POLITECNICO
MILANO 1863

SCUOLA DI INGEGNERIA INDUSTRIALE
E DELL'INFORMAZIONE

Electronic and atomic structures of iron oxalate dihydrate at extreme conditions

TESI DI LAUREA MAGISTRALE IN
ENGINEERING PHYSICS - Nanophysics and Nanotechnology

Author: **Francesca Frulla**

Student ID:	969787
Advisor:	Marco Moretti
Co-advisor:	Valerio Cerantola
Academic Year:	2021-22

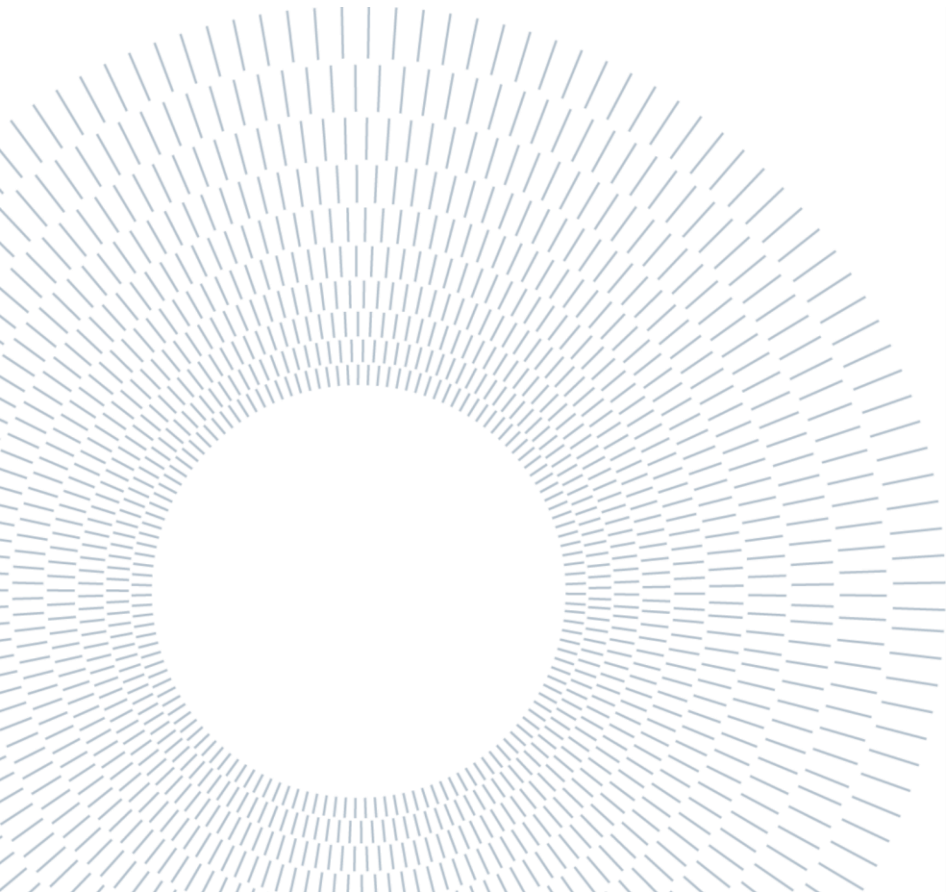

Abstract

Simple inorganic coordination polymers, such as the iron oxalate, have attracted much interest in the past decades because of their fascinating solid state properties such as gas absorption, electrical conduction and catalytic activity. For these reasons, iron oxalate dihydrate has emerged as an important building block for the preparation of new, functional advanced materials and as an important precursor to the synthesis of materials relevant in Geoscience and Planetary science. Despite extensive investigations carried out, next to nothing is known about the physico-chemical properties of iron(II)oxalate dihydrate at extreme pressures and temperatures. Preliminary results [1] have shown that $FeC_2O_4 \times 2\ H_2O$ exhibits several structural transitions upon pressure increase, which have not yet been characterized. Moreover, the simple chemical composition, the intrinsically high oxygen fugacity and the capability of Fe to exist in multiple valence states are desirable prerequisites to attempt the synthesis of new exotic C, O and H bearing materials at extreme pressures and temperatures. Thus, the aim of this thesis is the investigation of the structural evolution (both electronic and atomic) of $FeC_2O_4 \times 2\ H_2O$ at extreme pressures and its stability at extreme pressures and temperatures. In this thesis, pre-selected single crystals of $FeC_2O_4 \times 2\ H_2O$ (typical dimensions $15\times15\times10\ \mu m^3$) were characterized up to 100 GPa and high temperatures by Synchrotron Mössbauer spectroscopy (SMS) and X-ray diffraction (XRD) respectively at ID18 and ID15b at the European Synchrotron (ESRF) (Grenoble, France), and by Raman spectroscopy at the Bayerisches Geoinstitut (BGI) (Bayreuth, Germany). We used SMS to study the nuclear and electronic evolution of the material under compression, XRD to study changes in the long-range ordered structure and Raman spectroscopy to determine the vibrational, rotational and other low-frequency modes of oxalate characterizing molecules. Thanks to combination of these different techniques we obtained a complete analysis of the sample under compression. We confirmed the formation of a new phase starting at ~ 22 GPa. The structural transition happens in a broad P-range and is finally completed at P ~ 38 GPa. We also observed what seems to be a slow spin transition starting at 50 GPa. Our interpretation is not yet conclusive because in the Mössbauer spectra the Fe^{2+} high and low spin components reach a steady-state where both co-exist. Other explanations of what we have observed could be i) the pressur-induced oxidation of

Fe^{2+} to Fe^{3+}, or ii) the transition to a new structure characterized by two distinct iron sites and spin states. Moreover, we were able to synthesis new products after laser heating the samples at different pressures. At 100 GPa and ~ 2750 K we formed the already known orthocarbonate $Fe_4C_3O_{12}$ while at 50 GPa and ~ 2000 K we formed a new tetracarbonate $Fe_5C_3O_{13}$ which may contain OH^- group in its structure. The latter discovery has interesting potential implications for the transport of carbon and water from the Earth surface to the deep interior of our planet.

Key-words: Iron oxalate, Mössbauer spectroscopy (SMS), X-ray diffraction (XRD), Raman spectroscopy, extreme conditions, structural evolution.

Abstract in lingua italiana

I polimeri inorganici di coordinazione, come l'ossalato di ferro, hanno suscitato molto interesse negli ultimi decenni a causa delle loro affascinanti proprietà allo stato solido come l'assorbimento di gas, la conduzione elettrica e l'attività catalitica. Per queste ragioni, l'ossalato di ferro diidrato è emerso come un componente importante per la preparazione di nuovi materiali avanzati funzionali e come un importante precursore della sintesi di materiali rilevanti per la Geoscienza e per le Scienza Planetaria. Nonostante le approfondite ricerche condotte, quasi nulla è noto sulle proprietà fisico-chimiche del ferro(II)ossalato diidrato a pressioni e temperature estreme. I risultati preliminari [1] hanno dimostrato che $FeC_2O_4 \times 2\ H_2O$ presenta diverse transizioni strutturali sull'aumento della pressione, che non sono ancora state caratterizzate. Inoltre, la semplice composizione chimica, la fugacità intrinsecamente elevata dell'ossigeno e la capacità di Fe di esistere in molteplici stati di valenza sono prerequisiti desiderabili per tentare la sintesi di nuovi materiali esotici con cuscinetti C, O e H a pressioni e temperature estreme. Pertanto, lo scopo di questa tesi è l'indagine dell'evoluzione strutturale (sia elettronica che atomica) di $FeC_2O_4 \times 2\ H_2O$ a pressioni estreme e della sua stabilità a pressioni e temperature estreme. In questa tesi, dei preselezionati cristalli singoli di $FeC_2O_4 \times 2\ H_2O$ (dimensioni tipiche $15\times15\times10\ \mu m^3$) sono stati caratterizzati fino a 100 GPa e a temperature elevate con spettroscopia Mössbauer (SMS) e diffrazione a raggi X (XRD) rispettivamente a ID18 e ID15b presso l'European Synchrotron (ESRF) (Grenoble, Francia) e con spettroscopia Raman al Bayerisches Geoinstitut (BGI) (Bayereuth, Germania). Abbiamo utilizzato SMS per studiare l'evoluzione nucleare ed elettronica del materiale sotto compressione, XRD per studiare i cambiamenti nella struttura ordinata a lungo raggio e spettroscopia Raman per determinare i modi vibrazionali, rotazionali e altri modi a bassa frequenza dell'ossalato che caratterizzano le molecole. Grazie a queste diverse tecniche abbiamo ottenuto un'analisi completa del campione sotto compressione. Abbiamo confermato la formazione di una nuova fase a partire da ~ 22 GPa. La transizione strutturale avviene in un ampio intervallo di pressioni ed è finalmente completata a P ~ 38 GPa. Abbiamo anche osservato quella che sembra essere una lenta transizione di spin a partire da 50 GPa. La nostra interpretazione non è ancora definitiva perché negli spettri Mössbauer i componenti di Fe^{2+} in ''spin alto'' e ''spin basso'' raggiungono uno stato stazionario dove entrambi coesistono. Altre spiegazioni di ciò che abbiamo osservato potrebbero essere i) l'ossidazione indotta dalla pressione di Fe^{2+} a Fe^{3+}, o ii) la transizione a una nuova struttura caratterizzata da due siti di ferro e configurazioni di spin distinti. Inoltre, siamo stati in grado di sintetizzare nuovi prodotti dopo il

riscaldamento laser dei campioni a diverse pressioni. A 100 GPa e ~ 2750 K abbiamo formato un ortocarbonato $Fe_4C_3O_{12}$, già noto, mentre a 50 GPa e ~ 2000 K abbiamo formato un nuovo tetracarbonato $Fe_5C_3O_{13}$ che può contenere OH^- gruppo nella sua struttura. Quest'ultima scoperta ha interessanti implicazioni potenziali per il trasporto di carbonio e acqua dalla superficie terrestre all'interno profondo del nostro pianeta.

Parole chiave: Ossalato di ferro, spettroscopia Mössbauer (SMS), diffrazione a raggi X (XRD), spettroscopia Raman, condizioni estreme, evoluzione strutturale, ciclo del carbonio profondo, ciclo dell'acqua

Contents

1. Introduction

1.1 Importance of iron oxalate dihydrate ($FeC_2O_4 \times 2\ H_2O$)

Simple inorganic coordination polymers (CPs), such as oxalate compounds, have attracted much interest in the past decades because of their fascinating solid state properties such as gas absorption, electrical conduction and catalytic activity [2, 3]. Their importance comes from having a highly ordered structure and a wide design latitude of frameworks by choosing various metal ions and bridging ligands [3]. Indeed, changing the design of the framework and making use of internal degrees of freedom of space (so-called coordination space) in addition to the lattice (framework), the hydrophilicity or acidity of the frameworks can be controlled. This results in several advantages for the construction of proton conductors and in the control of the condensed state of the water cluster existing in a pore as a conducting media. By combining these variables, one can also design hydrogen-bond networks as a conducting pathway and built-in acidic groups as a proton source.

Iron oxalate dihydrate, $FeC_2O_4 \times 2\ H_2O$, is one of the simplest CPs and for these reasons, it has emerged as an important building block for the preparation of new, functional advanced materials. This introduction is focused on two main applications of Fe-oxalate dihydrate nowadays: its use i) as reactant in high-capacity Lithium-ion batteries (LIBs) (Fig. 1.1.1) and ii) as precursor in the study of geologically relevant materials at extreme conditions (Fig. 1.1.2).

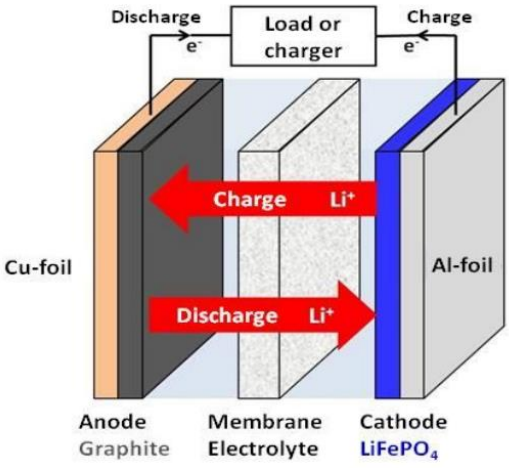

Figure 1.1.1: Anhydrous FeC_2O_4 used as anode in LIBs.

Lithium-ion batteries, with the increasing demand for high energy and power density, have stimulated great research interest in high performance anode materials for their application in hybrid electric vehicles (HEVs), electric vehicles (EVs), and smart grids.

Consequently, transition metal oxalates (TMOxs) have attracted considerable attention because they are promising candidate for anode materials. Indeed, in addition to their fascinating solid state properties, they have numerous other appealing features, they are environmentally friendly and economically cheap to produce [4]. Moreover, transition metal oxalates have been developed as promising candidates for anode materials owning to their higher electrochemical reactivity, outstanding cyclability, lower cost, simpler manufacturing process and environmental friendliness in comparison with their equivalent oxides [5]. It is well known that two basic reactions are involved in the TMOxs electrodes, as shown in Equations (1) and (2):

$$MC_2O_4 + 2Li^+ + 2e^- \rightarrow Li_2C_2O_4 + M \quad (1)$$

$$Li^+ + e^- \rightarrow Li \quad (2)$$

The electrochemical conversion process leads to the reduction of the metal ions to the metallic state together with the formation of lithium oxide. The first process is the electrochemical conversion reaction of Li^+ to form $Li_2C_2O_4$ and metallic nanoparticles (M). The electrochemical activities of metal nanoparticles, oxalate matrix and inserted Li^+ have a great influence on reversible capacity in subsequent cycles. The second reaction, related to the mesoporous texture of iron oxalate particles, is the capacitive effect in which Li^+ can implant into the multilayer and mesoporous nanostructure and combine with electronic. However, it is not so simple to use TMOxs as anode materials [6]. Indeed, the slow Li^+ ion diffusion and low intrinsic electronic conductivity lead to high irreversible capacity and poor rate performance, impeding their practical application for power batteries. These problems typically are overcome by coating with carbonaceous substances [7] and doping metal element [8]. Although, these strategies are ineffective for the migratory problem of Li^+ ions within the materials and doping limits the energy storage performance because it can lead to unstabilized activity of complex nanocomposites produced in electrochemical reaction process. A promising alternative to overcome these issues are the micro-nano structure design of active materials. Higher capacities at higher rates can be achieved by using the advantage of dispersion at the nanoscale and the enhanced stability of one-dimensional nanoparticles. Generally, the nano crystallization of active materials is advantageous for shorter diffusion path but the stability of micro-nano structure is more critical and the structure instability can bring numerous problems.

In this regard, it is also important to consider the different structure in which TMOxs can crystallize. Indeed, different crystal structures exhibit different interface energies that affects the diffusion behaviors of Li^+ ions and thus different electrochemical properties. Iron oxalate dihydrate crystallizes in two allotropic forms, α-FeC_2O_4 x 2 H_2O monoclinic C2/c and β-FeC_2O_4 x 2 H_2O orthorhombic Cccm and it can exist in a mixed phase of the two phase α@β-FeC_2O_4 x 2 H_2O [6, 9]. α-FeC_2O_4 x 2 H_2O exhibits a

polygonal prism-shaped microstructure with good monodispersivity and clear edges. This well-organized morphology offers larger interfaces between particle and electrolyte and more channels for Li^+ ions mobility. Whereas the β-FeC_2O_4 x 2 H_2O consists of submicrometer sized lamellar plates and slight aggregation [6, 9]. The smaller dimension is advantageous for shorter diffusion path but problematic for structure instability. In addition, the iron oxalate with mixed state of phase transformation α@β-FeC_2O_4 x 2 H_2O exhibits more homogeneous pores and integrates both characteristics of α and β that leads to high electrochemical reactivity, leading to superior cycling stability and satisfactory rate performance.

From a structural perspective, the presence of crystal water could be problematic, since it negatively influences the electrolytes behavior during the redox reaction. Attempts are made to completely remove the two moles of water through low temperature heating treatments, with the side effect however to deteriorate the crystallinity of the anode materials. But in reality, water molecules might be an advantage and could be used to increase electrochemical properties of iron oxalate since crystal water can provide a stable sustaining force and enlarge interlayered spacing to maintain the high elastic buffer space and improve diffusion kinetics of Li^+ [10]. However, during Li^+ (de)intercalation process, water molecules not only can cause slippage stresses and structural collapse, but also present an obvious inhibitive role on the electrochemical activity of complex nanocomposites and formation of compact organic deposit interfaces, thus resulting in substantial structural deficiencies and poor lithium storage performance. Thus, considering all the various effects that can affect the performance and the electrochemical capabilities of this material, it is crucial to continue investigating how it behaves and reacts when exposed to external parameters, among them also pressure (and temperature). In particular, extreme conditions have the ability to profoundly affect the physico-chemical properties of any material, directly contributing to structural modifications, at the atomic and electronic levels, influencing properties such as density, heat transport, electron transfer etc. Thus, pressure-driven phase transitions of oxalates to some high pressure polymorphs while maintaining the same stoichiometry, could potentially improve the properties for which iron oxalate dihydrate is important for lithium batteries storage materials.

As mentioned before, our interest in $FeC_2O_4 \times 2\ H_2O$ also relates to Earth sciences, since it can be used as precursor for the synthesis of iron carbonate $FeCO_3$ that is one of the largest contributors for the recycling of carbon in the deep earth [11] (Fig. 1.1.2). Moreover, Fe-oxalate unique stoichiometry is also of extreme interest for the synthesis and discovery of new Fe-C-O-H containing materials, which might be of help explaining how light elements have been trapped inside the Earth during Earth's formation and differentiation 4.5 billions years ago (Fig. 1.1.3).

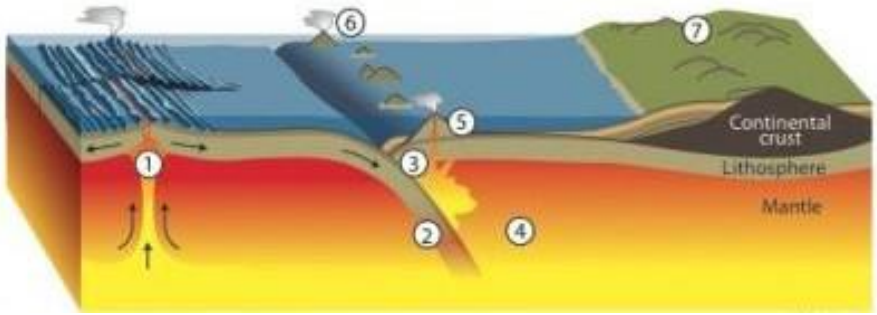

Figure 1.1.2: Cross section of the modern plate tectonic cycle, including (1) creation of oceanic crust at mid-ocean ridges, (2) subduction at ocean trenches, (3) dehydration and melting beneath subduction volcanoes, (4) carbon storage in the upper mantle, (5) carbon transport in island arc volcanoes where oceanic crust is subducted beneath oceanic crust, (6) carbon emissions from volcanoes, and (7) diffuse carbon sources.

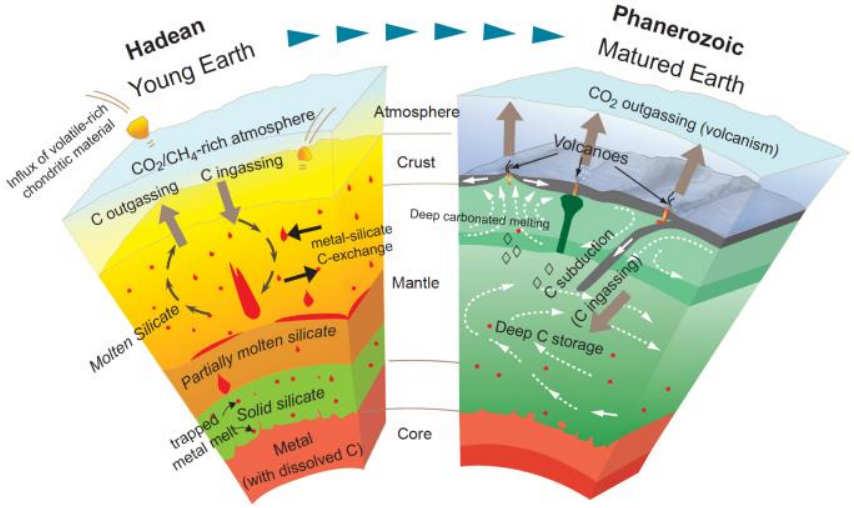

Figure 1.1.3: Range of deep-Earth processes. From Dasgupta (2013).

$FeCO_3$, which is the chemical composition of the mineral siderite, is known to be one of the major carbon carrier from the Earth's surface down to the Earth's interior, via oceanic plates subduction, thus having a very important role in crustal carbon sequestration. It is also believed to be a potential carbon-host in deep geochemical reservoirs [12, 13]. In fact, geophysical, geochemical and petrological evidences suggest that sufficiently cold and/or fast subducting slabs can penetrate deep inside the mantle, immobilizing carbon in the form of carbonates or other minerals at those depths. The understanding of the behavior of carbonates at extreme conditions, $FeCO_3$ but also $MgCO_3$ and $CaCO_3$, the determination of their stability regions and of their properties is fundamental to understand the deep carbon cycle. Carbonates phase stability and carbon oxidation state in the Earth are influenced by two major mechanisms: chemical reactions with surrounding minerals and transformations

(including self-oxidation-reduction) of carbonates themselves at specific pressures and temperatures [13]. For instance, $FeCO_3$ at P > 50 GPa and T > 1500 K transform into two, newly discovered, tetracarbonate phases [12, 13], which are formed by CO_4 tetrahedra as main building blocks, similar to silicates SiO_4 groups. These new structures have proven to be extremely stable at deep mantle conditions. The transformation to tetracarbonates has been observed also for $MgCO_3$ and $CaCO_3$, however the presence of iron, which has the capability to exist in multiple valence states, creates the conditions for redox reactions and the formation of a wide variety of tetracarbonates compositions and structures, contrary to Mg- and Ca- endmembers. Overall, the presence of iron is extremely important because it can radically change the thermodynamic stability of carbonate and tetracarbonate phases, thereby preserving them from breaking down to oxides and diamonds. This behavior may be a direct consequence of pressure-induced spin crossover. Indeed, at high-pressure conditions, as those found in the Earth's lower mantle, it is known that iron undergoes to a spin transition that modify the electrons configuration in the outer 3d orbitals [47, 48], with consequent changing in physical properties such as conductivity, sound velocity, density and volume.

Most of the studies on deep carbon have been performed so far using carbonates as starting materials. Thus, the use of other reagents, with more complex stoichiometry and characterized by different oxidation states is very important in order to expand our knowledge on the forms that carbon can take at extreme conditions. In this perspective, Fe-oxalate is the perfect candidate since it contains iron, carbon and oxygen elements, similar to carbonates but in different ratio, and it contains also water, which increases the complexity of the system but can deliver very intriguing results because it intimately connects to the study of the deep water cycle, i.e. water transport and water distribution inside the Earth. Indeed, it is estimated that the amount of water transported by subducting slabs into the mantle is at least 8.7×10^{11} kg/year when instead the flux of water outgassing from the mantle through magmatism is much lower and it is estimated at 2×10^{11} kg/year [14]. Recent studies on natural samples coming from the deep mantle suggest the existence of an hydrated transition zone [15]. However, water may be transported as far as the bottom of the lower mantle and by reacting with metallic iron in the lower mantle can form hydrous phases or reduced iron hydride [14]. Iron hydrides could exist and be one of the constituent phases of the Earth's core [16]. Thus, it is very important to dig into the complex chemical reactivity of Fe-H-O compounds at different P/T conditions, in order to fully characterized what is hidden deep inside our planet.

At last, the special and unique chemical composition of iron oxalate dihydrate is very interesting for the study of the interiors of icy planets, or gas giants such as Jupiter, Neptune or Uranus, which are known to be formed mainly by light elements such as

H, He, C, N, O and possibly by Fe-alloys to form their cores [17, 18]. Thus, the investigation of Fe-oxalate stability at different pressure and temperature conditions will prove to be a very important contribution also for the more generic study of planetary sciences.

1.2 Sample

In this work we analyzed the structural stability and behavior of Ferrous Oxalate Dihydrate at extreme pressures and temperatures. $FeC_2O_4 \times 2\ H_2O$ is simple inorganic coordination polymer but may also be viewed as a metal organic framework. The compound can be found in nature as the mineral humboldtine, usually associated with coal or hydrothermal deposits but may also form by the interaction of fungi and iron-bearing rocks. In a recent study, Müller et al. [1] described a new synthetic process for the preparation of high-quality Fe-oxalate single crystals starting from pure ^{57}Fe metal powder, thus suitable for Mössbauer studies. Below, I will first introduce how the compound is formed naturally on the Earth and then how it was synthesized in order to do the experiment.

1.2.1 How does it form in nature?

Humboldtine, also known by the German name Eisen-Resin because of its aspect and coloration, is one of the oldest known oxalate minerals [19]. It was initially found in Kolowserux, Bohemia (today Czech Republic), by de Rivero in 1821 but a complete characterization occurred only during the first half of 1900, after it was found, as a secondary mineral, associated with brown coal at the D'Arco cape, Elba Island, Italy. Some years later it was also found associated with iron oxides at the Cape Calamita mine of the same island and most recently it was described in pegmatite fractures, associated with hematite, magnetite and goethite, in Minas Gerais, Brazil. It has also been described in association with gypsum, cassiterite, tourmaline and quartz and has been found in different regions of the Czech Republic, Germany, England and Canada. It is usually found in the form of small prismatic crystals or as incrusted masses with fibrous aspect. The crystals are transparent or translucent, presenting yellow to amber-yellow color (Fig. 1.2.1.1).

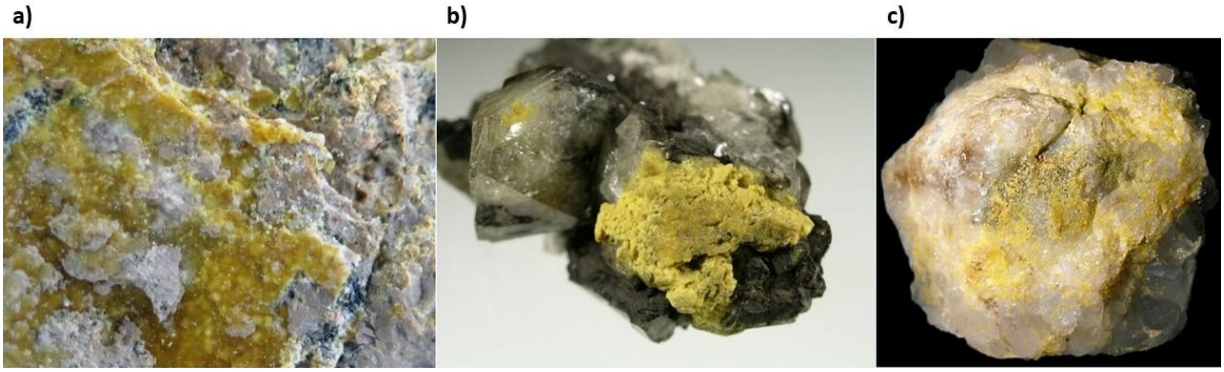

Figure 1.2.1.1: Humboldtine samples found in a) Csordakúti Mine, Hungary, b) Csordakúti Mine, Hungary and c) Vignola Mine, Italy.

Humboldtine was also recovered from iron-containing rocks in mineralogical collections after cleaning them with oxalic acid and on iron archaeological objects after their restoration using oxalic acid, thus formed in the context of anthropic activities. Humboldtine is of great interest for the scientific community for its formation mechanism. The sources of oxalic acid necessary for oxalate crystallization have not been discussed in most works dedicated to natural humboldtine. However, in a number of works, it was assumed that the products of microorganism metabolism can serve as a source of oxalic acid for the formation of iron oxalate. It is interesting to mention that during the chemical weathering of rocks due to acid excretion by lichens the formation of different metallic oxalates have been observed. In the case of glushinskite, $MgC_2O_4 \times 2\ H_2O$, formed at the lichen/rock interface of a magnesium-rich serpentine colonized by the lichen *Lecanora atria* it has been found that the biomineral contains appreciable amounts of iron (Mg:Fe ratio is ca. 20:1) but pure humboldtine has never been found associated with lichen activity in rocks [20]. In contrast, in the study of weathering of calcareous rocks by lichens it was reported the precipitation of a non-hydrated Fe(III) oxalate at the interfaces between dolomite rock and the lichen species *Caloplaca callopisma*. The behavior of the Fe(II)/Fe(III)/oxalate system is extremely complex, as shown by different experimental studies, and one may speculate that probably aerial or microbial oxidation of Fe(II) to Fe(III) species occur in these natural environments, with subsequent hydrolysis and precipitation of more or less crystalline iron oxides [21]. On the other hand, if we consider humboldtine in brown coals, it can be associated with micro-organisms since species of bacteria and fungi are found in brown coals and are capable of producing oxalic acid [22]. Thus microorganisms can serve as a source of oxalic acid to form iron oxalate humboldtine.

1.2.2 Synthesis of $FeC_2O_4 \times 2\ H_2O$

The availability of high-quality single crystals of $FeC_2O_4 \times 2\ H_2O$ is crucial for diffraction or spectroscopic studies at high pressure. Muller et al. [1] describes a

versatile synthetic approach to single crystals of $FeC_2O_4 \times 2\ H_2O$ starting from metallic iron. This preparative two-step approach starts with the dissolution of iron in dilute sulphuric acid and subsequent reaction of the obtained iron(II)sulphate solution with excess dimethyl oxalate under autogenous pressure according to Equations 1.2.2.1 and 1.2.2.2.

$$Fe + H_2SO_4\ (H_2SO_4 + H_2O \text{ in excess}) \rightarrow Fe^{2+} + SO_4^{2-} + H_2 \uparrow + (H_2SO_4 + H_2O \text{ in excess}) \quad (1.2.2.1)$$

$$Fe^{2+} + SO_4^{2-} + HO_2CCO_2H \text{ (excess)} + (H_2SO_4 + H_2O \text{ in excess}) \rightarrow$$
$$[Fe^{II}(C_2O_4)x2H_2O] \downarrow + (HO_2CCO_2H + H_2SO_4 + H_2O \text{ in excess}) \quad (1.2.2.2)$$

For simplicity, dimethyl oxalate (DMO) has been replaced in Eq. 1.2.2.2 with oxalic acid. The latter is released in situ upon heating of the reaction mixture. All reactions were carried out in thermodynamic equilibrium and produced only the stable α-polymorph. Figure 1.2.2.1 displays the characteristic morphology of crystals of α-$FeC_2O_4 \times 2\ H_2O$ obtained under hydrothermal conditions.

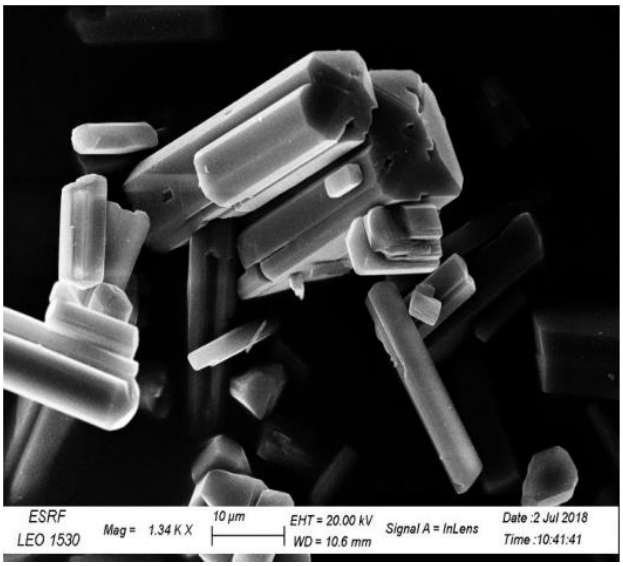

Figure 1.2.2.1: SEM-Micrograph of single crystal of α-$FeC_2O_4 \times 2\ H_2O$. From Müller et al. [1].

α-$FeC_2O_4 \times 2\ H_2O$ is a polymeric coordination compound composed of bidentate oxalate dianions $C_2O_4^{2-}$, divalent ferrous Fe^{2+} ions, and water molecules. Oxalate dianions and Fe^{2+} cations alternate in a planar arrangement that results in one-dimensional infinite linear chains along the b-axis as shown in Figure 1.2.2.2.

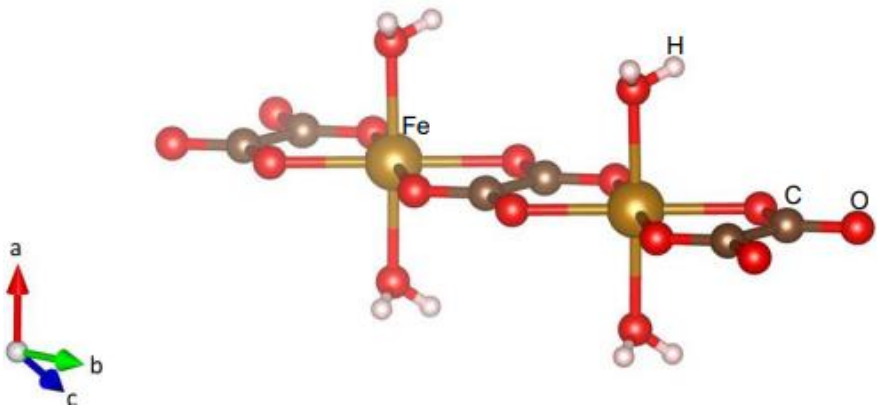

Figure 1.2.2.2: Representation of the single, infinite, planar 1-D chain of α-$FeC_2O_4 \times 2\ H_2O$ with repetitive units composed of a divalent iron(II)cation, a bidentate oxalate dianion, and two water molecules. From Müller et al. [1].

Each Fe^{2+}-ion is in octahedral coordination and the resulting octahedra comprises four oxygen atoms of two oxalate dianions on equatorial positions and two oxygen atoms of two water molecules on axial positions approximately parallel to a (the angle H_2O-Fe-OH_2 is 182° at ambient pressure). The three-dimensional structure of $FeC_2O_4 \times 2\ H_2O$ consists of linear infinite chains along [010]. These chains in the b-c-plane are linked by hydrogen bonds between the oxygen atoms of water molecules and oxalate dianions belonging to adjacent chains as show in Figure 1.2.2.3.

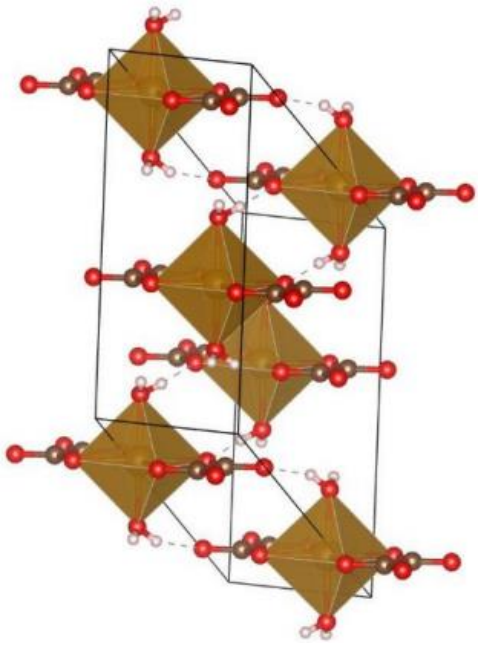

Figure 1.2.2.3: Representation of three-dimensional structure of $FeC_2O_4 \times 2\ H_2O$. From Müller et al. [1]

1.3 Aim of the thesis

This thesis is focused on the experimental investigation of the high-pressure high-temperature behaviour of synthetic iron oxalate dihydrate (Humboldtine) $FeC_2O_4 \times 2 H_2O$. Several studies have been performed to investigate the structure and physico-chemical properties of Fe-oxalate at ambient conditions but very little is known about the stability and pressure-dependence of the molecular and crystalline structure of this compound at extreme conditions [1]. Preliminary results have shown that $FeC_2O_4 \times 2 H_2O$ exhibits several structural transitions upon pressure increase, which have not yet been characterized. These studies clearly depict a system in continuous evolution, which is fascinating and merits further investigation. The relevance of this study relates to different research fields such as technology (as anode material for lithium-ion batteries), deep carbon cycle (as precursor of $FeCO_3$) and planetary science (as Fe-C-O-H phases). The structural and electronic transitions in crystalline and amorphous materials at extreme conditions are of considerable interest in condensed matter physics, and despite a lot of effort was dedicated to the study of more conventional compounds such as oxides, silicates, carbonates and metallic-alloys, very little is known on the behavior of metallorganic frameworks at elevated pressures and temperatures. For instance, what happens to the oxalate ions when compressed to multi-kilobars pressures? Moreover, $FeC_2O_4 \times 2 H_2O$ stability studies aim to look into the storage of light elements inside the Earth and bigger icy planets, known to have a "lighter" chemical composition than the Earth. In fact, the simple chemical composition, the intrinsically high oxygen fugacity of the system (oxalate anion $C_2O_4^{2-}$ + water molecules $2 \times H_2O$) and the capability of Fe to exist in multiple valence states are desirable prerequisites to attempt the synthesis of new exotic C, O and H bearing materials at extreme pressures and temperatures. Thus, the aim of this study is the investigation of the structural evolution (both electronic and atomic) of $FeC_2O_4 \times 2 H_2O$ at extreme pressures and its stability at extreme pressures and temperatures. The preparation of new materials with similar elemental compositions is of considerable interest for elucidating the sequestration of light elements during differentiation and core formation processes in the earth's mantle. The lack of information on this compound at extreme conditions is due to the technical challenges to simultaneously probe the sample at high pressures and temperatures. In order to overcome this difficulty we used the unique properties of the European Synchrotron Radiation Facility (ESRF). The ESRF is a synchrotron light source that works with electrons produced by an electron gun linearly accelerated to relativistic velocity and then forced to follow a circular path thanks to a magnetic field. When the trajectory changes, the electrons undergo an acceleration which results in X-ray emission. This source has an extremely high photons flux, high brilliance and low divergence. This latter

properties are related to lower acquisition times and to the spot size on the sample which must be very tiny (~ μm) and is fundamental to study samples confined in a reduced dimension and at extreme conditions, as the case of the experiments carried out in the context of this thesis.

2. Methods

2.1 High-pressure experiments

2.1.1 Diamond anvil cells

A diamond anvil cell (DAC) is a high-pressure device introduced in the late 50th [23]. It enables the static compression of small (sub-millimeter-sized) pieces of materials to extreme pressures to recreate, for instance, the environments existing deep inside planets and synthesize materials and phases not observed under ambient conditions.

A DAC consists of two opposing gem quality oriented diamonds with a sample compressed between the culets (tips) (Fig. 2.1.1.1). A metallic gasket is used to contain the sample from spreading outwards, radially during compression.

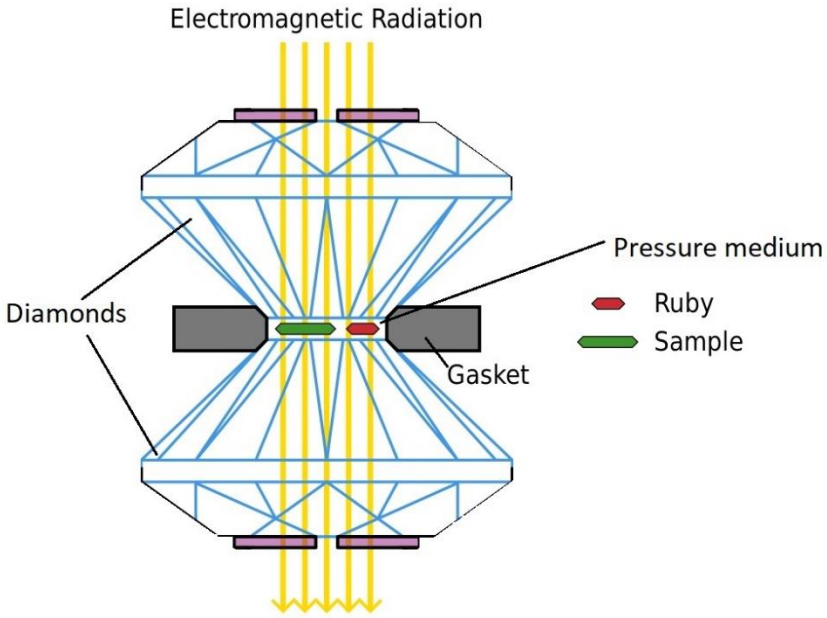

Figure 2.1.1.1: Schematic diagram of diamond anvil cell.

An important characteristics of the DAC technique is the anvils transparency to a wide range of electromagnetic radiation that allows for in situ studies of pressurized samples using different absorption, scattering and emission methods.

The operation of the DAC relies on a simple principle:

$$Pressure = {Force}/{Area} \tag{2.1.1.1}$$

A sample placed between the flat parallel faces of two opposed diamond anvils is subjected to pressure when a force pushes the two opposed anvils together. Based on

this principle, different pressure ranges can be achieved by varying the diamond culet size. Generally, the smaller the area of the culets, the highest the reachable pressure.

The preparation of a diamond anvil cell starts by gluing a pair of gem quality diamonds to hard-metal seats, usually made of tungsten-carbide alloys, which transmit the load from the cell body to the diamonds. The seats are directly fixed to the two mobile parts of the DAC body. For the correct application, the two diamonds should be strictly coaxial and perfectly aligned against each other in order to avoid possible tilting between them. Tilt between the diamonds generates pressure gradients on the sample and leads to an achievable pressure reduction and may result in sample loss or diamonds destruction at high pressures. The sample is constrained inside a gasket typically made of rhenium (Re) because it has good mechanical properties and contains no iron, nor other metals impurities, a critical aspect in element selective analytical studies such as Mössbauer spectroscopy or x-ray absorption (XAS) and emission (XES) experiments. The gasket is beforehand pre-indented to 30 μm from an initial thickness of ~ 200 μm. The indentation has the shape and the size of the diamonds culets. A hole of different dimension (depending on the culets size) is drilled in the center, which is used as a pressure chamber where the sample is placed with or without pressure medium.

In most of the DACs used nowadays, the force is mechanically generated in two ways:

1. screw driven
2. membrane driven

In the former, the force is applied by screwing the two parts of the DACs together i.e [24]. Instead, in the second one, the force is applied using an expandable membrane that contract or expand depending on the amount of gas applied, which in turn compress or release the two parts of the DACs in contact with the membrane i.e [25]. The membrane allows for pressure adjusting without disturbing the cell, which is an important advantage for synchrotron research. However, this type of cells is not well suitable for high-temperature experiments due to thermal expansion of gas in the membrane, which complicates pressure control.

In the current work both types of cells were used. In particular, the piston-cylinder type BX90 mechanical DAC [24] (Fig. 2.1.1.2) was used in order to do Raman spectroscopy at the University of Bayreuth (BGI) and the membrane cells provided by the European Synchrotron [25] (Fig. 2.1.1.3) were used in synchrotron Mössbauer spectroscopy (SMS) and X-ray diffraction (XRD) experiments respectively at ID18 and at ID15b at the ESRF.

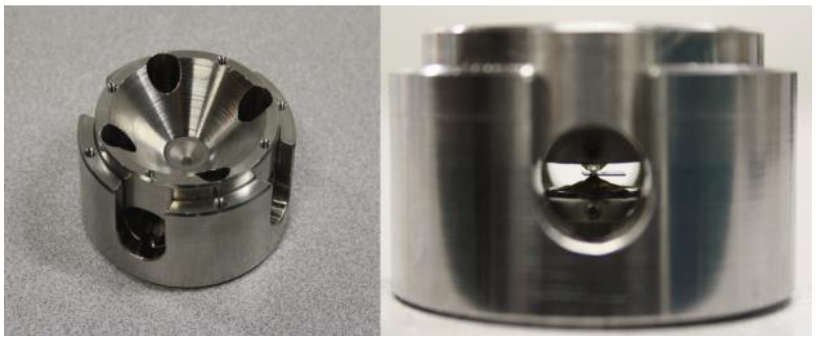

Figure 2.1.1.2: Photograph of a BX90 diamond anvil cell.

Figure 2.1.1.3: Photograph of a membrane diamond anvil cell.

The aim of this work is the study of materials at extreme conditions, which are of interest for solid state physics (structural and electronic transitions) and geoscience (reproducing the pressures and temperatures of the deep Earth's interiors). To reach these goals, diamonds with 150 μm and 300 μm culets were used, allowing us to reach pressures up to ~100 GPa.

2.1.2 Loading of pressure transmitting media

The intrinsic design of a DAC causes non-uniform stress upon compression. The stress is uniaxial and perpendicular to the diamonds culets surfaces, thus producing non-uniform strain. Pressure can be considered as a thermodynamic parameter only if a sample is surrounded by hydrostatic media (liquid or gas). Moreover, non-uniform stress leads to destruction and quality loss of single crystal samples and thus is

inapplicable for experiments using single crystals as starting material. Aiming to avoid these problems and to overcome the "non-hydrostaticity" in DACs, different pressure-transmitting-media (PTM) have been used. In order to achieve quasi-hydrostatic conditions during the experiments, the best pressure-media are noble gases: He, Ne, Ar. They crystallize at relatively high pressures, remain "soft" in solid state and preserve quasi-hydrostatic conditions even after crystallization due to relatively low yield strength. In this work Ne has been used for all the experiments done both at the ESRF and at the BGI for two reasons: i) good quasi-hydrostatic properties at high pressures and ii) melting temperature high than He, which is makes it a very suitable PTM in laser heating (LH) experiments at high pressures.

There are several ways to load pressure media inside the gasket. Gases are normally injected into the pressure chamber either using i) gas-loaders that compress the gas inside a vessel at several bars of pressure, or ii) cryogenically. In this work, Neon was pressurized inside the DACs using the gas loading system designed in BGI [26] and the one present at ESRF [27] for the loadings of BX90 and membrane type cells, respectively. A cell at ambient pressure and slightly open (~ 100 μm distance between the diamonds) is placed inside the vessel, and the entire "bomb" is then pumped with gas. After the gas reaches a specific filling pressure inside the vessel, normally of several hundred bars, the DAC is closed and the pressure increased, in order to trap the gas inside the gasket. Afterwards, the remaining gas from the "bomb" is released and the DAC can be removed from the vessel and used experimentally.

2.1.3 Pressure measurements

Determination of the pressure is a crucial point in any DAC experiment in order to precisely set the experimental conditions. Usually, methods based on calibrants loaded in a pressure chamber together with a sample are used. In this work two different techniques were used:

1. Ruby fluorescence spectroscopy
2. Raman spectroscopy of the diamond culets.

In particularly, at the ESRF the first one was used for pressure under ~ 80 GPa and the second one was used when the pressure reached values above ~ 80 GPa since from this point it becomes very difficult to measure the low intensity ruby fluorescence lines, for which the shift with pressure is calibrated. At BGI, only Raman spectroscopy was used since there was no ruby present in the DAC.

A ruby fluorescence method is a rapid and easy way to measure a pressure. It is based on the pressure dependence of the wavelength λ of the $Al_2O_3:C^{3+}$ R_1 peak (Fig. 2.1.3.1) obtained from the shock wave equations of states of metals [28, 29]. The pressure can be derived from the equation:

$$P(GPa) = \frac{A}{B}\left[\left(\frac{\lambda}{\lambda_0}\right) - 1\right] \quad (2.1.3.1)$$

where λ is the measure wavelength of the peak and λ_0 is the wavelength of the peak at ambient pressure, A = 1905, B = 5 for non-hydrostatic conditions and B = 7.665 for quasi-hydrostatic conditions. In the current work commercially available ruby spheres from few to tens of microns in diameter size were used. For correct pressure measurements, the ruby should not touch the two diamonds culets during the experiment in order to minimize the deviatoric stresses acting on it that will result in distortion of the ruby spectra. Nevertheless, the ruby is normally positioned for simplicity in one of the culets.

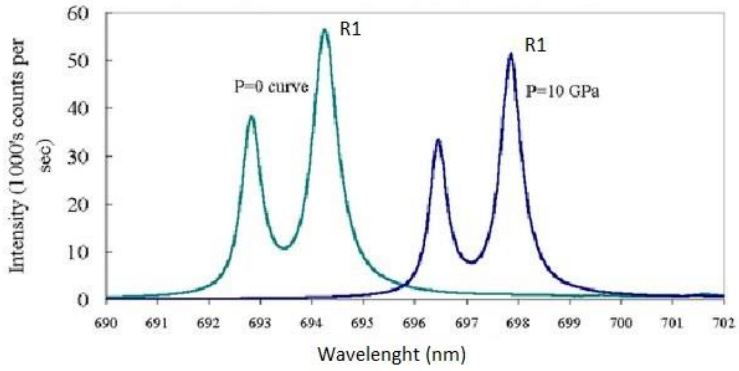

Figure 2.1.3.1: Typical Ruby Fluorescence Spectra for Ambient Pressure and 10 GPa.

Pressure measurements by ruby fluorescence method are limited to ~ 100 GPa due to a broadening and weakening of the R_1 peak signal. Already for P > 60 GPa the use of higher energy laser light, i.e. into the blue region (λ ~ 400 nm) and sensitive spectrometers are desired and becomes necessary at the highest pressures. Therefore, a second technique, the pressure dependence of the first order Raman mode of the diamond culets (Fig. 2.1.3.2), is used above megabar pressure. The wave number of the Raman band of the diamond is positively correlated with the normal stress experienced by the culet's face [30]. Quasi-hydrostatic pressure can be derived from the equation:

$$P(GPa) = K_0\left(\frac{\Delta v}{v_0}\right)\left[1 + \frac{1}{2}(K_0' - 1)\left(\frac{\Delta v}{v_0}\right)\right] \quad (2.1.1.1)$$

where Δv is the measured wavenumber of the high-frequency edge and v_0 is the edge frequency at ambient pressure, K_0= 547 GPa and K_0' = 3.75. The position of the high-wavenumber edge is defined as the minimum of the first derivative of the spectrum (Fig. 2.1.3.2).

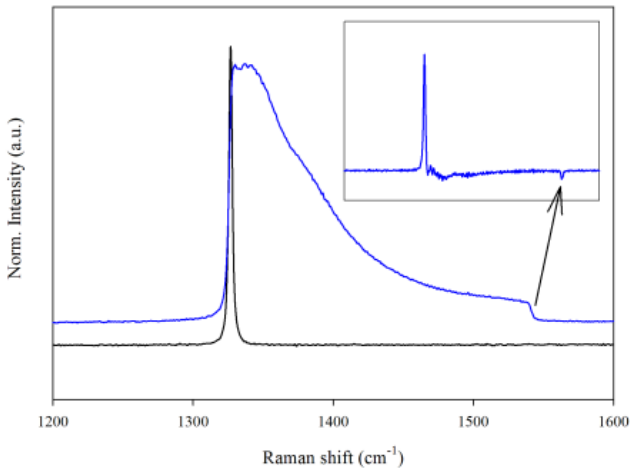

Figure 2.1.3.2: Typical Raman spectra from the center of the diamond anvil culet at ambient pressure (black) and at 105 GPa (blue). The inset shows a first derivative of the spectrum used for the correct determination of the high-wavenumber edge.

2.1.4 Laser heating in DAC

Laser heated diamond anvil cell allows studying materials under extreme conditions such those present inside the Earth and planetary interiors, to synthesize high pressure superconductors and unveil new chemical and physical properties of materials never observed in our daily life.

Nevertheless, laser heating in DAC is noy an easy task. Usually, it results in high temperature gradients inside the sample chamber, which can lead to non-homogeneous heating, thermally induced diffusion and/or movement of the sample. In order to reduce the temperature gradients in DAC, double-sided laser heating systems coupled with π-shapers positioned along the beams path, have been developed [31, 32, 33].

In this work, we extensively utilized the pulsed double-sided laser heating system described by Aprilis et al. 2017 [34]. Figure 2.1.4.1 shows the schematic diagram of the components of the laser-heating system used at ID18 at ESRF.

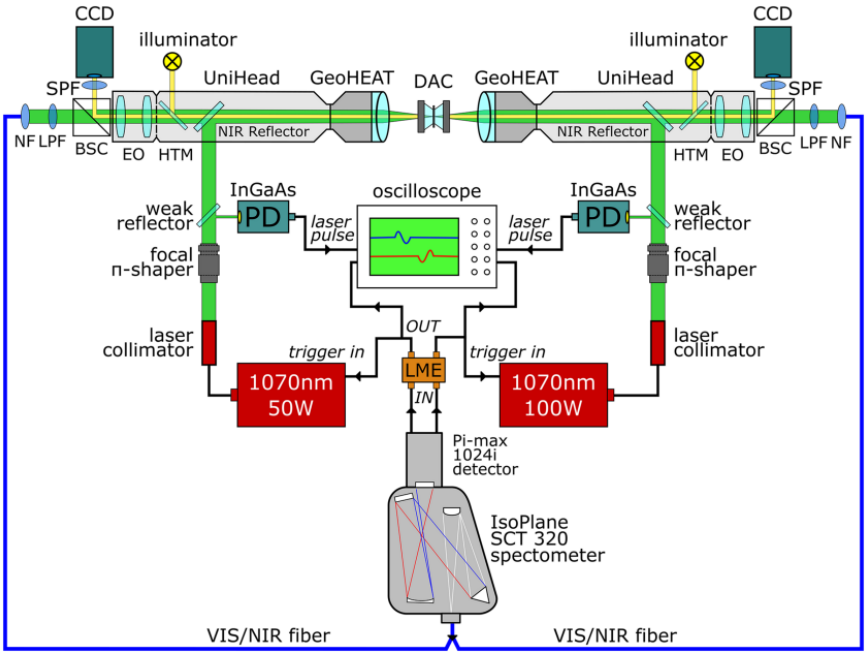

Figure 2.1.4.1: Schematic diagram of the double-sided pulsed laser heating system for diamond anvil cells.

The system consists of the following main components:

- Two infrared lasers that independently heat a sample in the DAC from two sides.
- Two UniHead modules with optical components to shape and focus each laser beam.
- Laser modulation and synchronization units including photodetectors, custom electronics, and an oscilloscope for control and visualization of the pulse shapes.
- Two VIS/NIR fiber bundles for collecting thermal radiation which are optically aligned on the sample.
- High-precision spectrometer coupled with a fast, intensified CCD detector used for time-resolved spectroradiometry measurements from both sides.

Two SPI RedPower R4 fiber lasers emitting at the near-infrared (NIR) central wavelength of 1070 ± 10 nm are used as laser sources, one with a maxim output power of 100 W and the other with 50 W. At present, the 100 W laser has been replaced by a 200 W one. Both lasers can be operated in continuous or pulsed modes with pulse frequencies up to 100 kHz. The collimated output beam of the laser is very wide for the intended applications. Therefore, each laser beam is collected by a Focal-π Shaper (Focal-π Shaper 9 1064 by AdlOptica GmbH), which is designed to shape a randomly

polarized Gaussian beam (TEM_{00}) into a flat-top when combined with focusing optics. The output beams of the Focal-π Shapers from both sides are focused using two sets of GeoHEAT 40 NIR lenses. The resulting beam spot can have a radius of about 20 μm. In order to heat a sample as homogeneously as possible, the peak and duration of the laser pulses should match from both sides. The UniHeads are necessary in order to focus the incoming laser radiation on the sample inside the DAC, providing high magnification images of the sample and its illumination and finally to collect thermal radiation from the sample for temperature measurements. Mirrors positioned at different angles depending on the experimental set-up are utilized to make laser beam and X-rays coaxial. The sample is illuminated using light emitting diodes built inside the UniHeads. Both UniHeads are equipped with modules for in situ temperature measurements and visual observation. The accurate in situ determination of the temperature of the laser-heated sample inside the DAC is crucial. The optical transparency of the diamond anvils allows the collection of the emitted radiation of the heated sample and the estimation of its temperature using the gray body approximation of Planck's law. The thermal radiation is collected from both sides through the same optical path that is used to focus the laser. This is done with a set of two UniHead modules. The image of the sample inside the DAC is magnified by the UniHead optics, working as a microscope, and projected into the cameras that are used for optical observation. The light is guided into an IsoPlane SCT 320 spectrometer (Princeton Instruments) and the resulting spectrum is collected by a PI-MAX 4 with a 1024 × 256 ICCD detector. The Intensified CCD camera with enhanced quantum efficiency gives the possibility of very fast collection.

2.2 Mössbauer Spectroscopy

2.2.1 Basic principles

The phenomenon of the emission or absorption of a γ-ray photon without loss of energy due to recoil of the nucleus and without thermal broadening is known as the Mössbauer effect. It was discovered by Rudolph Mössbauer in 1958 [35] and has had an important influence in many branches of physics and chemistry. Its unique feature is in the production of monochromatic electromagnetic radiation with very narrowly defined energy spectrum, so that it can be used to resolve minute energy differences with neV resolution. The direct application of the Mössbauer effect to chemistry arises from its ability to detect the slight variations in the energy of interaction between the nucleus and extra-nuclear electrons, variation which before its discovery had been considered negligible. Indeed, nuclei in atoms undergo a variety of energy level transitions, often associated with the emission or absorption of a gamma ray. The transitions are influenced by their surrounding environment, both electronic and

magnetic, which can change or split these energy levels. These changes can provide information about the atom's local environment within a system and ought to be observed using resonance/fluorescence techniques. There are, however, two major obstacles in obtaining this information: i) the 'hyperfine' interactions between the nucleus and its environment, which are extremely small in energy, and ii) the recoil of the nucleus as the gamma-ray is emitted or absorbed prevents resonance.

Let us consider the situation when an excited free atom at rest, mass M, is sending out a gamma quantum and let us define its potential energy E_0 as the energy difference between the ground state of the nucleus and its excited state. Initially, the system is characterized by a potential energy of E_0, then the initial energy is converted into two componenets, nominally gamma energy E_γ and recoil energy for the atom E_R. The photon has a linear momentum of p_γ while the recoiling atom of p_M. This situation is visualized in Figure 2.2.1.1.

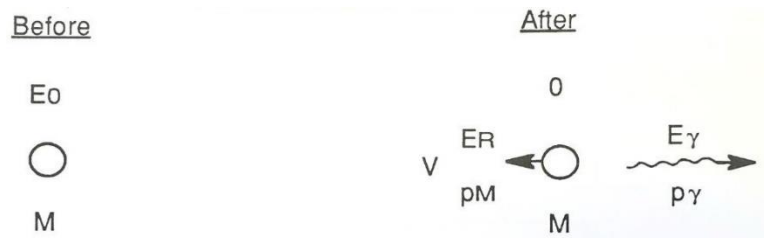

Figure 2.2.1.1: The situation before and after emission of a gamma quantum.

Therefore, a free nucleus during emission or absorption of a gamma ray, it recoils due to conservation of momentum, just like a gun recoils when firing a bullet, with a recoil energy E_R given by:

$$E_R = \frac{{E_\gamma}^2}{2Mc^2} \tag{2.2.1.1}$$

where E_γ is the energy of the gamma ray, M is the mass of the emitting nucleus and c is the velocity of light. Moreover, as the atoms will be moving due to random thermal motion the gamma-ray energy has a spread of values E_D caused by the Doppler effect and given by:

$$E_D = \left(\frac{v}{c}\right) E_\gamma \tag{2.2.1.2}$$

where E_γ is the energy of the gamma ray, v is the velocity of the emitting nucleus and c is the velocity of light. The γ-ray energy is thus seen to differ from the nuclear energy level separation by an amount which depends firstly on the recoil kinetic energy and secondly on the term related to the Doppler effect.

Fundamental radiation theory tells us that the proportion of absorption is determined by the overlap between the exciting and the excited energy distribution (Fig. 2.2.1.2) in this case the gamma-ray has lost energy E_R due to recoil of the emitting nucleus. The emitted gamma ray has E_R less energy than the nuclear transition but to be resonantly absorbed it must be E_R greater than the transition energy due to the recoil of the absorbing nucleus. To achieve resonance the loss of the recoil energy must be overcome in some way.

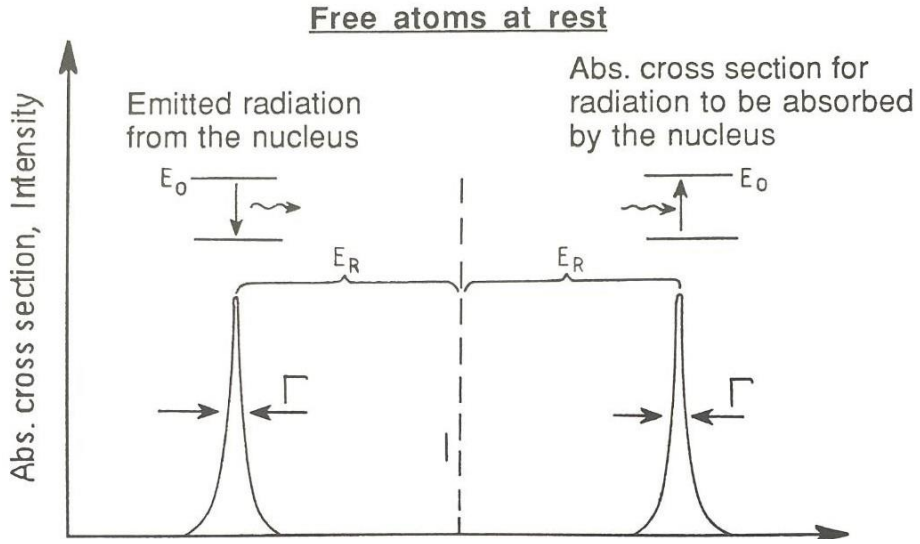

Figure 2.2.1.2: The exciting and the excited energy distribution.

Mössbauer discovered that when the atoms are within a solid matrix the emission and absorption of gamma-quanta are recoilless. Chemical binding and lattice energies are of the order of 1-10 eV and are considerably greater than the free-atom recoil energies. If the emitting atom is unable to recoil freely because of the chemical binding, the recoiling mass become the mass of the whole crystal rather than the mass of the single emitting atom. Indeed, the atom is bonded to its neighbors in a crystal and thus the movement of one atom is coupled to the movements of the other atoms building up the crystal. The atomic vibrations are described in the phonon spectrum of the crystal. However, such elastic vibrations do not carry momentum as the movement is a description of the relative motions of the atoms relative to each other. Thus, the recoil momentum has to be taken up by the crystal as a whole and the crystal recoil energy is given by the same equation of the case with the recoil energy of the free atom. However, the mass in the nominator is not the mass of the free atom but it is the mass of the whole crystal the decaying atom is member of. As the crystal recoil energy is completely negligible, also respect to the Heisenberg half width of ~10^{-4} meV, such a process will be called “recoilless”.

As just said, the crystal recoil energy is negligible respect to the Heisenberg natural linewidth of the transition. One of the most important influences on a gamma-ray energy distribution is the mean lifetime of the excited state. The uncertainties in energy and time are related to Planck's constant $h = 2\pi\hbar$ by the Heisenberg uncertainty principle:

$$\Delta E \Delta t \geq \hbar \qquad (2.2.1.3)$$

The time uncertainty, Δt, is interpreted as the mean life, τ, of the level emitting the gamma ray and is related to the more familiar half life, $T_{1/2}$, by $\tau = T_{1/2}/\ln 2$. The ground-state nuclear level has an infinite lifetime and hence a zero uncertainty in energy. However, the excited state of the source has a mean life τ of a microsecond or less, so that there will be a spread of the gamma-ray energies of the width Γ at half height where $\Gamma\tau = \hbar$. For ^{57}Fe the half life of the 14.4 keV level is 97.7 ns which gives the uncertainty in the energy as 4.67×10^{-9} eV. This uncertainty becomes the natural linewidth, Γ, of the transition, where $\Gamma = \hbar/\tau$, and this sets the best resolution which can be obtained when utilizing the entire time spectrum of the gammas. Electromagnetic considerations tell us that the intensity, I(E), of the emission line as a function of energy, E, will have the Lorentzian shape given by:

$$I(E) = \frac{(\Gamma/2)^2}{(E-E_0)^2+(\Gamma/2)^2} \qquad (2.2.1.4)$$

where E_0 is the center of the emission line. Γ is the full width of the line at half maximum (FWHM).

The narrow linewidth of ^{57}Fe, ~ 5×10^{-9} eV, is of the order necessary to detect the hyperfine interactions in the nucleus. As resonance only occurs when the transition energy of the emitting and absorbing nucleus match exactly the effect is isotope specific. The relative number of recoil-free events, and hence the strength of the signal, is strongly dependent upon the gamma-ray energy and so the Mössbauer effect is only detected in isotopes with very low lying excited states. Similarly the resolution is dependent upon the lifetime of the excited state limiting the number of isotopes that can be used successfully for Mössbauer spectroscopy.

The information that we can extract from Mössbauer spectroscopy are described by the Mössbauer parameters:

- center shift (CS)
- quadrupole splitting (QS)
- magnetic field (B)
- intensity (I)

The first three are the one that describing the hyperfine interactions. Let us see this parameter in more details and let us start considering the center shift. The CS is given by:

$$CS = IS + SOD \tag{2.2.1.5}$$

It is the sum of two different effect:

- the isomer shift (IS)
- the second order Doppler shift (SOD)

In a Mössbauer spectrum it is impossible to measure the two quantities separately, so one always operates with a sum of both, the CS.

The electrostatic energy between the positively charged nucleus and its surrounding electrons influences the nuclear energy level and thus the transition energies. As long as the nucleus is treated as an uniformly charged sphere embedded in an electronic cloud having a constant density over the nuclear volume the interaction is called electrostatic monopole interaction. This electrostatic energy will change if the radius of the nucleus will change or if the electrons can penetrate into the nucleus. Indeed, the nucleus has a radius that differs between different energy levels and the s-electrons have a finite probability to penetrate the nucleus. Then it is not very astonishing that the monopole electrostatic energy will vary for different nuclear energy level.

Let us consider that the electrons move around the nucleus at sufficiently large distance to consider the source as a point charge. Even if most of the electron charge density is outside the nucleus, s-electrons and partially p-electrons have a small but finite probability of being inside the nucleus. This effect, dominated by 1s-electrons, results in a shift of the energies of all the nuclear levels. The nucleus undergoes a transition from an excited state to a lower state upon emitting a gamma ray, the radius of the nucleus being different in these two levels $R_g \neq R_e$. The interaction in each level is the integration of the product of the nuclear charge density and the electron charge density over the region of overlap. Since the volume of the overlap region is different for the two nuclear states, the shift of each nuclear level is different. The difference between the shifts is effectively a measure of the electron density in the very thin annular shell, which makes up the difference in volumes of the two nuclear states. This, principally s-electron density will change in accord with the bonding of the atom and hence will be different for every compound which the atom can be part of. The mathematical expression for the isomer shift δ is:

$$\delta = \Delta E_A - \Delta E_S = \frac{2}{3}\pi Z e^2 (\rho_A - \rho_S)\left({R_e}^2 - {R_g}^2\right) \tag{2.2.1.6}$$

where ΔE_S and ΔE_A are energy differences between the excited and ground states of a source material and an absorber material consequently. The monopole interaction does not change degeneracy of the energy levels and, therefore, does not cause splitting of the absorption lines (Fig. 2.2.1.3).

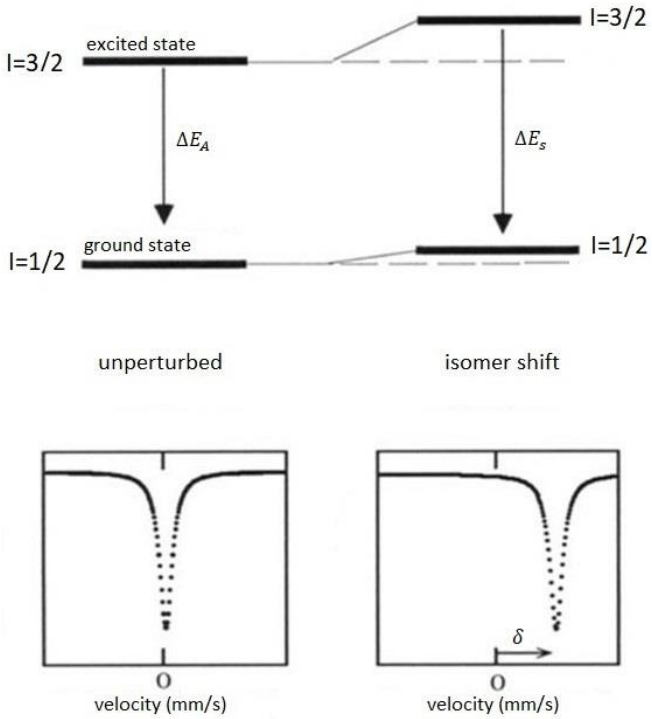

Figure 2.2.1.3: The diagram of ^{57}Fe nuclear energy splitting due to isomer shift and the corresponding absorption spectra.

The second component that contributed to the shift between the emission and the absorption lines is the second-order Doppler shift that is related to the vibration of the atoms on its lattice site. According to Einstein's special theory of relativity there is a relation between the time spans that are measuring the same event but that are measured by two identical clocks one in movement respect the other. Thus, Einstein's relation may be used to relate frequencies for the emitted gamma-ray from a moving atom compared to the frequency emitted by the same type of atom when it is at rest. The expression of this shift is given by:

$$\frac{\Delta E_{SOD}}{E} = -\frac{\langle v^2 \rangle}{2c^2} \qquad (2.2.1.7)$$

Where v is the velocity of the atom. It depends on Debye temperature and absolute temperature of the solid.

Between IS and SOD, the isomer shift is probably the most interesting parameter as it is related to the electronic density at the nucleus. Because only s-electrons have a finite

probability to penetrate into the nucleus the electron density at the nucleus $\rho_e(0)$ is given by the different s-contributions:

$$\rho_e(0) = \rho_{1s}(0) + \rho_{2s}(0) + \rho_{3s}(0) + \rho_{4s}(0) \qquad (2.2.1.8)$$

For ^{57}Fe 1s, 2s and 3s are filled shells and there is only a variation in the number of 4s electrons due to chemical reasons. However, the 1s-, 2s- and especially 3s-densities at the nucleus will vary between different chemical compound as a result of different shieldings. Thus, the most important cause to the variation at the nucleus is the number of 4s electrons and the shielding of 3s and 4s electrons by especially 3d electrons. As the 3s and 4s electrons are partly outside the 3d electrons it is easy to understand that the 3d electrons shield the nucleus for the 3s and 4s electrons and the effective nuclear positive charge will the decrease. From eq. 2.2.1.8 it is clear that IS increases when $|\rho_{4s}|$ decrease or when $|\rho_{3d}|$ increase.

It can be also demonstrated that the IS increases with the coordination number (CN), since to higher CNs normally are attributed larger interstitial voids, thus it is natural to assume more expanded electron orbitals and so higher IS values.

The variation of IS can be associated also to the electronegativity. A bond can be mostly covalent (sharing of charge between two atoms) or mostly ionic (transfer of charge from cation to anion). If the transfer of electrons from iron to the ligand is mostly of s-electrons, then one would expect a higher CS value, but if it is mostly of 3d electrons, due to decreased shielding, the CS values should decrease with increased ionicity of the ligand bond.

For our scope, it is very interesting to understand how CS vary with variation of pressure and volume. An increased pressure should squeeze the electron orbital to come closer to the nucleus, thus an increased pressure always should result in an increased electron density at the nucleus and accordingly a decrease in CS. An expansion in volume should have the opposite effect. However, as the influence is opposite for an increase in 3d and 4s electron densities the result is not self-evident. In general in metals, the CS decreases as the pressure increase, thus the compression of s electrons is the major cause to the change in CS. What is said here for metal is also roughly valid for ionic compound. All oxides and halides show a decrease in CS with increases in pressure. However, the effect seems to be stronger for Fe^{2+} compared to Fe^{3+} compounds.

Let us now consider the quadrupole splitting. If the potential created by the surrounding charges is asymmetrical the energy levels will also depend on the orientation of the nucleus in the anisotropic potential. This effect is called the quadrupole interaction. From a more fundamental point of view the quadrupole splitting is the result of i) a deviation from spherical symmetry for the nuclear charges

combined with ii) a deviation from spherical symmetry for the electronic field at the nucleus created by the electrons of the Mössbauer atom itself as well as from charges at the surrounding atoms. Thus, QS is the product of both nuclear and atomic parameters. If the nuclear spin, I, is equal or greater than 1 the charge distribution of the nucleus will have the shape of a rotational ellipsoid. Thus, in the case of ^{57}Fe, the ground state has a spherical charge distribution and the excited 14.4 keV state has an ellipsoidal distribution. The electrons surrounding the nucleus as well as the charges at the neighboring atoms create an electric field **E** at the nucleus. However, this field is not the same over the nuclear volume. To describe how this field varies we have to use the gradient concept, **EFG**. The core quadrupole moment interacts with the electrical field gradient and split the degenerate I=3/2 level into two sub levels, with magnetic spin quantum numbers m_I=±3/2 and ±1/2 (Fig. 2.2.1.4).

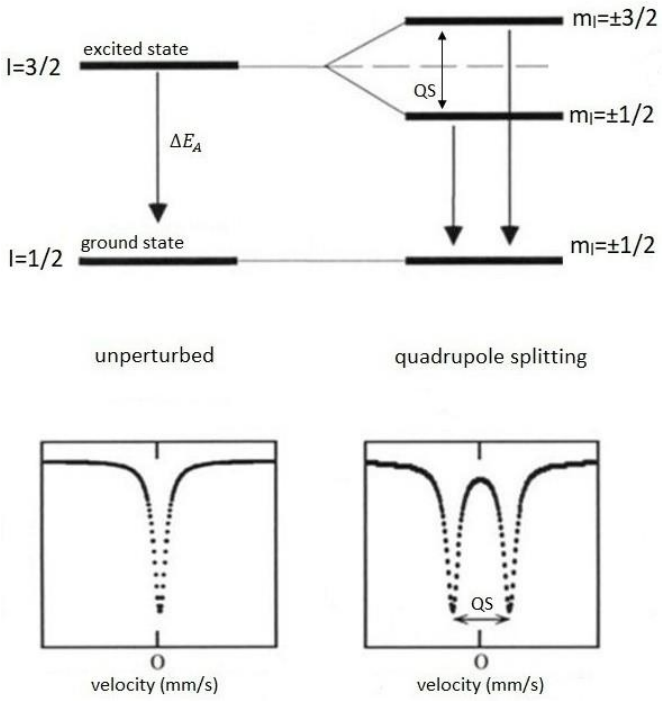

Figure 2.2.1.4: The diagram of ^{57}Fe nuclear energy splitting due to quadrupole splitting and the corresponding absorption spectra.

The charges that contribute to the **EFG** can be divided in two groups, one being electrons belonging to the atom itself, one being ions or other atoms in the neighborhood. A further subdivision can also be done when studying the electrons of the atom itself: core electrons in filled or half filled shells if the cloud is not exactly centered at the nucleus, EFG(nucleus), partially filled shells, EFG(valence) and surrounding ions, EFG(crystal).

The electric quadrupole splitting gives information on the oxidation state, the spin state, and the local symmetry of the Mössbauer atoms and generally, it depends also on external parameters, such as pressure and temperature. QS follows a less linear behavior as the pressure or volume increased respect to CS. In general, an increased distortion of the site geometry gives increased QS values.

Let us now see the last hyperfine parameter, the magnetic field. Since both protons and neutrons have a magnetic moment, all nuclei have magnetic dipole moments, except of course for those with an even number of protons and neutrons, for which the ground state will have a total angular momentum, I, of zero. The nuclear magnetic moment interacts with the magnetic moment of the electrons to produce the magnetic hyperfine interaction. In the presence of a magnetic field the nuclear spin moment experiences a dipolar interaction with the magnetic field i.e. Zeeman splitting. There are many sources of magnetic fields that can be experienced by the nucleus. The total effective magnetic field at the nucleus, B_{eff} is given by:

$$B_{eff} = (B_{contact} + B_{orbital} + B_{dipolar)} + B_{applied} \quad (2.2.1.9)$$

The first three terms being due to the atom's own partially filled electron shells. $B_{contact}$ is due to the spin on those electrons polarizing the spin density at the nucleus, $B_{orbital}$ is due to the orbital moment on those electrons, and $B_{dipolar}$ is the dipolar field due to the spin of those electrons.

This magnetic field splits nuclear levels with a spin of I into (2I+1) substates. Transitions between the excited state and ground state can only occur where m_I changes by 0 or 1. This gives six possible transitions for a 3/2 to 1/2 transition, giving a sextet as illustrated in Figure 2.2.1.5, with the line spacing being proportional to B_{eff}.

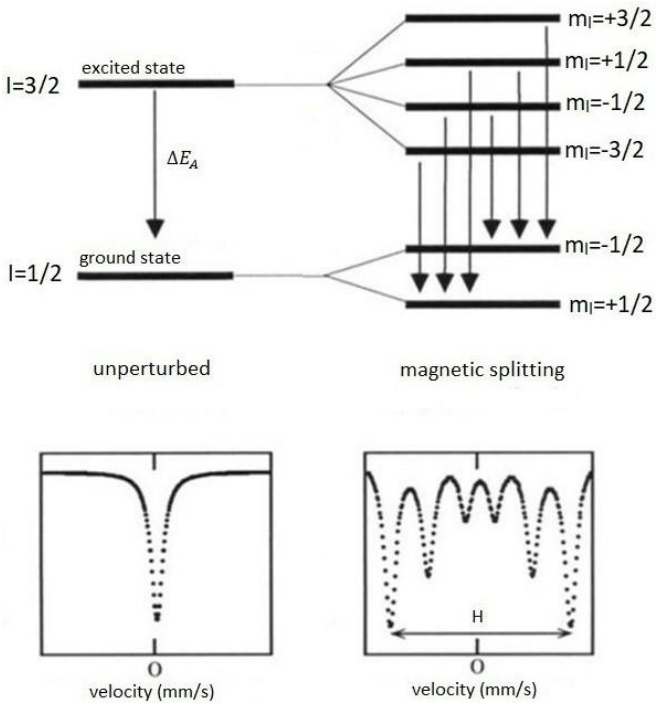

Figure 2.2.1.5: The diagram of ^{57}Fe nuclear energy splitting due to magnetic field splitting and the corresponding absorption spectra.

In this work I did not study materials with magnetic interactions and, hence, do not discuss this subject further.

Let us consider now the intensity. The total intensity from iron in a site is not affected by hyperfine interaction. However, in absence of quadrupolar and magnetic dipolar effects there is only one singlet, in pure quadrupolar electric case there is a doublet, and in the magnetic case a sextet. Thus, the total singlet, doublet and sextet areas will be identical if the number of iron atoms in the crystallographic positions are the same (Fig. 2.2.1.6).

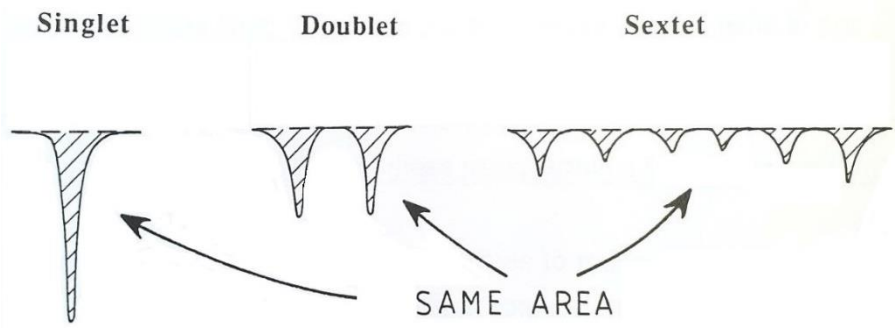

Figure 2.2.1.6: Total intensity.

The total absorption from a site is given by:

$$I(tot) = knf \quad (2.2.1.10)$$

Where f is the f-factor, n is the number of ^{57}Fe atoms per cm^2 and k is a constant that depends on the spectrometer and nuclear parameters. If the f-factor is the same for different sites then the total intensity is proportional to the number of ^{57}Fe atoms, thus the value of the intensity can be used to study site-occupancies.

2.2.2 Experimental set-up: Synchrotron Mössbauer source at ID18 at ESRF

Conventional Mössbauer spectroscopy has been a valuable tool for decades in studying the magnetic and electronic properties of various materials. However, the technique is not well suited for the study of samples with size smaller than 100 μm. Focusing radiation from radioactive sources is extremely difficult [36] and results in a low count rate and a reduction of spectral quality owing to an increase of the background. This leads to longer measuring times in order to obtain reasonable quality spectra, and even precludes some studies under extreme conditions, for example the investigation of physical properties of minerals relevant to the deep Earth at pressures of more than ~ 100 GPa [37] and high pressure superconductors [38]. Since in this study we are interested in the study of small single crystals of FeC_2O_4 x 2 H_2O inside a DAC, we performed our experiments using the Synchrotron Mössbauer Source technique [39] developed at the beamline ID18 at ESRF. The SMS is based on a nuclear resonant monochromator employing pure nuclear reflections of an iron borate ($^{57}FeBO_3$) crystal. The source provides ^{57}Fe resonant radiation at 14.4 keV within a bandwidth of 15 neV which is tunable in energy over a range of about ±0.6 meV. The beam of gamma-radiation emitted by the SMS is almost fully resonant and fully polarized, has high brilliance and can be focused to a 10 μm x 5 μm spot size. The small cross section of the beam and its high intensity allow for rapid collection of Mössbauer data.

The key element of the source that provides neV resolution is the iron borate $^{57}FeBO_3$ single crystal enriched in the ^{57}Fe isotope up to 95%. Iron borate is a canted antiferromagnet with a Neel temperature of 348.35 K. In this crystal all (NNN) reflections with odd N [i.e. (111), (333), etc.] are forbidden for electronic diffraction, while on the other hand they are allowed for nuclear diffraction. These are the so-called pure nuclear reflections. The planes (NNN) are parallel to the platelet surface. Therefore, the considered reflections are the symmetric ones.

The electronically forbidden but nuclear allowed reflections are employed to extract the nuclear scattering signal. This is possible because of the large difference in the polarization dependence of the electronic and nuclear scattering amplitudes and the antiferromagnetic ordering of iron atom spins in the $FeBO_3$ crystal. The sensitivity of nuclear scattering to the orientation of the magnetic field introduces an additional

phase π between waves scattered by two nuclei in the crystallographic unit cell and thus it recombines the destructive interference between the waves to a constructive one [40]. Owing to magnetic hyperfine splitting of the ^{57}Fe nuclear levels in the ground and the first excited states, the energy spectrum of the scattered radiation consists of several lines. Under these conditions the nuclear array in a crystal behaves as a multiline radiator. This is, of course, an inconvenient property for performing spectroscopic measurements. However, when the iron borate crystal is heated close to its Neel temperature of 348.35 K, the energy spectrum of the reflected radiation collapses to a single line [41]. Under these conditions a particular case of hyperfine interaction is realized where magnetic dipole and electric quadrupole hyperfine interactions are strongly mixed [42]. The combined multipath quantum interference in space, energy and spin domains results in the formation of a pseudo-single-line resonance structure in iron borate [43], which provides the basis for the creation of a single-line Synchrotron Mössbauer Source (SMS). The spectrum of the emitted radiation has an energy bandwidth close to the natural line width of the Mössbauer resonance.

For energy-domain Mössbauer spectroscopy one needs to scan the energy by changing the relative velocity of the source and the sample using the Doppler effect. The Doppler shift can be achieved by moving the iron borate crystal in the plane of the crystal surface [44]. This allows for both preserving the extreme focusing and employing complicated and/or heavy sample environments.

Figure 2.2.2.1 shows a typical optical scheme for a high-pressure experiment with a DAC using SMS based on the (111) pure nuclear reflection that is the one used in this work [4].

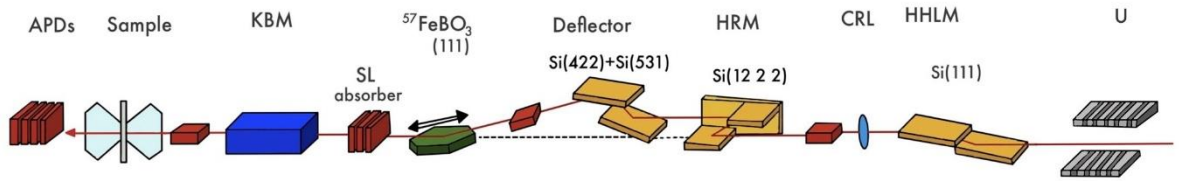

Figure 2.2.2.1: Scheme of set up at ID18 at ESRF.

The undulator (U) is the source of the synchrotron radiation beam. The first x-ray optic inside the beamline and after the undulators is a liquid nitrogen-cooled high-heat-load monochromator (HHLM), which consists of two separate Si(111) crystals on two separate mechanical supports. The HHLM is used to decrease the energy bandwidth of the beam to ~ 2 eV, and the following compound refractive lens (CRL) is used to decrease the divergence of the beam incident to the SMS. The first high-resolution monochromator (HRM) consists of an asymmetrically cut channel-cut Si(4 2 2) crystal

(outer) and a symmetric channel-cut Si(12 2 2) crystal (inner). The HRM is used to decrease the energy bandwidth of the beam further to ~ 15 meV. The deflector, with silicon reflections Si(422) and Si(531), directs the beam to the iron borate crystal (IB) where the final monochromatization within ~ 10 neV occurs. The beam from the SMS is focused by the Kirkpatrick–Baez mirrors (KBM), that allows to focus the beam after the SMS to a spot of about 10 μm x 5 μm on the sample located in the DAC. The gamma-radiation transmitted through the sample is monitored by avalanche photodiode detectors (APDs).

The beam after the iron borate crystal is also linearly polarized, but the vector of the electric wavefield lies in the vertical plane. The polarization of the beam makes the Mössbauer spectra measured with the SMS extremely sensitive to the direction of the electric field gradient (EFG) and of the magnetic field on nuclei. In studies of single crystals this sensitivity allows for determination of the geometry of the electric field gradient and hyperfine magnetic field.

The energy spectrum of gamma-radiation from a radioactive source is a Lorentzian distribution. In contrast, the energy spectrum of radiation emitted by the SMS is the result of the interference of two spectral lines (each with a Lorentzian distribution) with almost equal resonance energies during the collapse of the magnetic hyperfine structure [43]. Therefore, the energy spectrum of radiation emitted by the SMS to a first approximation can be described by a squared Lorentzian distribution.

2.3 X-Ray Diffraction

2.3.1 Basic principles

X-ray diffraction (XRD) is the most powerful tool used for identifying a crystalline material and determining its atomic structure. XRD analyses identifies the long-range order (i.e., the structure) of crystalline materials and the short-range order of non-crystalline materials (via pair distribution function analyses). From this information we deduce lattice constants and phases, average grain size, degree of crystallinity, and crystal defects. Advanced XRD provides information about strain, texture, crystalline symmetry, and electron density.

A crystal is a solid material made by atoms, molecules and/or ions that are arranged in a highly ordered microscopic structure, forming a crystal lattice that extends in all directions. When a monochromatic X-ray beam impinges onto the surface of a material, the atoms interact with the radiation and they can transmit, refract, scatter, and absorb it. Diffraction requires coherent scattering of the radiation by the solid. In this unique form of elastic scattering, there is no change in the energy of the X-ray after scattering. In order to have diffraction, the wavelength of the incident radiation has to

be smaller than the distance between the scattering sites. The wavelength of X-ray radiation is indeed well suited for resolving typical distances of covalent bonds. The energy of a quantum of this radiation is approximately 8 keV, which is approximately the energy of electrons in their orbitals. This equivalence of energy leads to interactions so that the electrons of an atoms will primarily be responsible for the scattering of X-rays.

When radiation impinges upon a solid, coherent scattering of the radiation by periodically spaced atoms results in scattered beams that produce spot patterns from single crystalline samples and ring patterns from polycrystalline samples. The number of electrons in a given volume of space, called electron density, determines how strongly an atom scatter X-rays. The directions of the scattered beam depend on the interatomic spacing (d_{hkl}) of the plane and the radiation wavelength while the intensity of the scattered beam depends on the orientation of the crystal relative to the direction of the incident X-ray and the position of each atom inside the unit cells.

The interference of the scattered X-rays leads to the phenomenon of diffraction. The origin of scattering can be developed starting with Huygen's principle, which states that every point along a wavefront can be considered the origin of a new wavefront (Fig. 2.3.1.1).

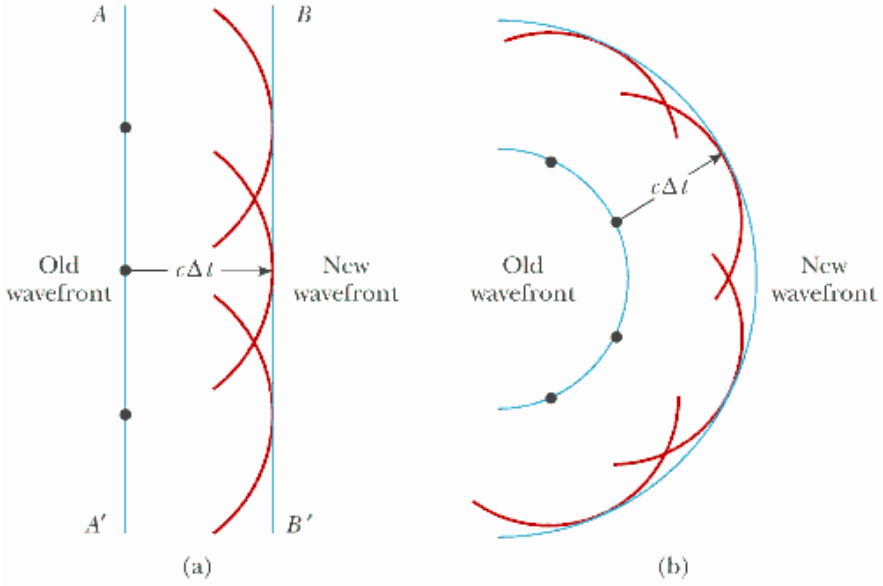

Figure 2.3.1.1: The Huygens' construction for an unrestricted wavefront in the case of: a) a plane wavefront, b) a spherical wavefront.

Objects placed in the path of a wavefront act as points of propagation for new wavefronts, called scattered waves. Therefore, if there are two point objects, A and B, in the path of the wavefront, each of the two points will propagate a new wavefront

having identical wavelengths and velocities of the original one. The offset in the maximum amplitude of the two waves depends on the position of A and B relative to the origin of the initial wavefront. The phenomena of diffraction depends on how the two scattered waves overlap. If the two scattered waves are in phase, the wave propagating from A will reinforce the scattered wave from B through constructive interference while if they are out of phase, the wave from A will reduce the amplitude of the wave from B through destructive interference.

In 1912 W.L. Bragg developed a relationship to explain how diffraction was related to the relative position of point objects in space. In this model, the crystal is modelled as a set of discrete reflecting parallel planes separated by a constant interval d and a wave of X-rays (with wavelength λ) is incident on the reflecting planes at an angle θ (Fig. 2.3.1.2). The wave is scattered by reflection from the planes at an identical angle θ. If we assume that the distance to our point of observation is very large compared to d, we can consider that the individual paths of scattered light are essentially parallel. Since there are a large number of planes, we observe constructive interference only when the reflected waves are perfectly in phase. This occurs when the difference in the length of the path of the incident and reflected waves of each plane (DE + EF = DEF in Fig. 2.3.1.2), is equal to some integer n of the wavelength of the incident X-rays:

$$DEF = n\lambda \tag{2.3.1.1}$$

By trigonometric relationship we know that the path difference is related to the distance separating the reflecting planes by the formula:

$$\frac{1}{2DEF} = d \sin\theta \tag{2.3.1.2}$$

Substituting n λ with DEF we derive Bragg's law of diffraction:

$$2d \sin\theta = n\lambda \tag{2.3.1.3}$$

This simple relationship means that larger spacing of repeating units in a crystal results in smaller diffraction angles.

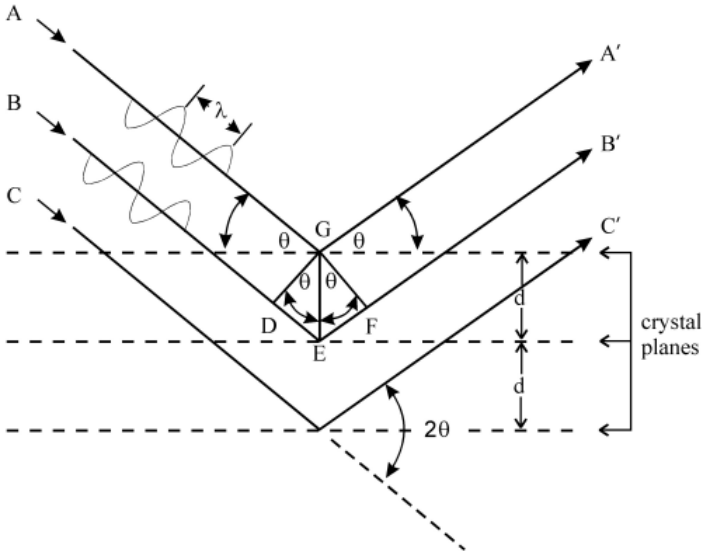

Figure 2.3.1.2: Model of Bragg's law of diffraction.

2.3.2 X-Ray Single Crystal Diffraction

Single-crystal X-ray Diffraction is a non-destructive analytical technique which provides detailed information about the lattice of crystalline substances, including unit cell dimensions, bond-lengths, bond-angles, and details of site-ordering. Also, it is the only technique that allows for structural solution, i.e. determination of new structures and discovery of new materials. To obtain these information and the crystal structure, the data generated from the X-ray analysis must be interpreted and refined using different software. As already discussed above, X-ray diffraction is based on constructive interference of monochromatic X-rays and a crystalline sample. When the sample is a single crystal, by changing the geometry of the system, i.e. the orientation of the centered crystal with respect to the incident X-rays and detector plane, all possible diffraction directions of the lattice can be obtained. Typical mineral structures contain several thousand unique reflections that can be labeled with indices (*hkl*). These indices indicate the position of the reflections within the diffraction pattern. This pattern has a reciprocal Fourier transform relationship to the crystalline lattice and the unit cell in real space, so they are fundamental to understand the spatial arrangement of the analyzed structure. Single-crystal X-ray diffraction is most commonly used for precise determination of a unit cell, including cell dimensions and positions of atoms within the lattice. Moreover, bond-lengths and angles are directly related to the atomic positions. The crystal structure of a mineral is a characteristic property that is the basis for understanding many of the properties of each mineral. Specific applications of single-crystal diffraction include new mineral identification, crystal solution and refinement, determination of unit cell, bond-lengths, bond-angles and site-ordering,

characterization of cation-anion coordination, variations in crystal lattice with chemistry and also discovery and determination of new compounds at extreme conditions (high pressure and/or temperature).

2.3.3 Experimental set-up: Synchrotron radiation source at ID15b at ESRF

Synchrotron radiation has several advantages relative to conventional X-ray source. From the Bragg equation one can see that the shorter is the wavelength the greater is the number of reflections that can be observed. This is crucial for DAC experiments because the opening angle of a DAC is usually very limited. Intensity of the synchrotron X-ray beam is several orders of magnitude higher compared to laboratory X-ray tubes and, therefore, data collection goes much faster. Moreover, the beam can be focused to a micron-size and this small beam size provided at synchrotron facilities allows to perform XRD at extreme conditions. In the current study, single-crystal X-ray diffraction experiments have been performed at beamline ID15b at ESRF [45], for which the design is shown in Figure 2.3.3.1.

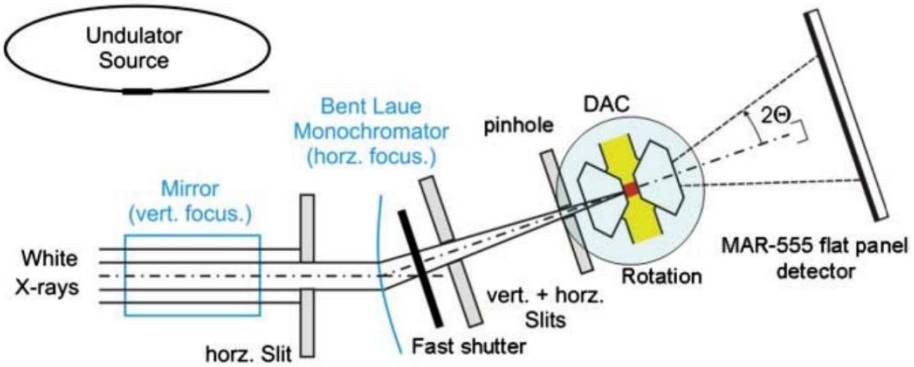

Figure 2.3.3.1: Schematic drawing of the experimental set-up of the ID15b beamline.

The experimental stage is located 40 m from the X-ray source. The beam, from an in vacuum undulator (U20 insertion device) with 20 mm period and a third harmonic tunable around 30 keV, is focused by vertical and horizontal transfocator and monochromatized by Si(111) Bragg monochromator. The working energy for high pressure experiments is 30 keV with a flux of 10^{12} photons/s at 200 mA resulting in typical exposure times of 1 sec. The beam size on the sample is about 30 x 30 μm^2 but can be made as small as 5 x 5 μm^2 for megabar pressure experiments. The measurements are performed by ω-scans, along a vertical rotation axis. The explored rotation range is limited by the geometrical opening cone of the DACs. With the standard design DACs being available at the beamline, a 64–80° ω-range is fully accessible. The appropriate step scans can be selected depending on data collection purposes and normally, a 0.5/1° step scan with 1 s integration time during sample oscillation between two consecutive steps, offers a good compromise between ω-

resolution and data collection time, which mostly resides on detector reading-out time. The scattered radiation is collected by an image-plate detector, an on-line Mar555 reader, which has a 430 x 350 mm (555 mm diagonal) active area.

2.4 Raman Spectroscopy

2.4.1 Basic principles

Raman spectroscopy is a non-destructive technique for observation of vibrational, rotational and other low-frequency modes in materials. It is a light scattering technique in which photons of monochromatic radiation incident on a sample are inelastically scattered after interacting with vibrating molecules within the sample.

When a molecule is in an electric field **E**, the electron cloud and nuclei become polarized resulting in an induced dipole moment **P**. The size of the dipole moment induced by a field of magnitude **E** is given by the polarizability α of the molecule:

$$\boldsymbol{P} = \alpha \boldsymbol{E} \tag{2.4.1.1}$$

Light consists of oscillating electric and magnetic fields. Thus, the induced dipole moment oscillates in phase with the applied field. The polarizability will depend upon the geometry of the molecule; as the molecule vibrates, the polarizability will change.

When light is scattered by a molecule, the oscillating electromagnetic field of a photon induces a polarization of the molecular electron cloud which leaves the molecule in a higher energy state with the energy of the photon transferred to the molecule. This can be considered as the formation of a very short-lived complex between the photon and molecule which is commonly called the virtual state of the molecule. The virtual state is not stable and the photon is re-emitted almost immediately, as scattered light. Raman spectroscopy exploits the fact that when radiation in the near infrared or visible range interacts with a molecule, several types of scattering can occur (Fig. 2.4.1.1):

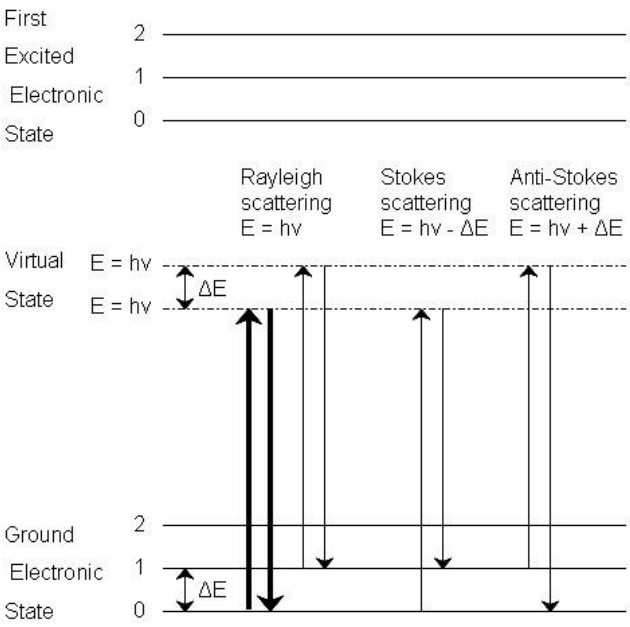

Figure 2.4.1.1: Scattering process scheme.

1. Rayleigh Scattering
2. Stokes Scattering
3. Anti-Stokes Scattering

In all three types of scattering, an incident photon of energy hν raises the molecule from a vibrational state to one of the infinite numbers of virtual states located between the ground and first electronic states. The type of scattering observed is dependent on how the molecule relaxes after excitation. In the vast majority of scattering events, the energy of the molecule is unchanged after its interaction with the photon; and the energy, and therefore the wavelength, of the scattered photon is equal to that of the incident photon. This is called elastic (energy of scattering particle is conserved) or Rayleigh scattering and is the dominant process. More rare is the Raman scattering, which is an inelastic scattering process characterized by a transfer of energy between the molecule and scattered photon. If the molecule gains energy from the photon during the scattering (excited to a higher vibrational level) then the scattered photon loses energy and its wavelength increases which is called Stokes Raman scattering. Inversely, if the molecule loses energy by relaxing to a lower vibrational level the scattered photon gains the corresponding energy and its wavelength decreases, which is called Anti-Stokes Raman scattering.

The intensity ratios of Stokes and Anti-Stokes Raman lines are determined by Boltzmann's law (Fig. 2.4.1.2).

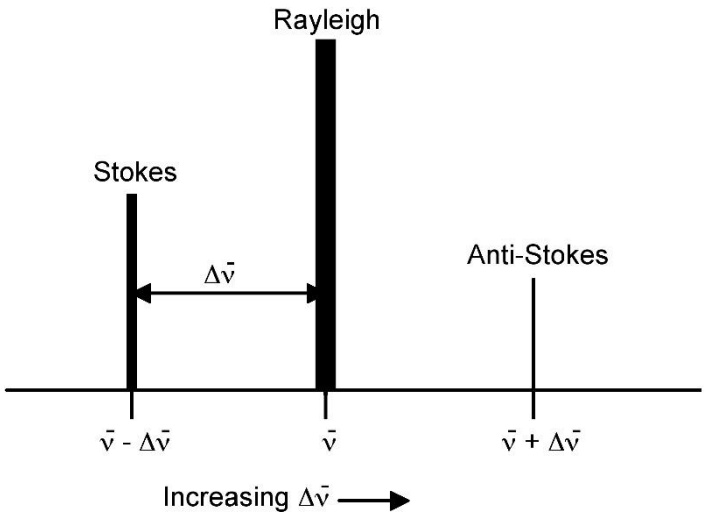

Figure 2.4.1.2: Intensity of scattering lines.

Quantum mechanically, Stokes and Anti-Stokes are equally likely processes. However, with an ensemble of molecules, the majority of molecules will be in the ground vibrational level and the more probable process is the Stokes scattering, whereby the photon is scattered at lower energy (shifted wavelength towards the red end of the spectrum). Since at room temperature the population state of a molecule is principally in its ground vibrational state, this is the larger Raman scattering effect. A small number of molecules will be in a higher vibrational level, and hence the scattered photon can actually be scattered at a higher energy, (a gain in energy and a shift to higher energy and a blue shifted wavelength). This is the much weaker Anti-Stokes Raman scattering. As a result, Stokes Raman scatter is always more intense than anti-Stokes and for this reason, it is nearly always the Stokes Raman scatter that is measured in Raman spectroscopy.

As already said, Raman activity depends on the polarizability of a bond and in order to have a Raman signal, the selection rule is that the molecular polarizability must change during the vibration, which intrinsically also depend on the molecule symmetry. The polarization is a measure of the deformability of a bond in an electric field. This factor essentially depends on how easy it is for the electrons in the bond to be displaced, inducing a temporary dipole. When there is a large concentration of loosely held electrons in a bond, the polarizability is also large, and the group or molecule will have an intense Raman signal. Because of this, Raman is typically more sensitive to the molecular framework of a molecule rather than a specific functional

group. Raman spectroscopy can provide information about both inorganic and organic chemical species. Raman can provide information on the metal ligand bond, leading to knowledge of the composition, structure, and stability of these complexes. Raman is also very useful for determining functional groups and fingerprints of organic molecules. Often, Raman vibrations are highly characteristic to a specific molecule, due to vibrations of a molecule as a whole, not in localized groups. The groups that do appear in Raman spectra have vibrations that are largely localized within the group, and often have multiple bonds involved.

2.4.2 Experimental set-up: LabRAM HR system at BGI

For the present study Raman spectroscopy was performed using the LabRAM HR developed by HORIBA (Fig. 2.4.2.1).

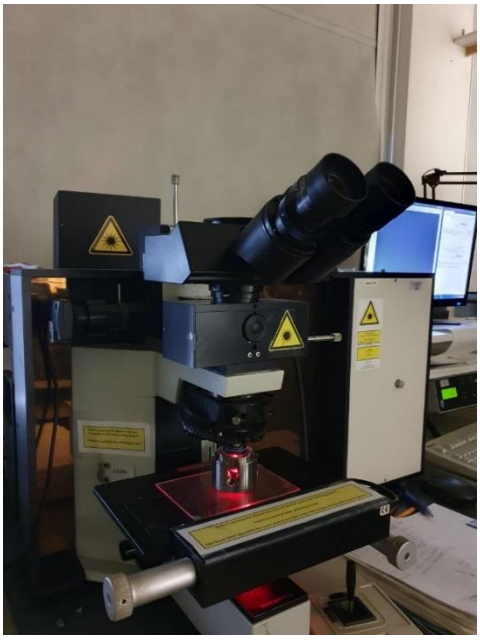

Figure 2.4.2.1: Photograph of the LabRAM HR at BGI.

This system excites Raman modes using the 532 nm HeNe green laser with maximum power of 10 mW. The scattered radiation was collected and analysed with an Olympus BX40 spectrometer. The following diagram (Fig. 2.4.2.2) of a LabRAM HR system shows the typical layout.

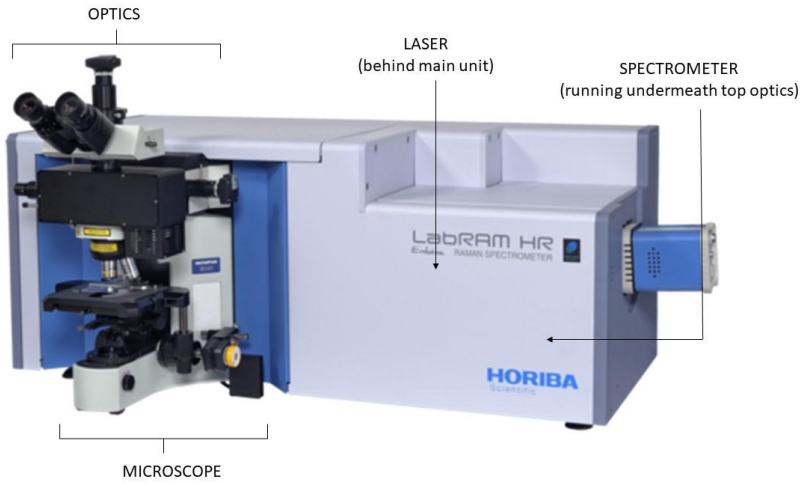

Figure 2.4.2.2: Diagram of the LabRAM HR.

The instrument can be subdivided into four main parts:

1. Laser: the HeNe (532nm) laser is internal, whilst other laser are external, mounted on an extended chassis at the back of the system.
2. Microscope: sampling is carried out through a standard optic microscope.
3. Spectrometer (Olympus BX40): dispersing the Raman signal into its constituent parts for detection by detector (usually CCD).
4. Optics: for coupling the lasers to the sample and carrying the Raman signal through to the spectrometer.

The LabRAM is equipped with standard white light illumination of the sample, by reflection and/or transmission and a color camera linked to the software allows the sample to be visualized.

3. Results

In this work we analyzed the evolution of the atomic and electronic structure of $FeC_2O_4 \times 2\ H_2O$ single crystals at extreme pressures and temperatures. Ferrous oxalate dihydrate, is a simple inorganic coordination polymer but may also be viewed as a metal organic framework. The compound can be found in nature as the mineral humboldtine, usually associated with coal or hydrothermal deposits. The availability of high-quality single crystals of $FeC_2O_4 \times 2\ H_2O$ is crucial for diffraction or spectroscopic studies at high pressure. In a recent study, Müller et al. [1] described a new synthetic process for the preparation of Fe-oxalate single crystals suitable for Synchrotron Mössbauer spectroscopy, X-ray diffraction and Raman spectroscopy, starting from pure ^{57}Fe metal powder. In this work, pre-selected single crystals of $FeC_2O_4 \times 2\ H_2O$ (typical dimensions $15\times15\times10\ \mu m^3$) were characterized by SMS, XRD and Raman spectroscopy. We used SMS to study the nuclear and electronic evolution of the material under compression, XRD to study changes in the long-range ordered structure and Raman spectroscopy to study vibrational, rotational and other low-frequency modes.

3.1 Synchrotron Mössbauer Spectroscopy (SMS)

3.1.1 Experiment HC-5141 at ID18 (ESRF)

The Mossbauer spectra were acquired at ID18 at the ESRF in Grenoble (France) during the experiment HC-5141. In order to carry out Mössbauer experiment at extreme pressures, we used membrane cells provided by the European Synchrotron. We compressed the samples to 50 GPa and 100 GPa and collected SMS spectra in situ, during compression, using two different DACs. The first DAC, that reached 50 GPa (DAC1), had cullets of 300 μm while the second one, that reached 100 GPa (DAC2), had cullets of 150 μm. Both DACs had rhenium gaskets and neon was used as pressure-transmitting medium to obtain quasi-hydrostatic conditions during compression. Both DACs were prepared by loading a $FeC_2O_4 \times 2\ H_2O$ single crystal and a smaller ruby crystal. The pressure was measured using different techniques (Methods). For pressures under ~ 80 GPa we measured the wavelength of the ruby fluorescence, while above ~ 80 GPa we determine the pressure through the shift of diamond Raman frequency caused by the stress generated on the culets. In fact, even in neon, at P > ~ 50 GPa the ruby experiences progressively less hydrostatic conditions, thus we changed the measurement approach to obtain more realistic pressures. The correlation between the wavelength and the pressure was calculated using the web site ''Fluorescense pressure calculation and thermocouple tools'' [46]. For pressures below ~ 50 GPa we used the calibrated scale ''ruby fluorescence tool'' from Dewaele et

al. 2008 [28] adapted for quasi-hydrostatic conditions, while for pressures between ~ 50 GPa to ~ 80 GPa we used the scale calibrated for non-hydrostatic conditions from Shen et al. 2020 [29]. For P > ~ 80 GPa we used the ''Diamond Raman tool''. At each P-point, the pressure was measured before and after the experimental run and the difference in values contributed to the pressure uncertainty, which was estimated to be 0.5 GPa for both experiments.

Mössbauer spectroscopy was performed using the Synchrotron Mössbauer Source at the ESRF. SMS spectra were collected during operation in multibunch mode (7/8 + 1 filling). The narrow (~ 6 neV) energy component of X-rays at the Mössbauer energy of 14.4 keV was extracted from a wide spectrum of synchrotron radiation using a $^{57}FeBO_3$ single crystal monochromator and focused to a beam width of size of ~ 10 x 3.6 μm^2 using Kirkpatrick-Baez mirrors (Fig 3.1.1.1). The velocity scales of all Mössbauer spectra were calibrated at 5 mm/s, relative to 25 μm thick α-Fe foil.

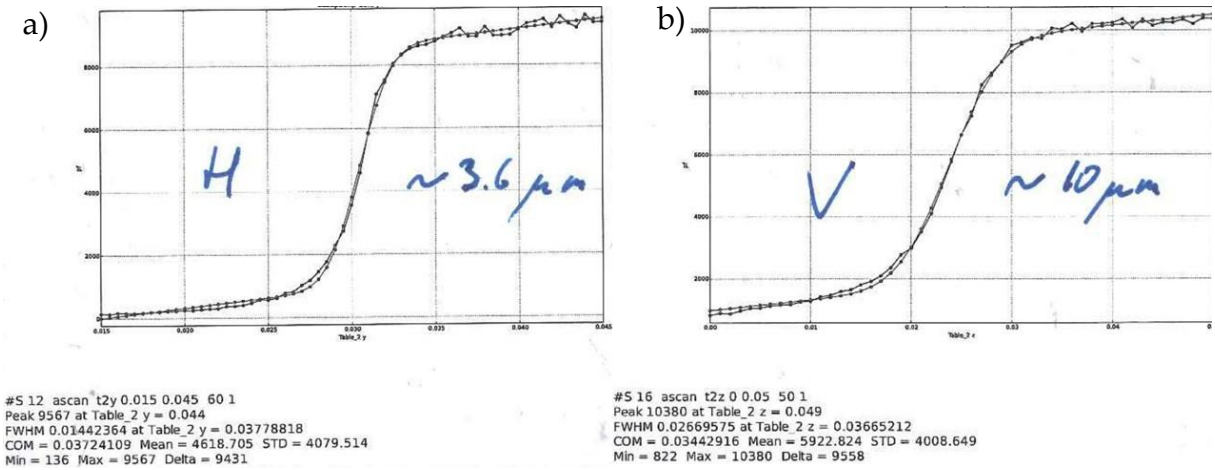

Figure 3.1.1.1: Beam width: a) horizontal width, b) vertical width.

Fe-oxalate Mössbauer spectra were collected in compression at different pressure steps up to 100 GPa (DAC2). Each SMS spectrum took approximately 30/45 minutes to be collected. Once reached the target pressures, 50 and 100 GPa for DAC1 and DAC2 respectively, the samples were laser heated at different temperatures, using the double-sided laser heating system present at ID18 at the ESRF [34]. The laser heating system is composed by two infrared lasers (one with a maxim output power of 200 W and the other with 50 W) that independently heat the sample in the DAC from two side. In DAC1 the maximum power reached with the two infrared laser was 7 W and the sample was heated at a peak temperature of 4000(150) K and afterwards annealed at a lower temperature of ~ 2000(100) K. With DAC2, the maximum output power reached with the upstream laser was 8-9 W while the maximum power reached with

the downstream laser was 10-11 W. The sample was heated for a total of ~ 5 minutes on two different areas of the crystal. In area A (Fig. 3.1.1.6) the measured upstream temperature was ~ 2600(100) K while the downstream temperature was ~ 2200(100) K. In area B (Fig. 3.1.1.6), the measured upstream temperature was 3100(100) K and the downstream temperature was 2800(100) K.

In DAC1 we only acquired the spectrum before and after the laser heating at 50 GPa (Fig 3.1.1.2, Fig. 3.1.1.3 and Fig. 3.1.1.4).

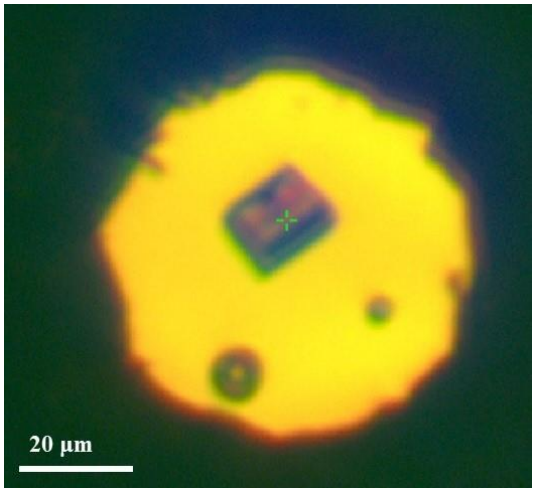

Figure 3.1.1.2: DAC1 at 50 GPa before laser heating.

After the laser heating the spectra were collected at two different points of the sample (position 1 and position 2) (Fig. 3.1.1.3.a and Fig. 3.1.1.3.b).

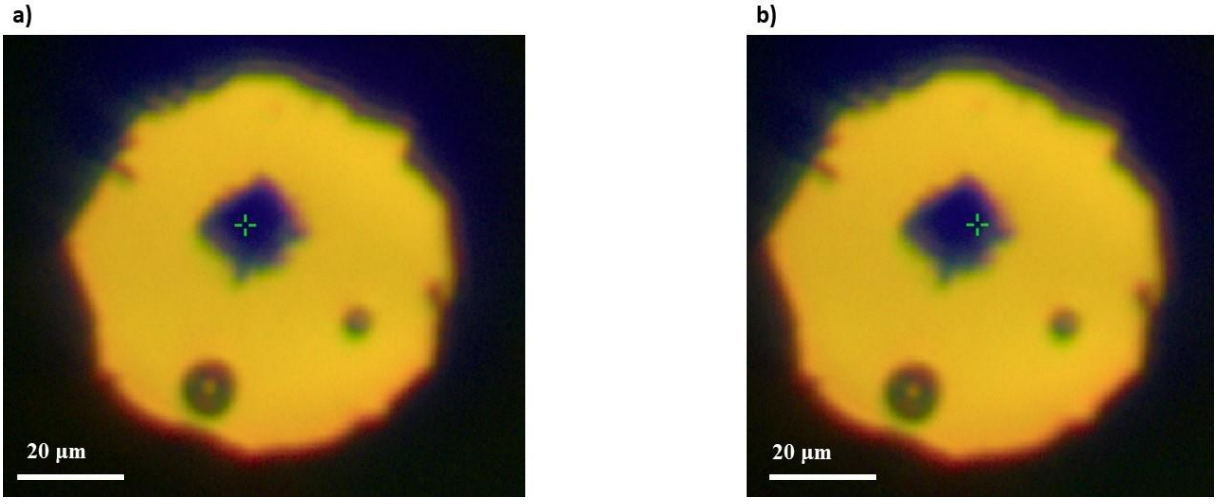

Figure 3.1.1.3: a) DAC1 after laser heating position 1 and b) DAC1 after laser heating position 2.

For the second DAC, we compressed the sample at pressure step of 4/5 GPa from ambient pressure to 100 GPa and we were able to collect a total of 17 spectra. All spectra were collected in the same point of the sample, roughly in the middle of the crystal (Fig. 3.1.1.4).

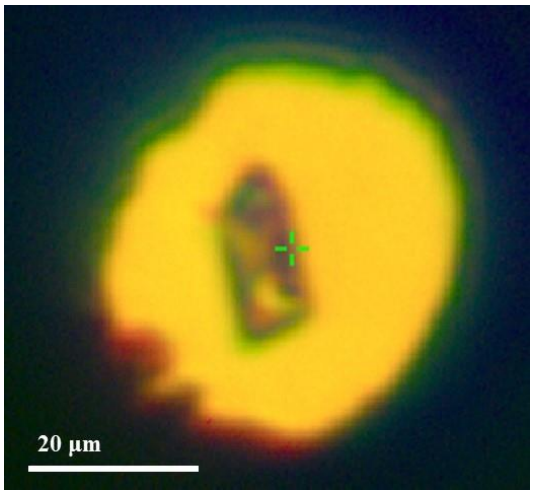

Figure 3.1.1.4: DAC2 at 5.5 GPa.

After the laser heating at 100 GPa we collected two more spectra in two different positions of the sample (area A and area B) (Fig.3.1.1.5).

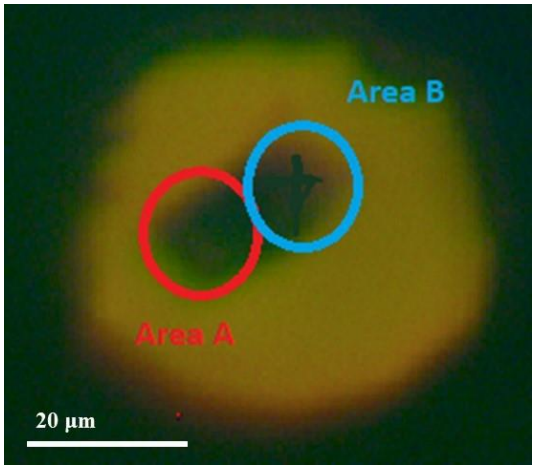

Figure 3.1.1.5: DAC2 after laser heating at 100 GPa.

In order to estimate the energy resolution of the source, before and after all measurements we collected the spectrum of a known material, a single line absorber characterised by a single line in the Mössbauer spectrum (chemical formula: $K_2Mg^{57}Fe(CN)_6$), from which it is possible to deconvolute the full width half maximum (FWHM) of the source. This is necessary to obtain the right calibration parameters and

perform reliable fittings, thus to extract correct hyperfine parameters from the measured spectra.

3.1.2 Data analysis

All spectra were fitted using the software package MossA [47]. Before starting with the sample spectra fitting procedure, I retrieved the FWHM of the source. For SMS measurements the shape of the source function is Lorentzian squared and the FWHM of the source is estimated by fitting the source FWHM to a single line absorber, as explained above. For this, normally two absorber spectra, called Single Line (SL), are collected before and after each sample run. The average of the deconvolution of the FWHM of the two SL will give the source FWHM. It is important to measure the FWHM of the SL absorber before and after each sample collection because even the smallest variation of external variables such as atmospheric pressure or temperature might affect, slightly, the energy resolution of the source. Another important thing to consider for the spectral fitting, is that ID18 is equipped with confocal Beryllium lenses (CRLs) and a Be-window along the X-ray beam path. The former is used to preliminary focus the X-ray beam to a smaller beam diameter while the latter is necessary to preserve the vacuum in one of the monochromator chambers while letting the X-rays going through with the smallest attenuation. Beryllium metal always contains traces of iron, which is visible in the Mössbauer spectrum as an extra component. Because the iron contamination is very low, the component has extremely low intensity, but should nevertheless be taken into account during the fitting process. This component does not change and is always characterized by the same hyperfine parameters, which are known and can be added manually in MossA. The input parameters are given in the following Table 3.1.2.1.

CS	FWHM	Int	QS	A12
0.1557 mm/s	0.3286 mm/s	0.0167844	0.4029 mm/s	0.25

Table 3.1.2.1: Lorentzian doublet to add to correct for Fe in Be lenses.

3.1.2.1 DAC 2 before laser heating

For the analysis I tried different fitting combinations, including different fitting functions (Lorentzian and Pseudo-Voigt), different approaches with A12 parameters (asymmetry of the peaks), and possibly constrains in QS and CS fitting ranges. From the performed fittings I noticed that the residual noise could be slightly improved using a Pseudo-Voigt fitting function instead of a Lorentzian line. However, the choice of the fitting functions does not influence the value of the hyperfine parameters obtained from the fitting. The fittings presented here were made with Lorentzian line

and using the lowest number of components, i.e. one component for the initial X site (Fe^{2+} in high spin in octahedral coordination) and one component for the Y site, which comes out at around 52 GPa. The appearing of a second component could indicate i) a structural transition, ii) an electronic transition, i.e. high spin (HS) to low spin (LS) or iii) a pressure induced change in the valence state (see Discussion). I tried different strategies to fit the high-pressure two-component spectra. Initially, I allowed the A12 parameter of the two doublets to vary without any constrain, then I imposed the A12 parameter to be equal, i.e. same asymmetry, in both doublets and finally, I repeated the fittings allowing the A12 parameter to vary only for the X site (Fe^{2+} starting octahedral site) up to about 52 GPa. From the emergence of the Y site, I blocked the A12 to 0.5 for the X site (symmetric condition) and allowed to vary only the Y site. I adopted this choice because the X site becomes progressively symmetric with pressure (Fig. 3.1.2.1.1, 1-9), and applying this constrain for the fitting of spectra collected at P > 50 GPa reduces the unknown variables and possible sources of error. Moreover, the change in symmetry of the doublet is probably caused by an increase in coordination number of the X site from octahedral to dodecahedral (see hyperfine parameters in Table 3.1.2.1), whereas the Y site seems to adopt an octahedral coordination. Because the Goldanskii-Karyagin effect should not affect cubic sites, I decided to block the possible asymmetry for the X site starting at 52 GPa, but it might be this happened also at slightly lower pressures. I could fit the Mossbauer spectra with two doublets also starting from 44 GPa since from the spectral fitting I notice the appearance of a small shoulder at 44 GPa, which however does not affect so much the hyperfine values of the X site. The choice of how to treat the parameter A12 mainly influences the CS trend of X and Y sites.

At the end, for the motivation given before, I used the third approach to fit the spectra. The results are displayed below (Fig. 3.1.2.1.1 and Table 3.1.2.1).

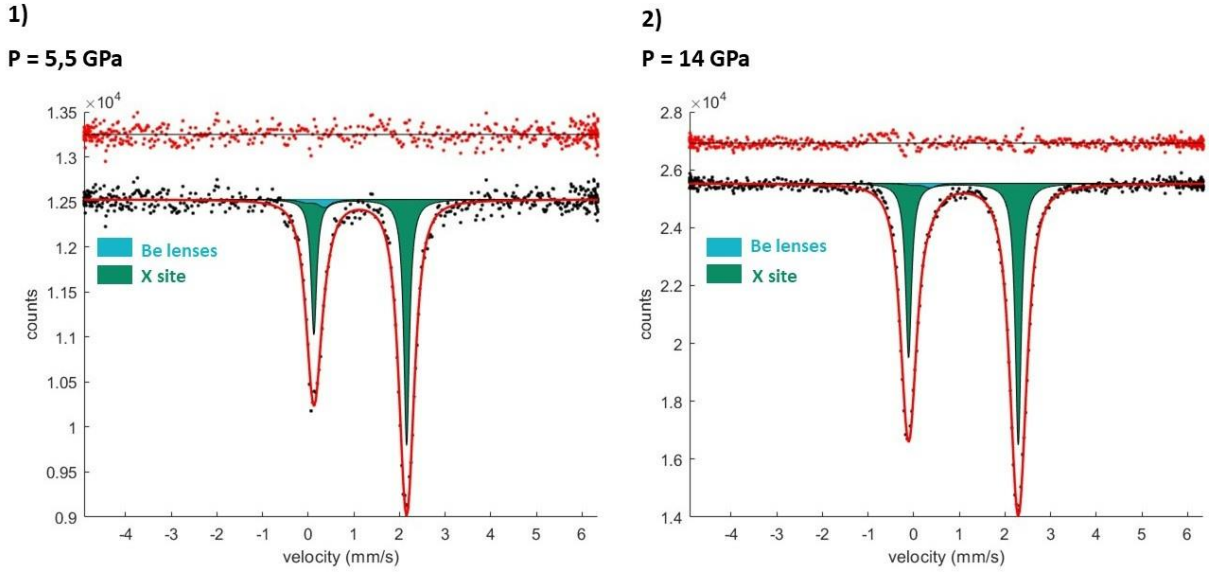

3)

P = 17 GPa

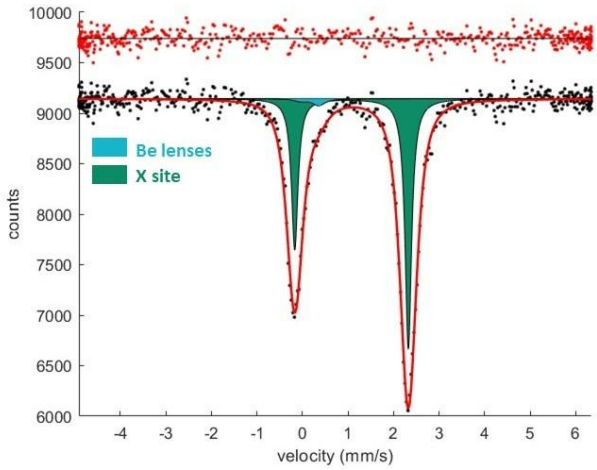

4)

P = 21 GPa

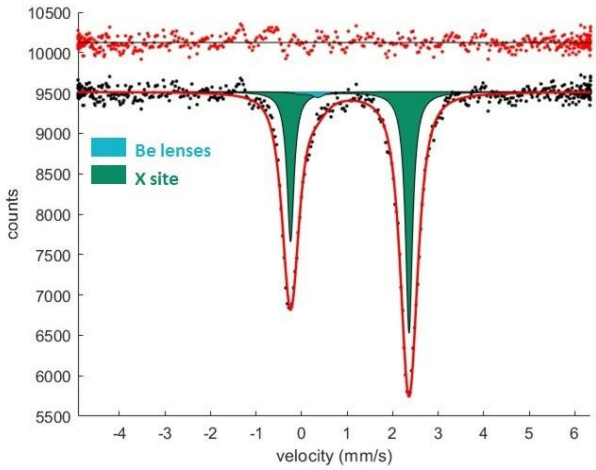

5)

P = 24 GPa

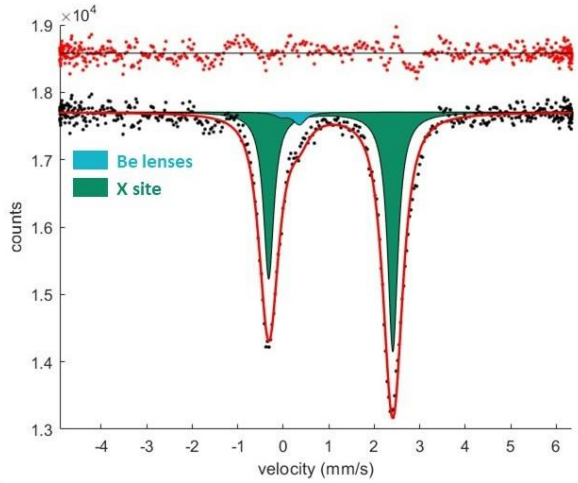

6)

P = 29 GPa

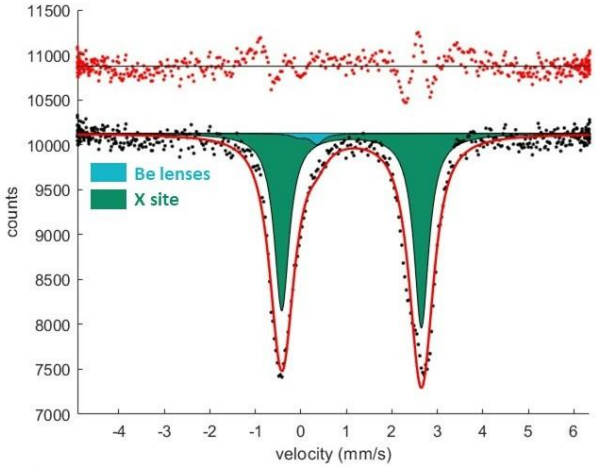

7)

P = 34 GPa

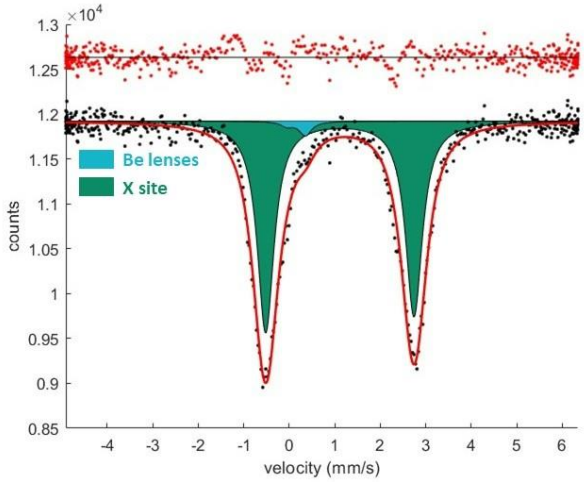

8)

P = 39 GPa

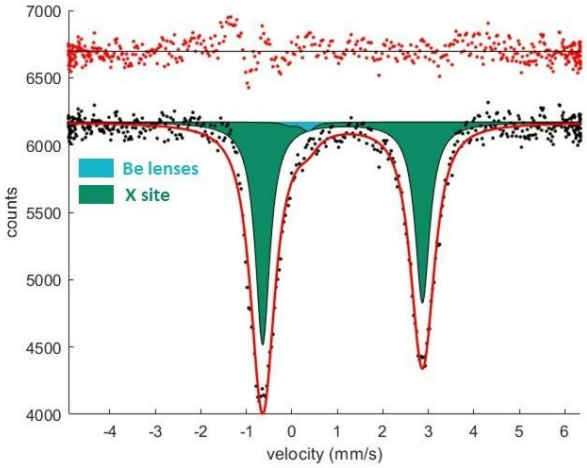

9)

P = 44 GPa

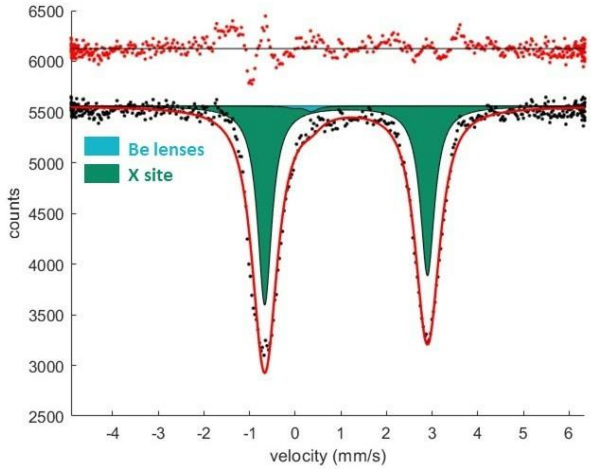

10)

P = 52 GPa

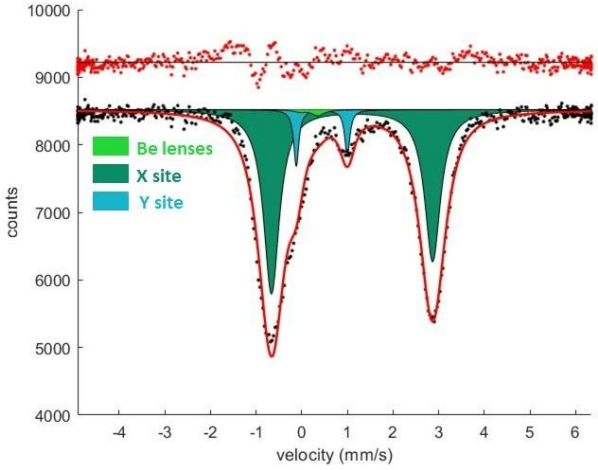

11)

P = 56 GPa

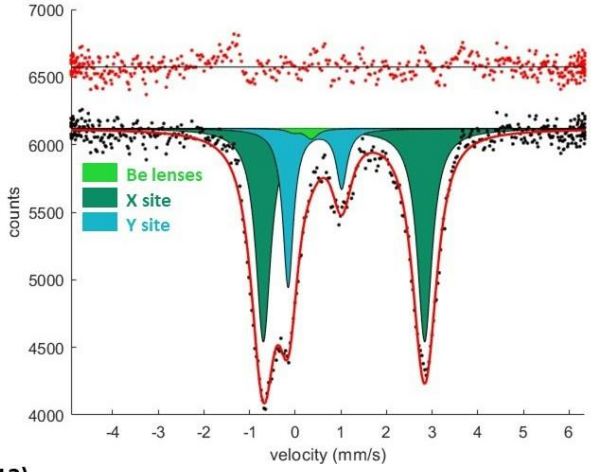

12)

P = 62 GPa

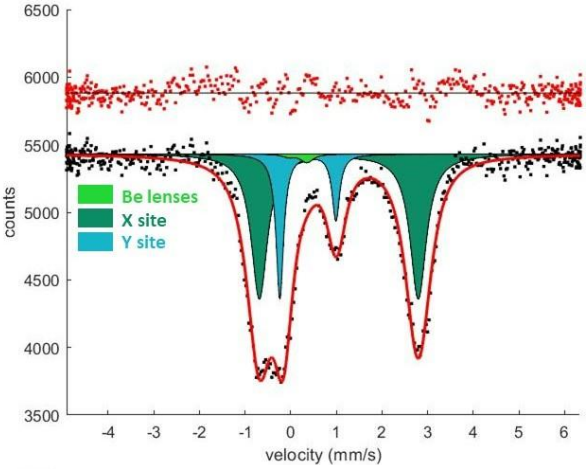

13)

P = 67 GPa

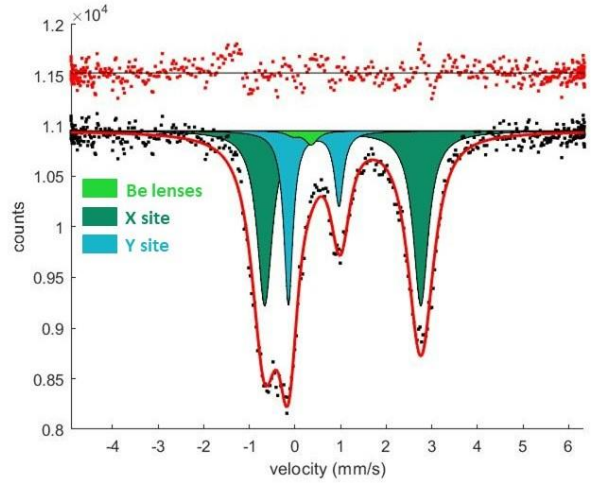

14)

P = 69 GPa

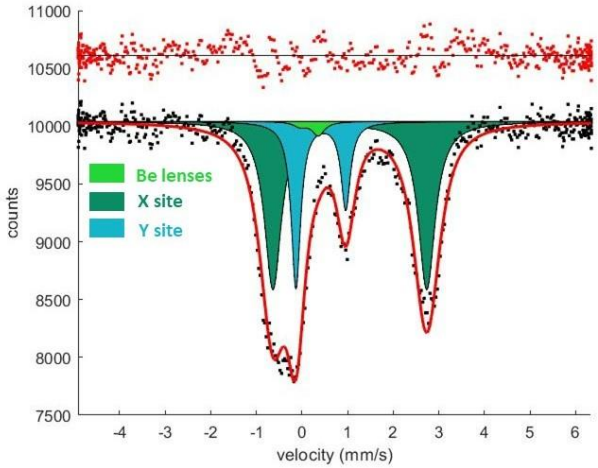

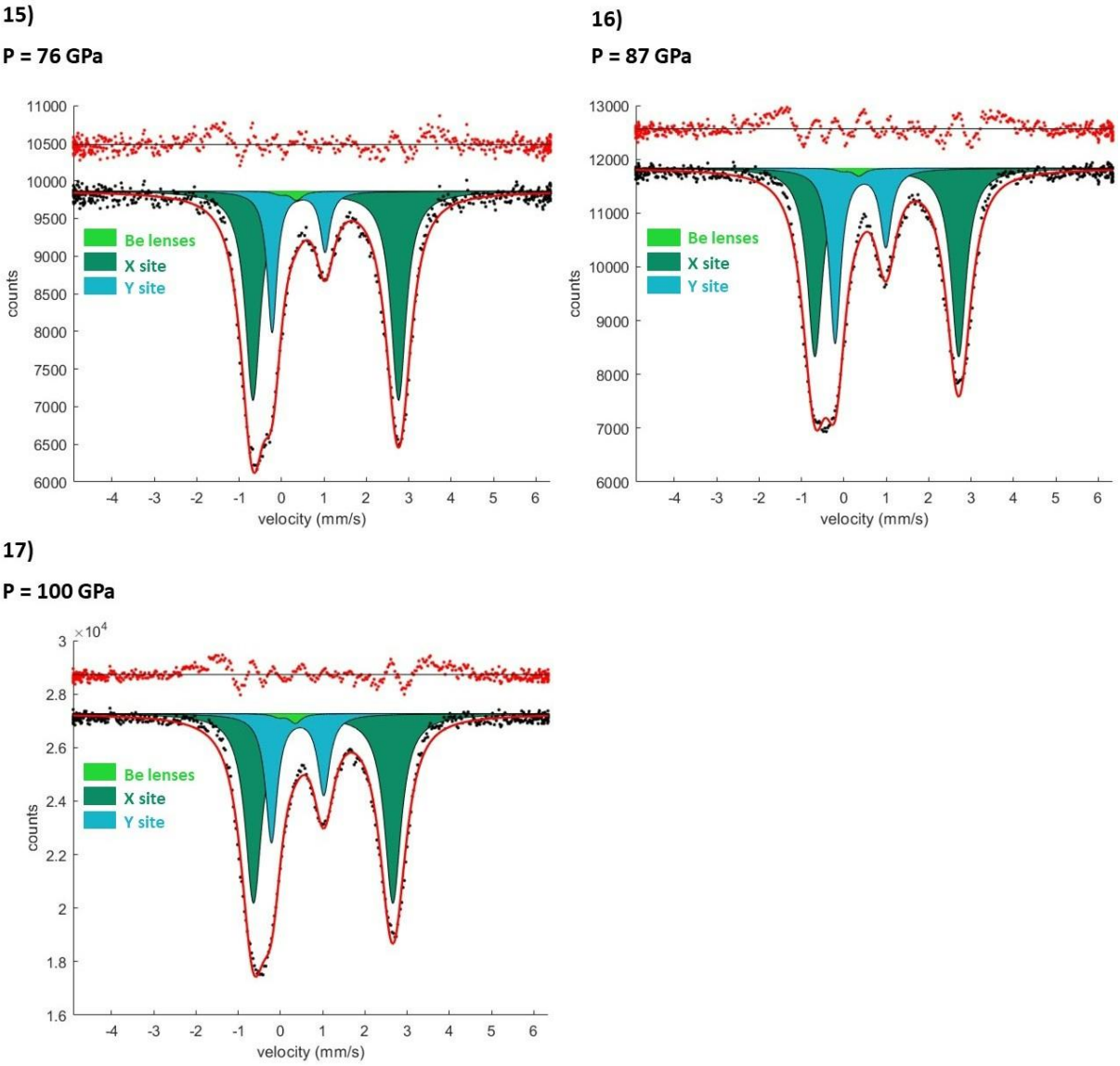

Figure 3.1.2.1.1: Mössbauer spectra fitted using MossA software package. Dark green doublet: Fe^{2+} in HS state in Fe-oxalate dihydrate X-site. It shows an evolution from octahedral coordination to dodecahedral (or higher) coordination at increasing pressures. Blue doublet: Fe^{2+} in Y-site. Discussions about the electronic configuration and coordination environment can be found in the Results and Discussions chapters. Light green asymmetric doublet: Be-lenses + Be-window component.

From Figure 3.1.2.1.1 one can notice that at low pressures only one doublet (X site) is visible in the spectrum. Between 17 GPa and 34 GPa there is a change in the asymmetry of the doublet, which is indicated by the swap of the peaks intensities. Above 34 GPa, a moderate asymmetry remains, constant, with the left pick as the most intense one. This could be caused by the distortion of the unit cell of the crystal and to the phase

transition confirmed by XRD and Raman data (Chapter 3.2.2 and 3.3.2), also in accordance with the preliminary studies made by Müller et al. [1]. At 52 GPa another doublet starts to appear and at 100 GPa both doublets are still present. To better understand these spectra, I plotted the center shift and quadrupole splitting of the two sites. From the comparison of the hyperfine parameters obtained from the fitting and the ones found in the literature (Fig. 3.1.2.1.2), I can affirm that at low and moderate pressures, the doublet of the X site represents Fe^{2+} in HS state in octahedral coordination (CS = 1.14 mm/s and QS = 2.03 mm/s at 5.5 GPa). At increasing pressures, one can notice a progressive increase of the QS values, which indicate a possible distortion of the site and change in coordination environment from octahedral to dodecahedral (CS = 1.11 mm/s and QS = 3.57 mm/s at 44 GPa). At 52 GPa another doublet starts to appear, which I attribute most certainly to a spin transition of the Fe^{2+} 3d electrons from the dodecahedral HS site to a new octahedral LS configuration, Y-site.

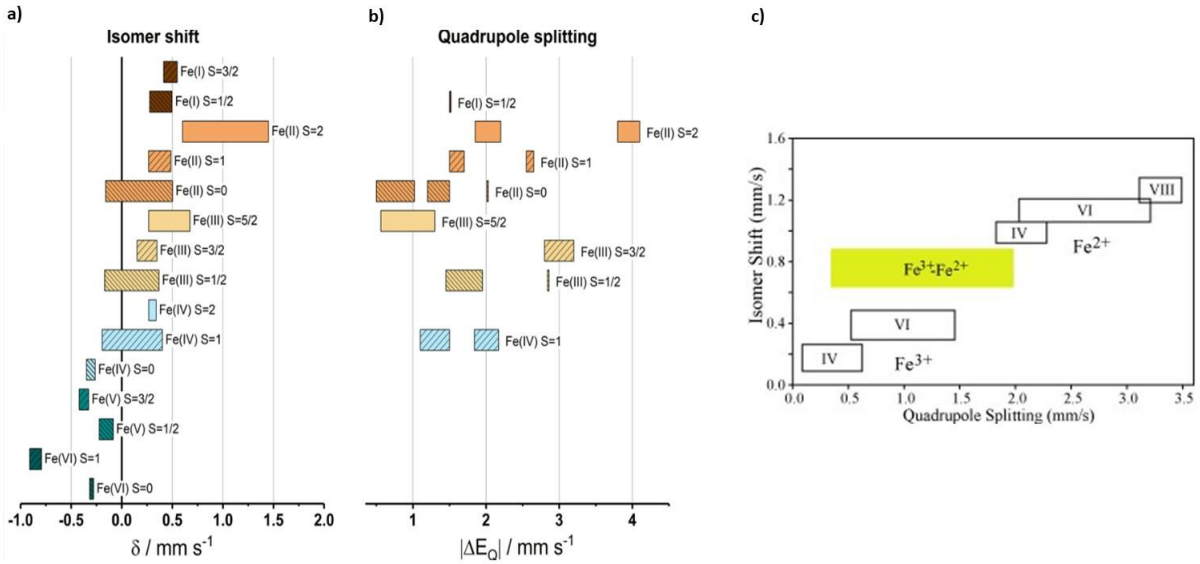

Figure 3.1.2.1.2: Hyperfine parameters: a) CS for Fe in different spin configurations, b) QS for Fe in different spin configuration and c) CS and QS for Fe^{3+} and Fe^{2+} in different coordination.

I also plotted the evolution of hyperfine parameters at the increase of pressure. In particular, center shift and quadrupole splitting are plot at the increase of pressure for the two sites in Figure 3.1.2.1.3. I identified different regions representing changes in the atomic or electronic structures, highlighted in Figure 3.1.2.1.3 using straight lines of different colors. These regions are identified in accordance with the XRD data.

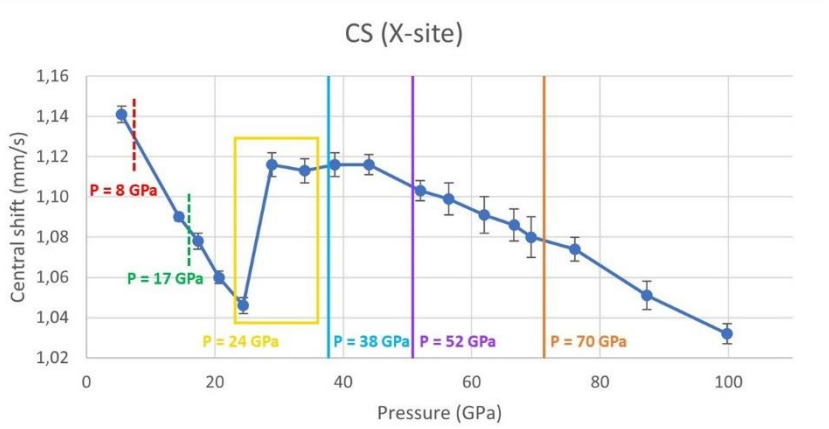
CS (X-site)
Central shift (mm/s)
1,16
1,14
1,12
1,10
1,08
1,06
1,04
1,02
P = 8 GPa
P = 17 GPa
P = 24 GPa
P = 38 GPa
P = 52 GPa
P = 70 GPa
0
20
40
60
80
100
Pressure (GPa)

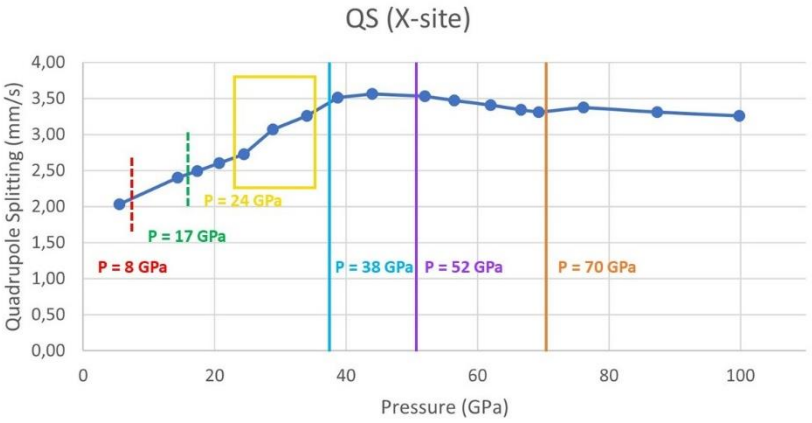
QS (X-site)
Quadrupole Splitting (mm/s)
4,00
3,50
3,00
2,50
2,00
1,50
1,00
0,50
0,00
P = 24 GPa
P = 17 GPa
P = 8 GPa
P = 38 GPa
P = 52 GPa
P = 70 GPa
0
20
40
60
80
100
Pressure (GPa)

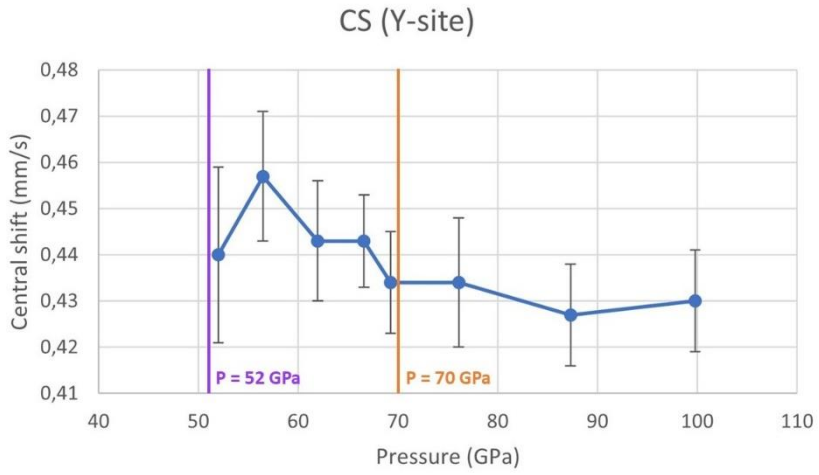
CS (Y-site)
Central shift (mm/s)
0,48
0,47
0,46
0,45
0,44
0,43
0,42
0,41
P = 52 GPa
P = 70 GPa
40
50
60
70
80
90
100
110
Pressure (GPa)

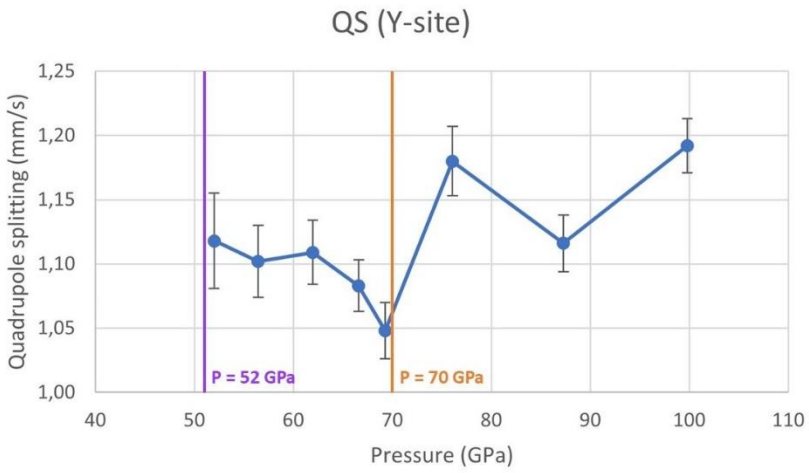

Figure 3.1.2.1.3: Evolution with pressure of CS and QS of X site and Y site. (In QS of X site, the error bars are smaller than points identifying data). The dashed lines indicate the pressures at which in the integrated patterns (XRD) there are changes due not to phase transitions but to artifacts.

It is useful to see these trend because the CS and QS are sensitive to the pressure. In particular, the central shift is sensitive to the s-electron density at the nucleus, while the quadrupole splitting measures the electric field gradient (EFG) caused by a non-symmetrical charge distribution around the nucleus (see Chapter 2.2.1).

From Figure 3.1.2.1.3 and Table 3.1.2.1 I notice an initial decrease of the CS for the X site at the increase of pressure, which I attribute to the rise of the s electron density at the Fe nucleus due to the progressive reduction of interatomic distances during compression. The decrease in CS with pressure while preserving the same structure is a well-known effect, i.e. [48, 49]. Between 24 GPa and 29 GPa there is a jump in the CS from 1.046 mm/s to 1.116 mm/s, which then remains more or less constant until 44 GPa. In the same pressure interval, around 38 GPa I observed from XRD data the completion of a sluggish structural transition which started at P > 22 GPa (see Discussion in Chapter 3.2.2), which coincide with the stabilization of the QS of the X site doublet. At the appearance of the second doublet at 52 GPa, the CS of both sites start to decrease again. A sudden increase in CS is indicative of a phase transition with a change in coordination environment, in this case the X site goes from octahedral to dodecahedral coordination and this means that the electronic cloud is more expanded and so the rise in CS values (CS increases because iron coordination increases). Instead, at 52 GPa, when the spin crossover is supposed to take place, the electronic cloud becomes more compact because the higher energy 3d electrons are paired to the lower energy ones in the same orbital and therefore the CS decreases again. From the evolution of the QS values, I notice that the QS for the X site increases with pressure

until ~ 40 GPa, which can be explained by a continuous distortion of the X site caused by progressive not uniform distribution of the electric field gradient around the Fe nuclei. This evolution confirms that compressing the sample the distortion of the X site is changing and from the obtained value I can affirm that the Fe^{2+} is switching from an octahedral to a dodecahedral coordination. At the emergence of the second doublet the value of the QS of X site remains more or less constant, showing only a tiny decrease that might indicate a slow but progressive gain in site symmetry due to the growth and appearance of the Y site. On the other hand, the QS of the Y site follow a more complicate path, at first it decreases until 70 GPa and then increase again until the highest pressure studied. Looking carefully at the evolution of the QS of the X site, I notice that at 24 GPa the slope of the straight line changes. This is indicative of the fact that at this pressure a new structure starts to appear (this is confirmed by XRD data (Chapter 3.2.2)). For this reason, I could potentially fit the spectra with two doublets, one representing the new structure (site 2) growing at the expenses of the lower pressure one (site 1). This is also evidenced by the increase in FWHM of the doublet, and it is a further confirmation of a sluggish transition. An example of fitting with two doublet is given in Figure 3.1.2.1.4.

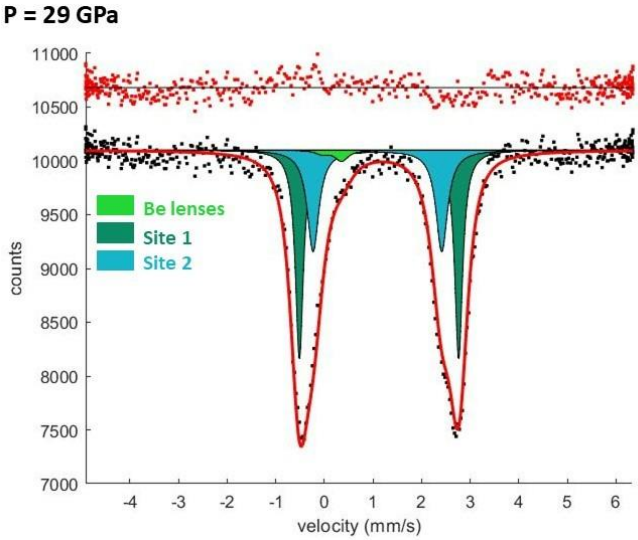

Figure 3.1.2.1.4: Mössbauer spectrum at P = 29 GPa fitted with two doublets using MossA software package: site 1 represents the lower pressure structure and site 2 represent the new structure.

After 40 GPa the QS reaches a plateau, a clear indication of the full conversion of our sample to the new high pressure structure.

3.1.2.2 DAC 2 after laser heating

Once reached the target pressure, i.e. 100 GPa, the sample was laser heated. We annealed two different areas at different temperatures (in area A T_{max} ~ 2400K and in

area B T_{max} ~ 2950K) in order to verify whether there is an effect on the synthesis of the products. For this reason, we acquired two spectra in the two different positions.

From a preliminary analysis made with CrysalisPro, we found a known phase, a tetracarbonate already discovered few years ago [13], namely the orthocarbonate $Fe_4C_3O_{12}$ in which all iron is ferric (Fe^{+3}) and in which there are two structurally distinct iron position. The Fe atom in position 1 is surrounded by nine O atom forming a regular trigonal prism while the Fe atom in position 2 is coordinated to 7 oxygens forming a bicapped trigonal prism. The presence of other phases, e.g. iron oxides of different stoichiometries, in not excluded. Therefore, in the fitted Mössbauer spectra, I will expect to see at least two different Fe site. Although a precise characterization of the pure phase using Mössbauer spectroscopy is difficult due to the possible presence of other iron compounds in the laser-heated sample.

The spectra acquired in area A and B are similar and can be fitted with the same number of components (Fig. 3.1.2.2.1).

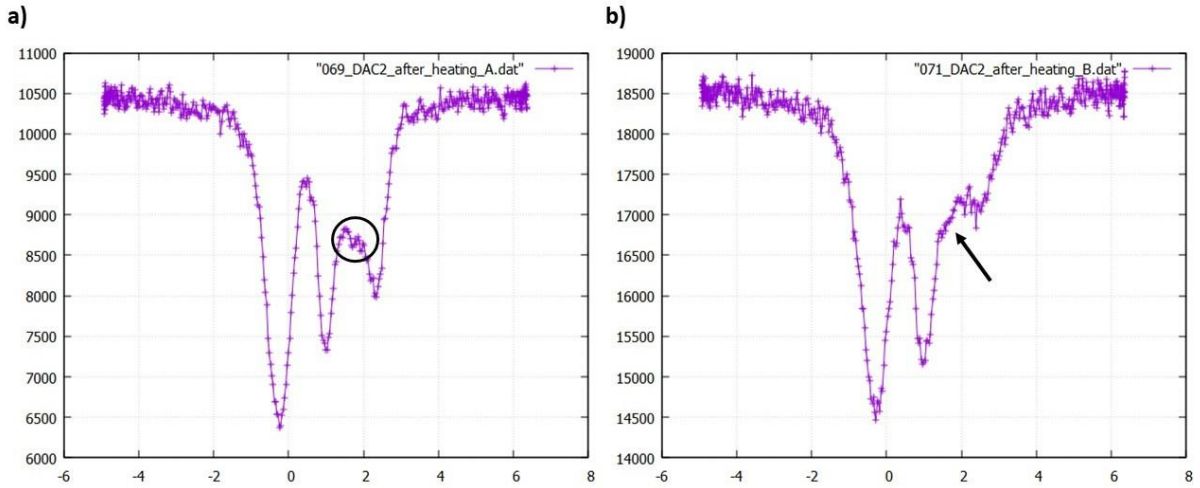

Figure 3.1.2.2.1: Mössbauer spectra: a) DAC 2 at 100 GPa after LH in area A, T ~ 2400 K and b) DAC 2 at 100 GPa after LH in area B, T ~ 2950 K.

In both spectra, I can notice the presence of two dominant peaks in the left part of the spectra and the presence of another peak towards the right side. The intensity of this peak is higher in Figure 3.1.2.2.1.a respect the one present in Figure 3.1.2.2.1.b. This difference is due to the different temperature reached in the two area during laser heating. From the spectra it is also clear that in reality this is a peak of another doublet. Indeed, I can see the presence of an extra very small peak (highlighted with a black circle) in in Figure 3.1.2.2.1.a and of shoulder (highlighted with an arrow) in Figure 3.1.2.2.1.b.

The analysis of this spectra with MossA is still in progress and we should carefully check and compare the hyperfine parameters in order to confirm the presence of the ferric iron in the two sites. This analysis should be also combined with the analysis of XRD data.

The following Figure 3.1.2.2.2 shows a preliminary fitting attempt of the spectra with MossA using with Lorentzian line, no constrain in hyperfine parameters and using the lowest number of components, i.e two doublets for the two sites of the orthocarbonate structure.

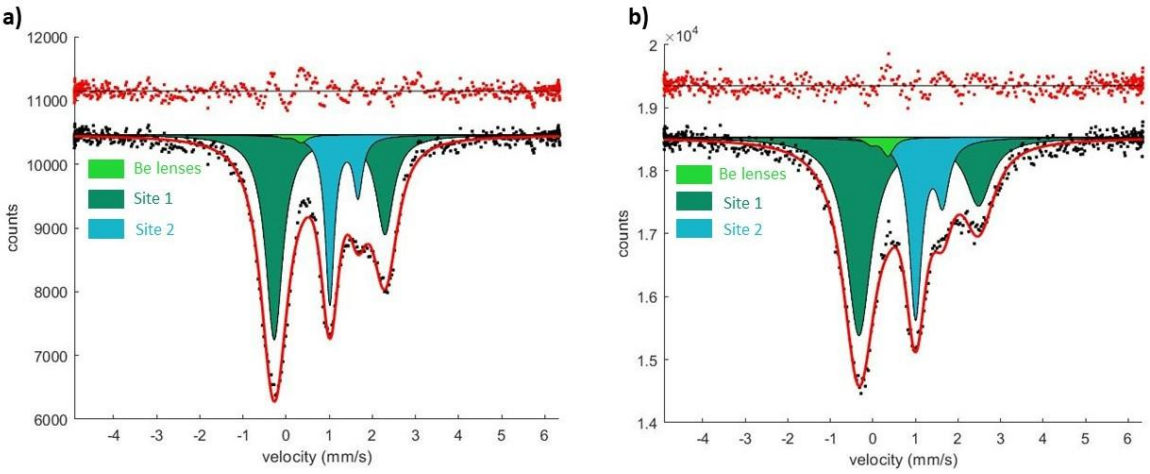

Figure 3.1.2.2.2: Mössbauer spectra fitted using MossA software package: a) DAC 2 at 100 GPa after LH in area A and b) DAC 2 at 100 GPa after LH in area B.

The hyperfine parameters of the two sites are reported in the Table 3.1.2.2.

From the value in Table 3.1.2.2, I can notice that the two sites have similar values and this confirm that during the laser heating we formed the same products in the two different area.

3.1.2.3 DAC 1 before laser heating

The fitting, presented here, was made with Lorentzian line and using the lowest number of components, i.e. one component for the initial X site and one component for the Y site, which from the analysis made before on DAC 2 (Chapter 3.1.2.1), I know appears at P ~ 52 GPa.

Figure 3.1.2.3.1 shows the fitted spectrum recorded from DAC1 at 50 GPa in comparison with the one measured from DAC 2 at 52 GPa.

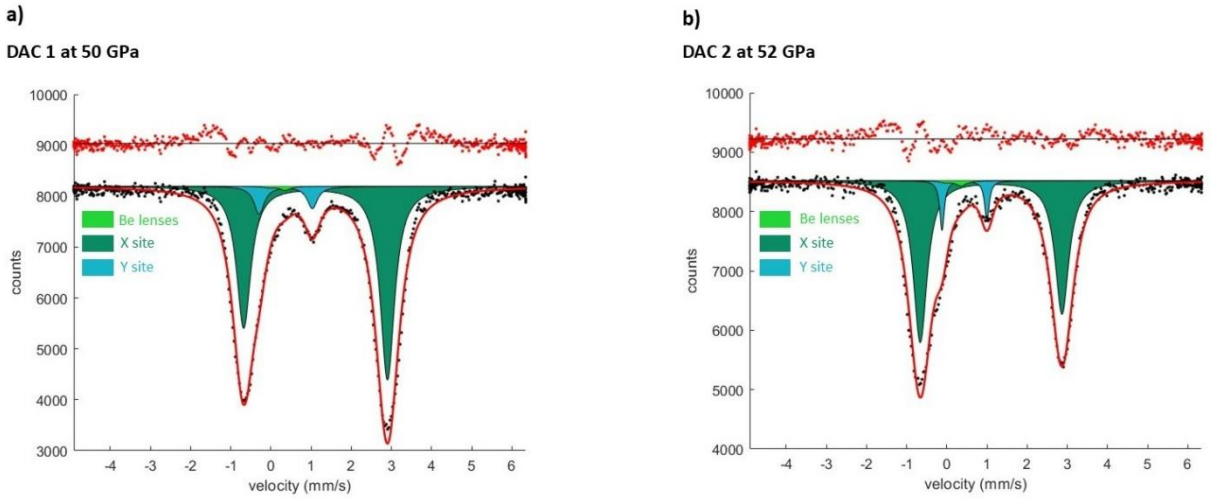

Figure 3.1.2.3.1: Mössbauer spectra fitted using MossA software package: a) DAC 1 at 50 GPa and b) DAC 2 at 52 GPa.

From Figure 3.1.2.3.1 and Table 3.1.2.1 I confirm that both spectra can be fitted with two doublets, one for the X site that correspond to Fe^{+2} in low spin configuration and one for the Y site that corresponds to Fe^{+2} in high spin configuration (see value of hyperfine parameters in Table 3.1.2.1). The difference between the two spectra is the asymmetry of the doublet of X site, which most likely is caused by the different crystallographic orientation of the two crystals with respect to the polarized beam of the synchrotron. However, having not measured the Mössbauer spectra of DAC1 before 50 GPa, I cannot affirm with certainty the origin of this difference of the two spectra. Nevertheless, despite this difference, the hyperfine values (Table 3.1.2.1) found in the two cases are in perfect agreement within error, so I can affirm that in both case we observe the same structural evolution, i.e the X site hosts Fe^{+2} that starts in octahedral coordination and high spin state, then at the increase of pressure the X site becomes progressively larger, a dodecahedral environment, while the Y site that appears around 50 GPa corresponds to Fe^{+2} in low spin state and probably in octahedral coordination.

3.1.2.4 DAC 1 after laser heating

The sample was laser heated at 50 GPa and annealed for several minutes at 2000(100) K, even if the highest measured temperature at the beginning of the heating was ~ 4000 K. We acquired two spectra in two different positions (position 1 and position 2).

From a preliminary analysis made with CrysalisPro we were able to synthesize at least two new products, a new tetracarbonate $Fe_5C_3O_{13}$, where there is a combination of Fe^{2+} and Fe^{3+} and another phase that for the moment remains unidentified.

The spectra acquired in position 1 and 2 (Fig. 3.1.2.4.1) are different and this is in agreement with what it was found from XRD preliminary analysis. Indeed the difference in the two spectra could be due to the fact that in position 1 and 2 are present different products respectively. Or perhaps the same products but in completely different proportions.

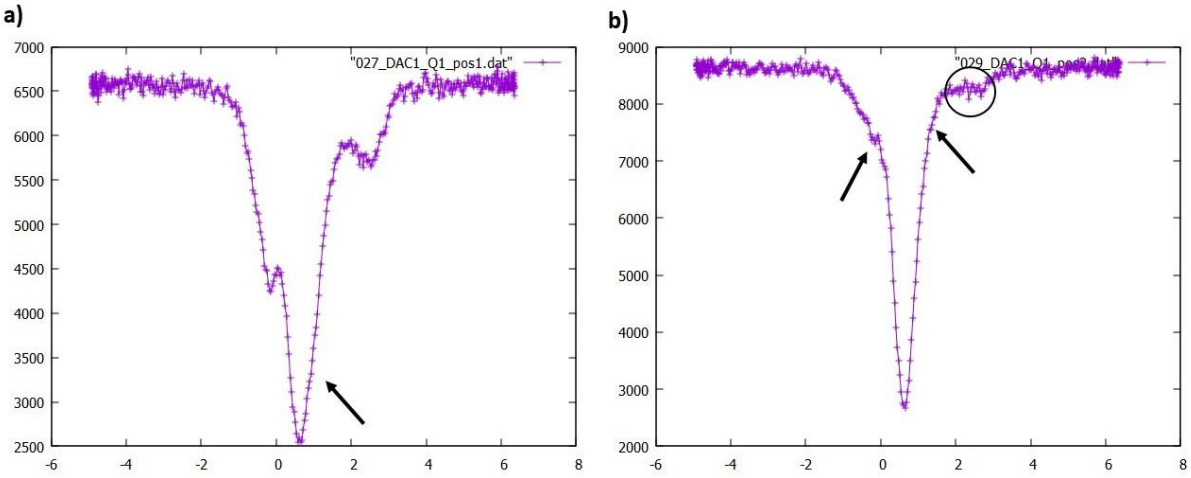

Figure 3.1.2.4.1: Mössbauer spectra: a) DAC 1 at 50 GPa after LH in position 1 and b) DAC 1 at 50 GPa after LH in position 2.

From the spectrum in Figure 3.1.2.4.1.a it is evident that the more intense peak in the middle is due to combination of at least two peaks from two different components. Indeed in this peak there is the presence of a tiny shoulder in the right part (highlighted with black arrow). Hence, this spectrum could be fitted with two doublets, one for the site of Fe^{2+} and the other for the site of Fe^{3+}, and a singlet, probably due to Fe^{2+} in LS state. On the other hand, the fitting of the spectrum presented in Figure 3.1.2.4.1.b seems more complicated. However, if one look carefully at the two spectra (a and b), it is possible to notice that the main differences rise by a non-identical ratio between the components' intensities, so that they both can be fit using two doublets and one singlet with similar hyperfine parameters, but different intensities. Even if the nature of the two doublets is not clear, from the hyperfine parameters of the singlet it is possible to assign it to octahedrally coordinated Fe^{2+} in LS state. The analysis of this spectra with MossA is still in progress and should be combined with the analysis of XRD data to confirm the hyperfine values found in Mössbauer spectroscopy in comparison with the structure found with XRD.

Figure 3.1.2.4.2 shows a fitting attempt for the spectra, made using MossA with Lorentzian function lines, no constrain in hyperfine parameters and using the lowest number of components.

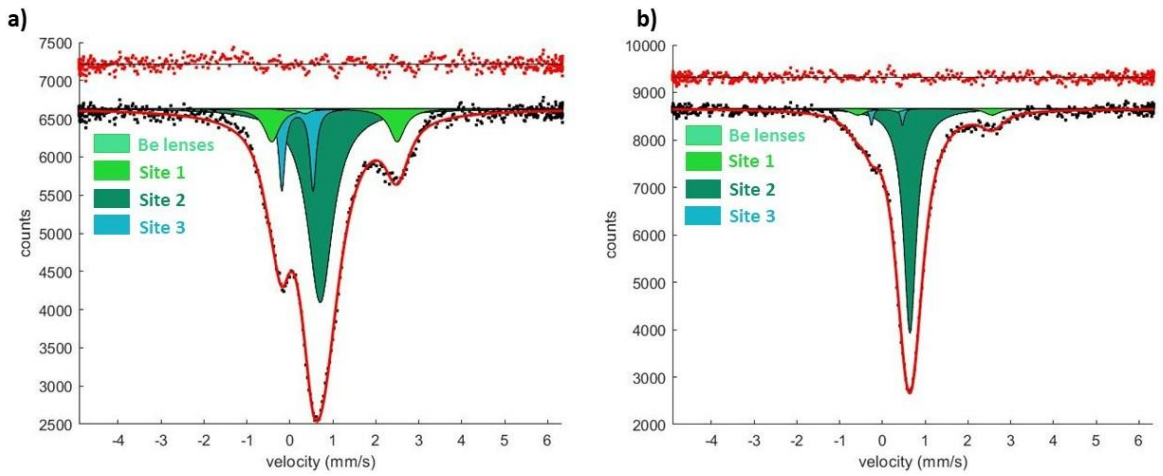

Figure 3.1.2.4.2: Mössbauer spectra fitted using MossA software package: a) DAC 1 at 50 GPa after LH in position 1 and b) DAC 1 at 50 GPa after LH in position 2.

The hyperfine parameters of the two sites are reported in the following Table 3.1.2.2.

From the value in Table 3.1.2.2, I can notice that the sites have similar values and this could confirm that in the two different position there are the same products but in completely different proportions.

P (GPa)	Doublet	CS (mm/s)	QS (mm/s)	FWHM (mm/s)	Int (%)	A12 (mm/s)
5.5(5)	Site X	1.141(4)	2.032(8)	0.150(11)	94.3(0)	0.355(9)
14.4(5)	Site X	1.090(2)	2.403(4)	0.233(6)	97.2(0)	0.400(4)
17.4(5)	Site X	1.078(4)	2.494(8)	0.172(11)	95.8(0)	0.377(8)
20.6(5)	Site X	1.060(3)	2.602(7)	0.190(10)	96.7(0)	0.383(7)
24.4(5)	Site X	1.046(4)	2.728(8)	0.278(12)	95.4(0)	0.410(7)
28.9(5)	Site X	1.116(6)	3.068(12)	0.400(19)	96.9(0)	0.477(9)
34.0(5)	Site X	1.113(6)	3.260(11)	0.449(17)	96.7(0)	0.520(7)
39.7(5)	Site X	1.116(6)	3.512(12)	0.392(18)	97.5(0)	0.552(9)

44.0(10)	Site X	1.116(5)	3.566(10)	0.380(16)	98.4(0)	0.540(8)
50.2(10)	Site X	1.113(7)	3.580(14)	0.434(14)	89.4(15)	0.422(14)
	Site Y	0.370(29)	1.325(58)	0.309(71)	9.5(13)	0.557(75)
52.1(10)	Site X	1.103(5)	3.531(11)	0.420(16)	89.4(14)	0.548(7)
	Site Y	0.440(19)	1.118(37)	0.136(56)	8.9(12)	0.548(7)
56.6(10)	Site X	1.099(8)	3.474(16)	0.465(24)	80.4(17)	0.500(0)
	Site Y	0.457(14)	1.102(28)	0.174(42)	17.7(15)	0.556(9)
62.0(10)	Site X	1.091(9)	3.405(18)	0.505(28)	75.9(18)	0.500(0)
	Site Y	0.443(13)	1.109(25)	0.188(36)	22.2(13)	0.554(9)
66.6(10)	Site X	1.086(8)	3.345(17)	0.527(26)	74.1(16)	0.500(0)
	Site Y	0.443(10)	1.083(20)	0.180(30)	23.4(15)	0.562(8)
69.3(10)	Site X	1.080(10)	3.310(20)	0.545(30)	72.7(19)	0.500(0)
	Site Y	0.434(11)	1.048(22)	0.194(32)	24.5(17)	0.560(9)
76.1(20)	Site X	1.074(6)	3.373(12)	0.481(18)	83.4(13)	0.500(0)
	Site Y	0.434(14)	1.180(27)	0.196(39)	15.0(12)	0.544(7)
87.3(20)	Site X	1.051(7)	3.312(13)	0.487(20)	76.2(14)	0.500(0)
	Site Y	0.427(11)	1.116(22)	0.240(31)	22.4(13)	0.564(7)
99.8(20)	Site X	1.032(5)	3.260(11)	0.499(16)	76.1(12)	0.500(0)
	Site Y	0.430(11)	1.192(21)	0.302(29)	22.3(11)	0.531(5)

Table 3.1.2.1: Hyperfine parameters of DAC1 and DAC2 under compression. All Mössbauer spectra in compression were collected using DAC2 except for P-points 5.5, 14.4 and 52.1 GPa, which were called using DAC1.

P (GPa)	LH (K)	Site	CS (mm/s)	QS (mm/s)	FWHM (mm/s)	Int (%)	A12 (mm/s)
50.2(10) (DAC 1)	2000(100) (Pos. 1)	Green Doublet	1.038(21)	2.918(44)	0.435(68)	14.5(10)	0.500(0)
		Singlet	0.706(17)	/	0.722(38)	70.1(14)	/
		Blue Doublet	0.176(21)	0.725(47)	0.176(52)	14.4(11)	0.500(0)
	2000(100) (Pos. 2)	Green Doublet	0.997(46)	3.140(102)	0.439(71)	3.4(12)	0.500(0)
		Singlet	0.646(6)	/	0.358(14)	88.5(15)	/
		Blue Doublet	0.108(57)	0.725(124)	0.097(98)	3.6(11)	0.500(0)
99,8(20) (DAC 2)	2400(100) (Area A)	Green Doublet	1.010(8)	2.568(16)	0.485(19)	70.4(12)	0.675(8)
		Blue Doublet	1.343(14)	0.655(25)	0.257(26)	28.0(11)	0.742(18)
	2950(100) (Area B)	Green Doublet	1.080(14)	2.813(28)	0.709(28)	66.7(14)	0.750(9)
		Blue Doublet	1.323(19)	0.637(30)	0.358(35)	30.5(12)	0.750(20)

Table 3.1.2.2: Hyperfine parameters of DAC1 and DAC2 after laser heating.

3.2 X-Ray Diffraction (XRD)

3.2.1 Experiment HC-5141 at ID15b (ESRF)

The XRD spectra were acquired at ID15b at the ESRF in Grenoble (France) during the experiment HC-5141. The XRD data were collected using the same pre-selected Fe-oxalate single crystals measured also with SMS. In order to do XRD experiment at extreme pressure, we used the membrane cells provided by the European

Synchrotron. We compressed the samples to 50 GPa and 100 GPa and collected XRD spectra in situ, during compression, using two different DACs as described in Chapter 3.1. DAC1, that reached 50 GPa, had a cullet of 300 μm while DAC2, that reached 100 GPa, had a cullet of 150 μm. Both DACs had rhenium gaskets and were gas load with neon used as PTM to maintain quasi-hydrostatic conditions. Both DACs were prepared by loading a $FeC_2O_4 \times 2\ H_2O$ single crystal and a smaller ruby crystal.

The pressure was increased using an automatic pressure-drive controlled from outside the hutch, thus there was no need to break the interlock and perform the hutch search at every pressure increase. The pressure was measured using the integrated Photo-Ruby-Luminescence (PRL) system present at the beamline, which correlates the shift of ruby fluorescence lines with pressure. Since the highest pressure reached with DAC2 was ~ 50 GPa, the pressure estimation was based on the calibration paper of Dewaele et al. 2008 [28] for hydrostatic ruby systems.

Single-crystal diffraction data were collected using the rotation method on the ID15B beamline of the ESRF [45]. The cell was rotated around the ω-axis from −36° to 36° for pressure below 8 GPa and from −33° to 33° for pressure above 8 GPa. 144 and 132 diffraction images with a step size of 0.5° and an exposure time of 0.2 or 0.3 s were collected for pressures below and above 8 GPa respectively. The XRD data were collected during operation in multibunch mode (7/8 + 1 filling), in parallel with the SMS beamtime. For the collection of each dataset, we used a EIGER2 X 9M CdTe (340x370 mm) flat panel detector. The detector to sample distance was 180 mm and the synchrotron radiation with a wavelength of 0,41 Å was focused, by compound refractive lenses, to a beam size of about $6 \times 6\ \mu m^2$.

Each XRD dataset took approximately 20 minutes to be collected and the calibration was made using a Si crystal as standard material.

As described in Chapter 3.1, the first DAC was laser heated at 50 GPa and the second one at 100 GPa using the double-sided infrared YAG laser heating system installed at ID18 at the ESRF.

The XRD spectra were collected at different pressure. In particular, DAC1 was compressed at pressure step of 3/4 GPa from ambient pressure to 50 GPa and we were able to collect 17 XRD patterns. After the laser heating at 50 GPa we performed again a diffraction measurement on the quenched products. While for the DAC2 we only acquired XRD patterns before and after the laser heating at 100 GPa.

3.2.2 Data analysis

The analysis of the XRD single crystal data with CrysAlis^{PRO} program is still in progress. As preliminary analyses, the diffraction images taken at each different pressure step have been merged to obtain a single wide angle image. In this way I was able to analyze the data as powder diffraction images, even if due to the nature of the interaction of the polarized synchrotron beam with the oriented single crystalline lattice, the intensities of each reflection could be over- or underestimated with respect to a real powder pattern. Figure 3.2.2.1 shows these wide angle images.

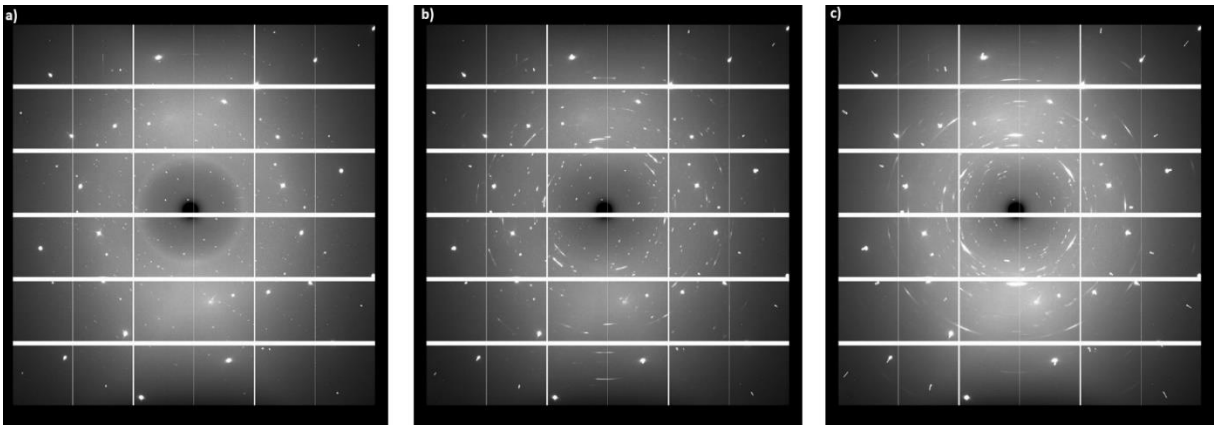

Figure 3.2.2.1: Dioptas images of DAC1: a) wide angle image of diffraction spots at 4 GPa, b) wide angle image of diffraction spots at 25 GPa and c) wide angle image of diffraction spots at 50 GPa.

From the Figure 3.2.2.1, it is clear that as the pressure increases the sample is compressed and so it starts loosing its crystallinity and becoming closer to a powder, but never completely. The difference from single crystal and powder XRD data is that in the first one we can clearly distinguish single spots at the angle of every reflection plane of the crystal (Fig. 3.2.2.1.a) while in the second one we start to observe circles that correspond to a specific angle of diffraction (Fig. 3.2.2.1.c). Indeed, the distinction between powder and single crystal diffraction is the degree of texturing in the sample. Single crystals have maximal texturing and are said to be anisotropic while in powered sample all the possible crystalline orientation are equally represented and for that they are said to be isotropic.

Here, I will present the preliminary and qualitative analysis made using the software Dioptas [50, 51] that is a Python-based program mostly used for fast integration and exploration of 2D X-ray diffraction Images.

For a proper data analysis, calibration is required. The correct detector geometry and sample to detector distance is easily set in Dioptos directly by loading the ''calibration file'' provided by ID15b after calibrating the sample environment with known samples, i.e. Si crystal or LaB_6 and CeO_2. Once the correct calibration is set, one can

start with the qualitative analyses of the sample XRD patterns. For this, Dioptas has another useful tool: the Mask module. Within the Mask module I could select regions I want to exclude from the image integration. A mask excludes specific areas from the integration process, which enables the removal of unwanted features such as, for example, diamond reflections in diamond anvil cell experiments, saturated peaks or detector blemishes. Therefore, before starting the analysis, I made a mask to hide the lines of the detector, the reflections coming the diamond, the rhenium of the gasket and the neon used as PTM (Fig. 3.2.2.2)

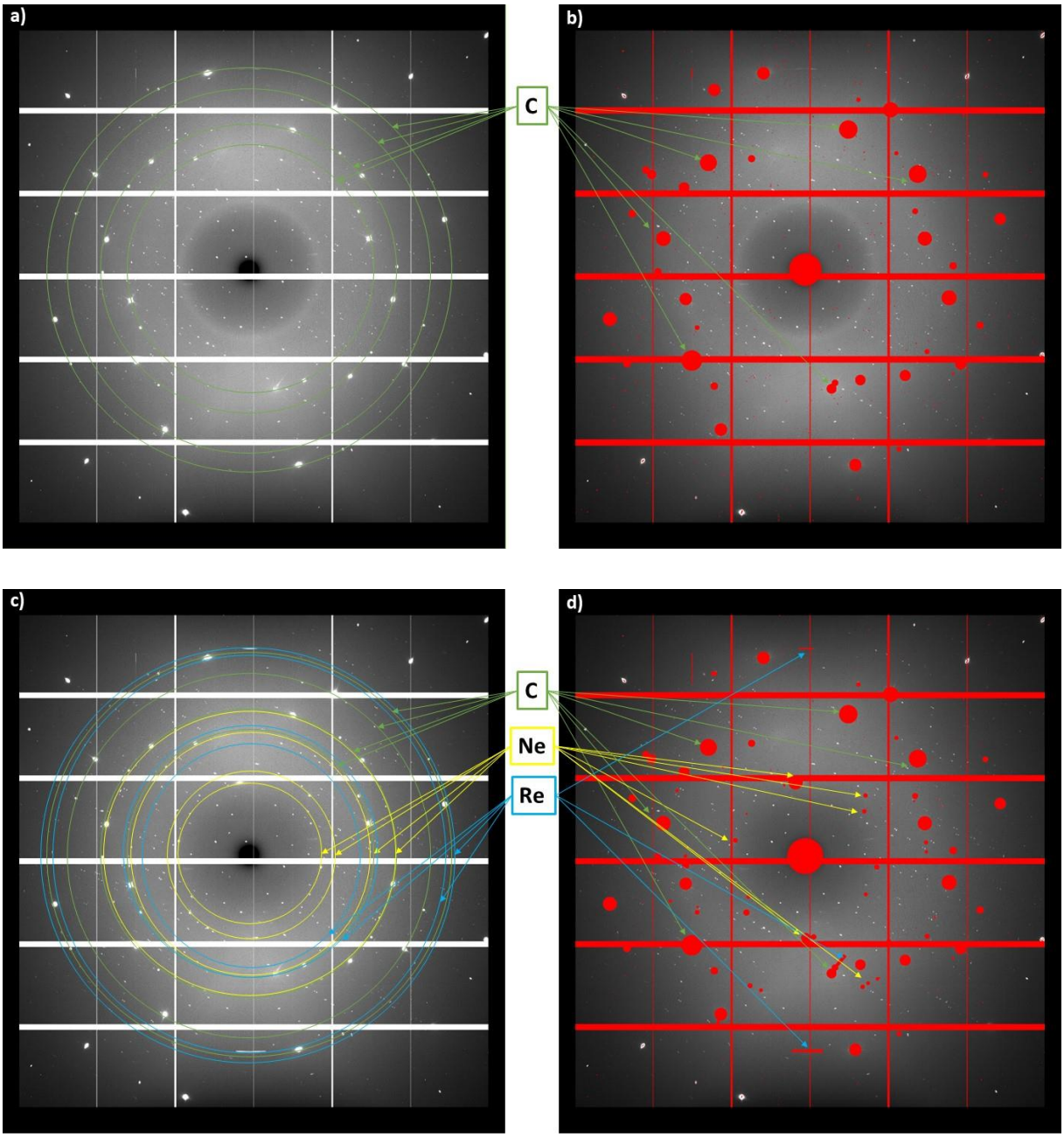

Figure 3.2.2.2: Dioptas images of DAC1: a) wide angle image of diffraction spots at 4 GPa, b) mask for diffraction spectra at 4 GPa, c) wide angle image of diffraction spots at 8.5 GPa and d) mask for diffraction spectra at 8.5 GPa. Highlighted in green, yellow and light blue circles are the C-diamond, Ne and Re spots, respectively.

The reflections caused by the diamond anvils are very easy to identify because they are very intense and always remain fixed as the pressure increases. Indeed, the sample was compressed increasing the pressure through the diamond culets but the diamonds themselves are not subject to it. On the other hand, the spots caused by rhenium and neon, that appear at 8 GPa, are more complicated to identify and they are influenced by the pressure. Therefore, as the pressure increases, they change position. In order to properly mask all these spots, I made a mask for each pressure point taken. Having masked the extra spots I can say that the diffraction pattern obtained from each image shows only the peaks due to our sample.

3.2.2.1 DAC 1 before laser heating

The Figure 3.2.2.1.1 shows all the integrated spectra obtained through Dioptas in the angle (2θ) range 2° to 44°.

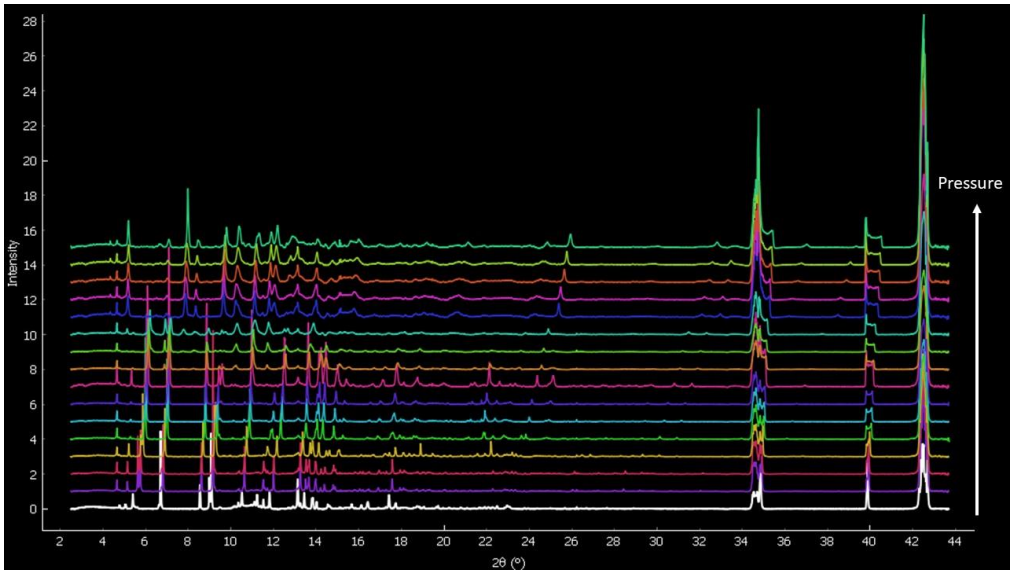

Figure 3.2.2.1.1: Integrated XRD spectra of DAC 1 at the increasing of pressure.

In order to better visualize the changes in the reflections, I normalized the integrated patterns with respect to the intensity and I plotted the patterns in different 2θ ranges. In particularly, I excluded the region above 42° because intense peak above 42° is not

due to the sample and I focused the analysis in two angular ranges: lower 2θ, i.e. between 3° - 20° (Fig. 3.2.2.1.2.a) and higher 2θ, i.e. between 20° - 42° (Fig. 3.2.2.1.2.b).

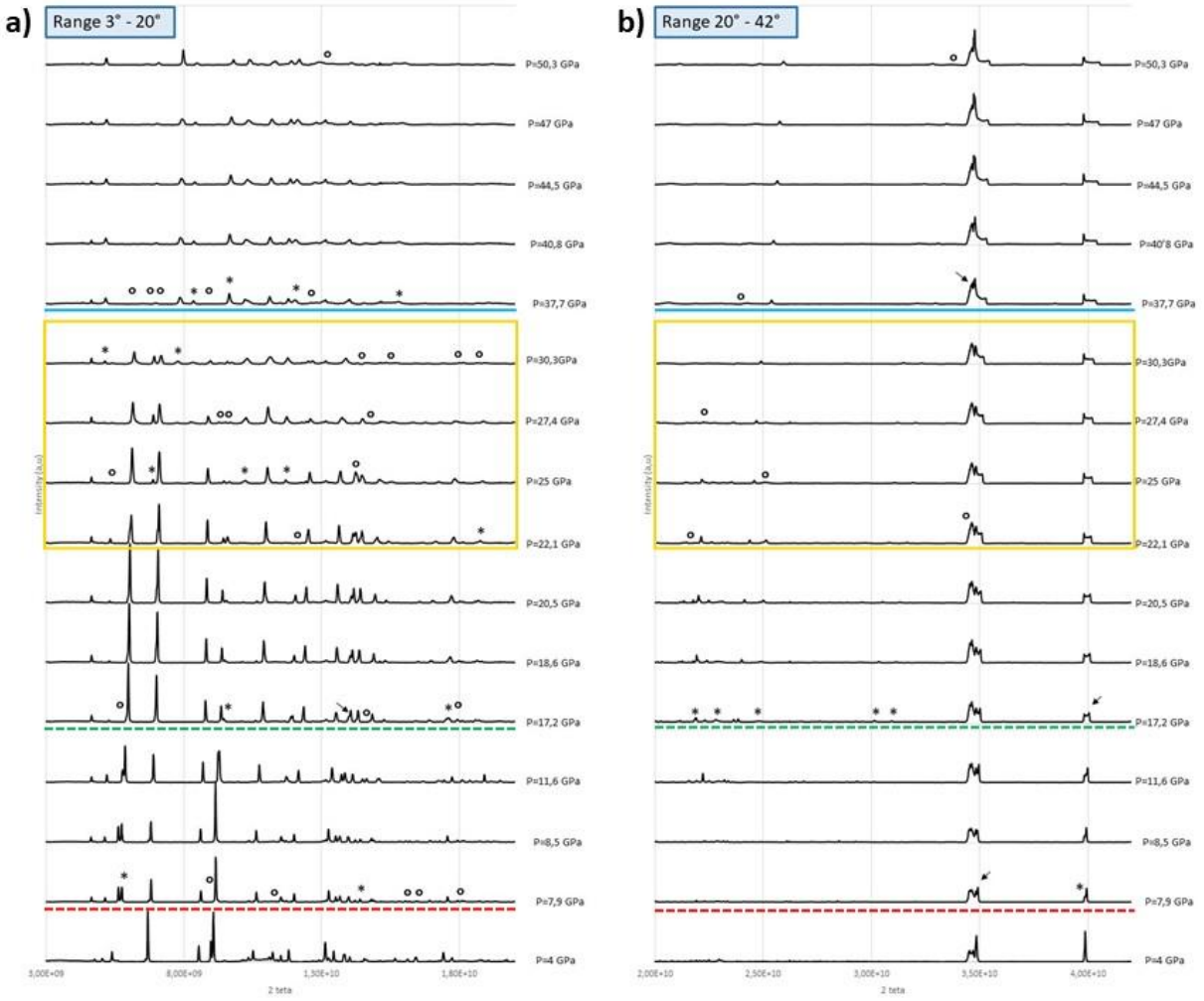

Figure 3.2.2.1.2: Integrated and normalized XRD patterns: a) angle range 2° - 20° and b) angle range 20° - 42°.

In Figure 3.2.2.1.2 I identified some regions in which we observe clear differences in the peaks position and intensities. Since I have merged together single crystal images to obtain powder-like wide angle images, it is better to focus on areas in the patterns where new peaks appear or existing peaks disappear rather than on changes in the peaks intensities. The latter might be untrue considering that we are treating single crystals data like powders, thus not representative for the real scattering intensities. In the XRD integrated patterns (Figure 3.2.2.1.2) I identified with asterisks the appearance of new peaks, with circles the disappearance of previous peaks and with arrows the evident variations in peaks intensity. Qualitatively, I could locate signs of possible structural changes already at 7.9 GPa, where new peaks emerge and others disappear.

This changes however are not in agreement with previous studies [1] and might be generated during the merging method, since we are treating single crystal data as powders and unwanted effect caused by twinning for instance cannot be avoided. Indeed, from the analyses of the single crystal data with CrysAlis^{PRO}, that are still ongoing, no structural changes were observed in this pressure range, but we could confirm that the crystal was initially twinned, thus formed by two distinct crystallographic domains characterized by two slightly different crystallographic orientations. Similarly, other changes observed at ~ 17 GPa are linked to the merging of integrated images from the two different crystallographic domains of the twinned crystal. At higher pressures instead, I noticed, in accordance with preliminary studies of Müller et al. [1], the evident appearance of new peaks starting at ~ 22 GPa, while reflections from the monoclinic structure get progressively lower in intensity. I interpreted this trend with the coexistence of two structures between 22 GPa and 38 GPa, the monoclinic structure of the oxalate at ambient conditions, observed until 38 GPa, and the one that begins to form at 22 GPa and that is completely formed at 38 GPa, which grows at the expenses of the low pressure one.

One should consider however that the progressive distortion of the monoclinic structure can cause a moderate shifts on the scattering angle of some reflections, not resulting however in a complete phase transition. Thus what we observe at 17 GPa might also be seen as a combination between distortion of the original monoclinic structure and twinning effects. I can affirm this because from previous studies [1] it is known that iron oxalate is very compressible and its structure undergoes distortions already at low pressures (~10 GPa).

3.2.2.2 DAC 1 after laser heating

Figure 3.2.2.2.1 shows the diffraction images of DAC1 at 50 GPa before and after laser heating.

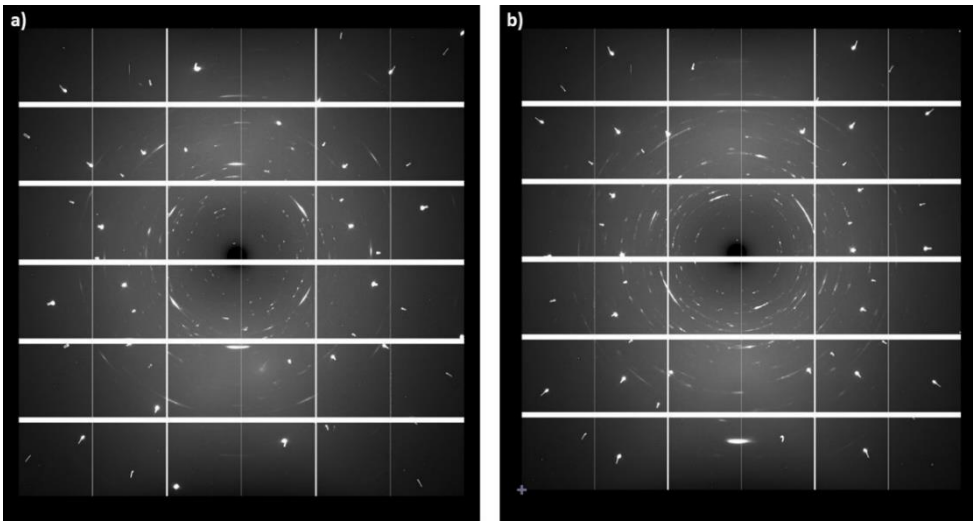

Figure 3.2.2.2.1: Dioptas images of DAC 1: a) wide angle image of diffraction spots at 50 GPa before laser heating and b) wide angle image of diffraction spots at 50 GPa after laser heating.

From the qualitative comparison of these 2D images it is already visible the difference between the diffraction patterns of the sample before and after heating. In Figure 3.2.2.2.1.b there are in general more spots (that at this pressure and after leaser heating start to look more like arcs) respect to Figure 3.2.2.2.1.a. This is the evidence that the sample transformed or decomposed to different phases. In general, after laser heating the 2D images always becomes more messy and it gets more difficult to correctly mask rhenium, neon and diamond features without also removing the signal from the sample.

From a preliminary analysis made with CrysalisPro we were able to identify at least two products, a new tetracarbonate $Fe_5C_3O_{13}$, where iron atoms are present in two different valence state, Fe^{2+} and Fe^{3+} (so not entirely oxidized) and which may contain OH group in its structure. The presence of OH groups in the tetracarbonate structure could have very interesting implications related to geoscience, as tetracarbonates might be possible water carriers down to the deep interior of the Earth via subducting slabs. Regarding the other phase, it remains unidentified. The analyses of the two new products are still in progress.

3.2.2.3 DAC 2 before laser heating

DAC2 was compressed to 100 GPa. The tiny culets (150 μm) and associated small hole in the gasket, caused unavoidable interactions between the tails of the X-ray beam and the rhenium gasket, so the presence of rhenium, neon and diamonds reflection is clear and the reflections are difficult to mask without the risk to remove also reflections from the sample. For these reasons I decided to mask only the spot of the diamond and to highlight with straight line the position where I expected to have Re and Ne peaks (Fig 3.2.2.3.1.b).

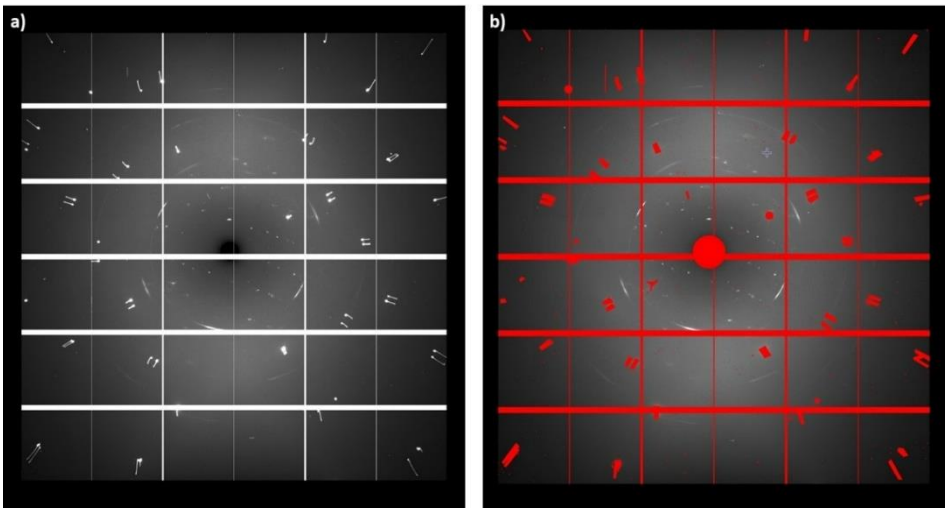

Figure 3.2.2.3.1: Dioptas images of DAC 2: a) wide angle image of diffraction spots at 100 GPa and b) mask for diffraction pattern at 100 GPa.

The Figure 3.2.2.3.2 shows the integrated pattern obtained through Dioptas in the angular (2θ) range 2° to 44°.

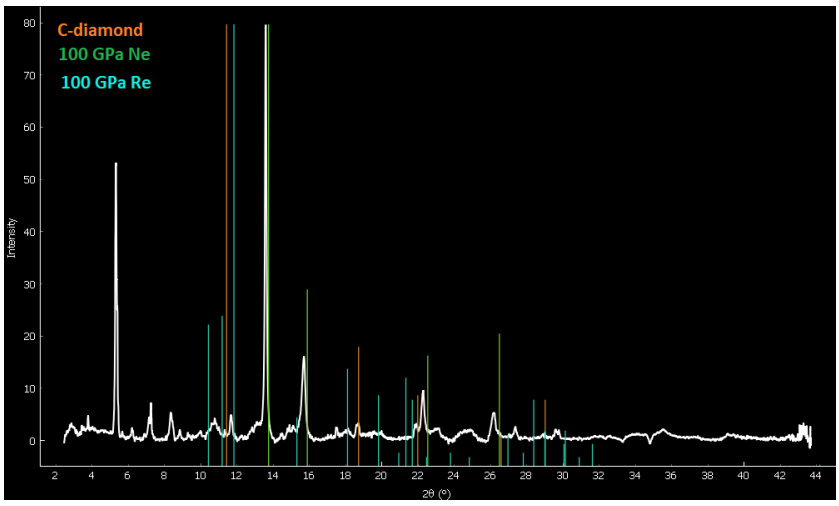

Figure 3.2.2.3.2: Integrated XRD spectrum of DAC 2 at 100 GPa.

3.2.2.4 DAC2 after laser heating

Also in this case it is difficult to correctly mask the rhenium, neon and diamond spots because the sample is compressed to very high pressure and also laser heated. Following the approach taken earlier, I decided to mask only the diamond reflections and to highlight with straight line the position in which I expected to see Re and Ne peaks (Fig 3.2.2.4.1.b).

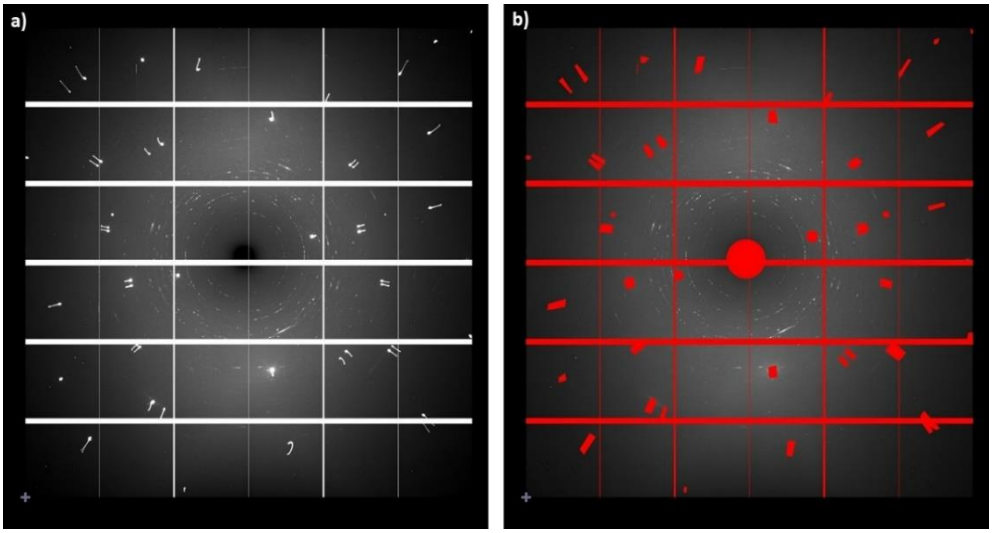

Figure 3.2.2.4.1: Dioptas images of DAC 2 after laser heating: a) wide angle image of diffraction spots at 100 GPa and b) mask for diffraction spectra at 100 GPa.

In Figure 3.2.2.4.1.a many new spots (or arcs) are visible in the 2D image compared to Figure 3.2.2.3.1.a. This is the evidence that the oxalate crystal changed, transforming or decomposing to one or more new products.

The Figure 3.2.2.4.2 shows the integrated spectrum obtained through Dioptas in the angular (2θ) range between 2° and 44°.

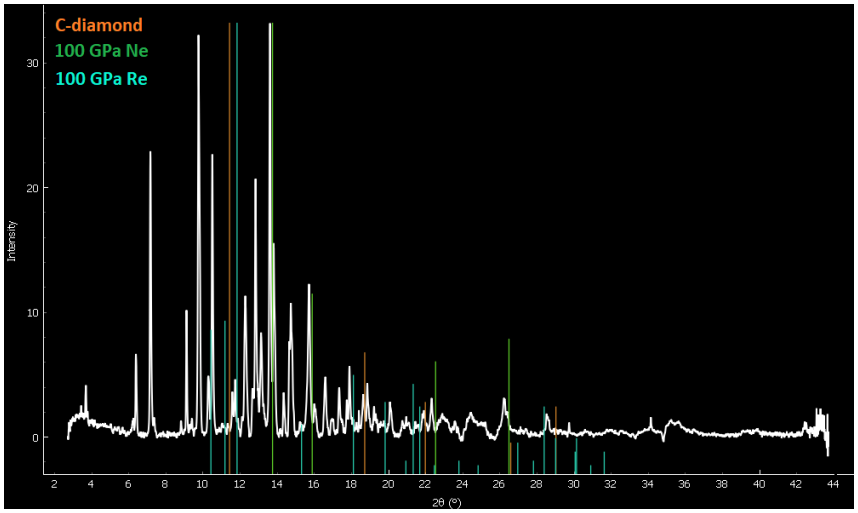

Figure 3.2.2.4.2: Integrated XRD spectrum of DAC 2 at 100 GPa after laser heating.

Figures 3.2.2.3.2 and 3.2.2.4.2 clearly show that after leaser heating the structure of the sample is changed. Indeed, after laser heating a lot of new peaks are present in the integrated image. In order to better visualized the difference in the integrated pattern I plot the XRD patterns of DAC2 before and after leaser heating in Figure 3.2.2.4.3.

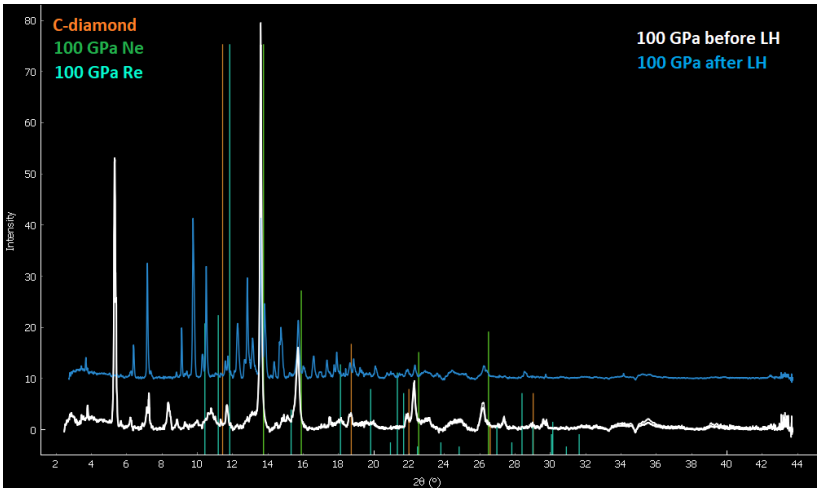

Figure 3.2.2.4.3: Integrated XRD spectra of DAC 2 at 100 GPa before laser heating (white line) and after laser heating (blue line).

From a preliminary analysis made with CrysalisPro, I know that we synthesized a known phase, a tetracarbonate already discovered few years ago, also called tetrairon(III) orthocarbonate $Fe_4C_3O_{12}$. The presence of other phases is expected, considering that oxalate oxidation should come with the reduction of something else, i.e. carbon, and several reflections were not indexed. In previous studies [13], the transformation of $FeCO_3$ was associated to the formation of $Fe_{13}O_{19}$ and diamond for instance, however other oxides are most likely to be present.

3.3 Raman Spectroscopy

3.3.1 Experiment at BGI

The Raman data were acquired at the BGI in Bayreuth. In order to do Raman experiment at extreme pressure, we used the piston-cylinder type BX90 mechanical DAC [24]. The DAC was prepared by loading a pre-selected (by XRD) $FeC_2O_4 \times 2\ H_2O$ single crystal. The sample was loaded in a DAC with cullet of 150 μm, rhenium gasket and the gas loading of the DAC was made with Ne. As described above, we used Ne gas as a PTM to preserve quasi-hydrostatic conditions during compression. We compressed the samples to 100 GPa and collected Raman spectra in situ, during compression. Pictures of the sample environment at different pressures are shown in (Fig. 3.3.1.1).

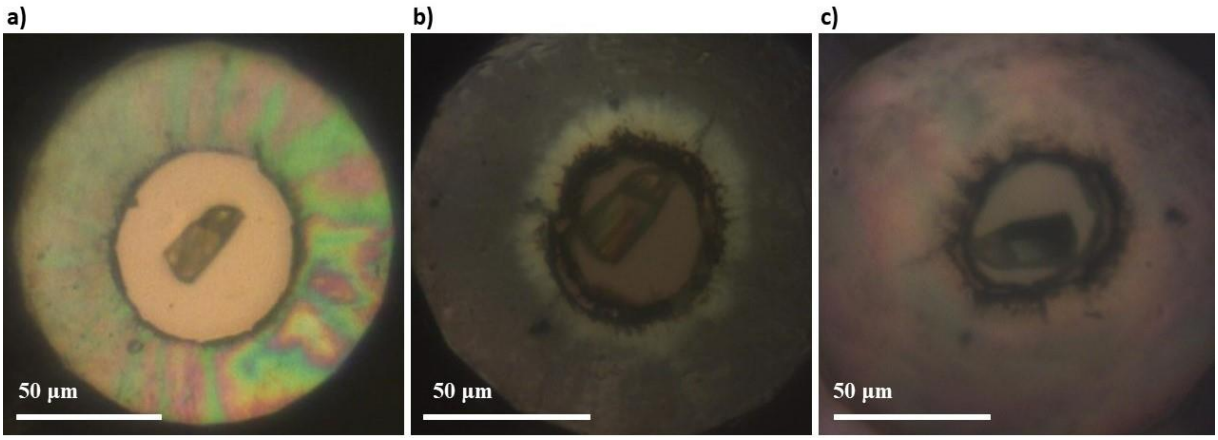

Figure 3.3.1.1: a) Sample in DAC (without Ne) at 1 bar, b) sample in DAC (loaded with Ne) at 2,5 GPa, c) sample in DAC (loaded with Ne) at 100 GPa.

Since the target pressure to reach was 100 GPa, we decided not to use the ruby fluorescence to estimate the pressure and did not load any ruby in the gasket hole. The pressure was measured through the shift of the wavelength of the Raman mode of the diamond culets. The correlation between the wavelength and the pressure was calculated using the web site ''Florescense pressure calculation and thermocouple tools'' [46] using the ''Diamond Raman tool''.

Raman spectroscopy was performed using the LabRAM HR developed by HORIBA. This system excites Raman modes using the 532 nm HeNe green laser with maximum output power of 10mW. The scattered radiation was collected and analyzed by the spectrometer Olympus BX40. The spectra were collected with magnification of 50 X.

Before loading the sample into the DAC, we acquired the spectrum at 1 bar. The spectrum was collected from 200 cm^{-1} to 3500 cm^{-1} (Figure 3.3.1.2).

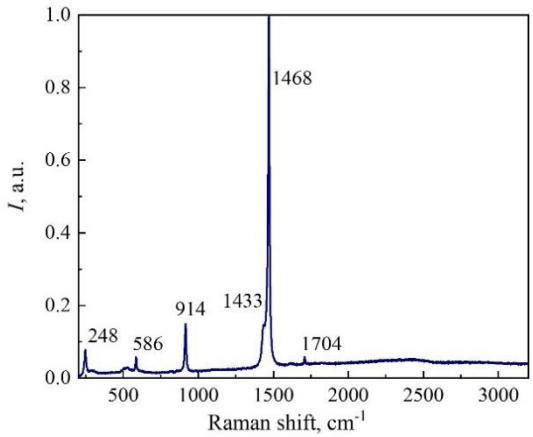

Figure 3.3.1.2: Raman spectrum in wide range (200 cm^{-1} - 3500 cm^{-1}) at ambient pressure.

After loading the sample in the DAC, we acquired spectra in different ranges of wavelengths and at different pressures. The DAC was compressed at pressure steps of 3/4 GPa from ambient pressure to 100 GPa and we collected a total of 20 spectra. For each pressure point, we first acquired a "rough" spectrum in a wide wavelength range (from ~ 200 cm^{-1} to ~ 1700 cm^{-1}) in order to check whether characteristic vibration bands from the sample were present at higher frequencies. In a second step, we acquired the spectra in two shorter wavelength ranges in order to reach a better spectral resolution of the spectra and to exclude the intense diamond mode, always present at ~ 1330 cm^{-1} due to the diamond anvils. The first range (short range 1) goes from ~ 200 cm^{-1} to ~ 1250 cm^{-1} and the second range (short range 2) is from ~ 1350 cm^{-1} to ~ 1700 cm^{-1}. During the acquisition of the spectra at different pressures, we changed the acquisition ranges towards longer wavelengths because we know that the bands move to higher frequencies when the pressure increase, unless there is a structural or electronic transition, which affect the molecular bonds length. We also changed the acquisition parameters, such as the exposure time and number of acquiring cycles (iteration), in order to optimize the quality of the data and the signal to noise ratio, i.e to improve the signal intensity vs the background. The first spectra, at lower pressure, were acquired in about 10 minutes. At P > 30 GPa the time of the acquisition increased to 30 minutes because we increased the exposure time and the number of iterations. Then for pressures above 50 GPa the acquisition time increased again to 50 minutes. In order to improve the quality of the date we also acquired the background caused by the laser interaction with the diamonds and the gasket at higher pressure.

3.3.2 Data analysis

The data were analyzed with OriginLab software [52]. In order to do the analysis, I subtracted to all spectra the background. In particular, for lower pressures (until 74 GPa) I subtracted the background manually, while at higher pressure (P > 78 GPa) I collected a separate background spectrum using the same exposure and iterations applied for the sample, which allowed for a precise background removal. The peaks in the spectra were fitted with a standard Gaussian function and considering all the fittings I obtained an R-squared (R^2) in the range between 0,89 – 0,98.

Here, I report on the Raman spectral evolution of Fe-oxalate compressed to 79 GPa. In particular, Figure 3.3.2.1.a shows the spectra collected in the short range 1 from 3 GPa to 79 GPa and Figure 3.3.2.1.b shows the spectra collected in the short range 2 from 3 GPa to 70 GPa. Above these pressures, the signal to noise ratio was too low to objectively recognize any mode from the sample (Fig. 3.3.2.2a and b).

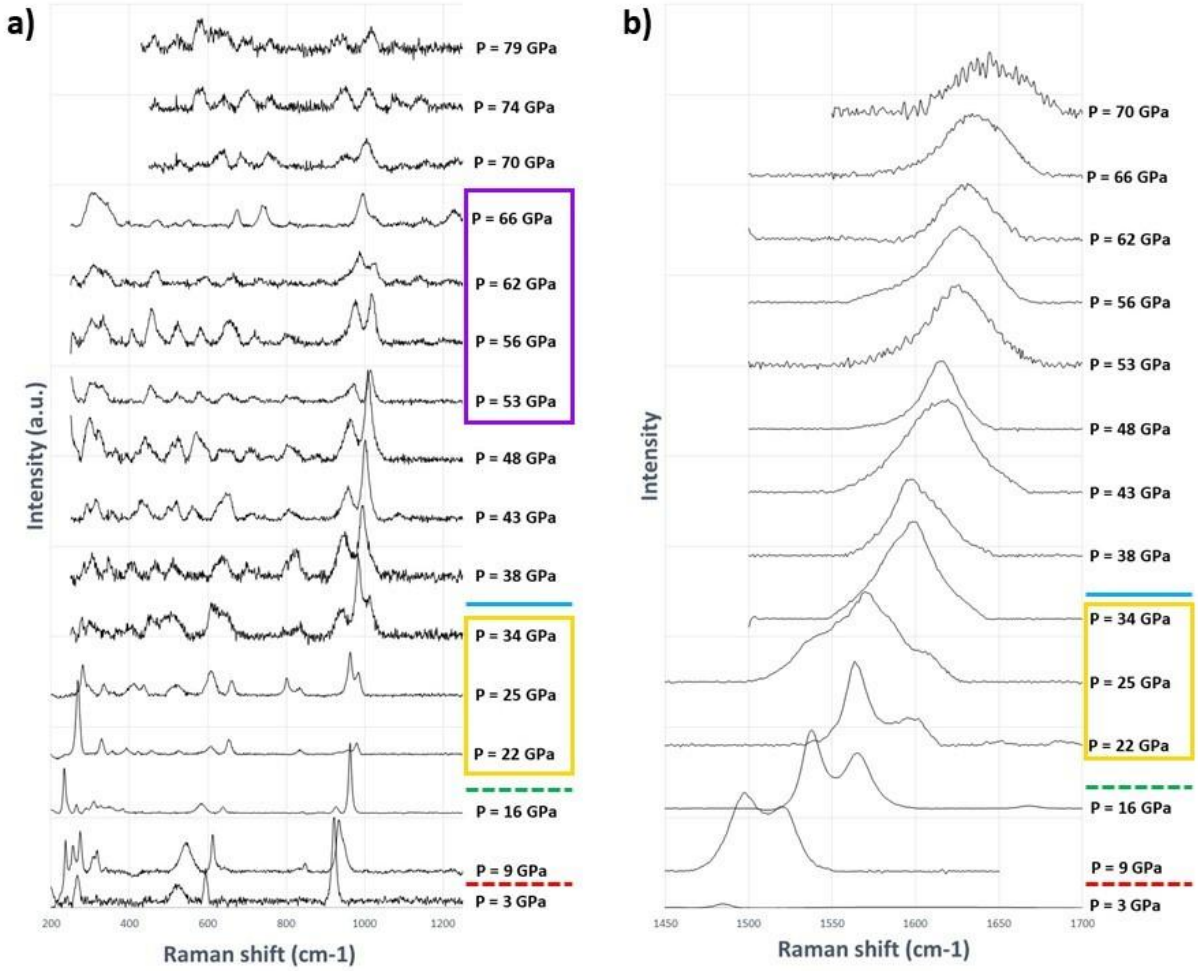

Figure 3.3.2.1: a) Raman spectra in the short range 1 from 3 GPa to 79 GPa and b) Raman spectra in the short range 2 from 3 GPa to 70 GPa. The dashed lines indicate the pressures at which in the integrated patterns (XRD) there are changes due not to phase transitions but to artifacts.

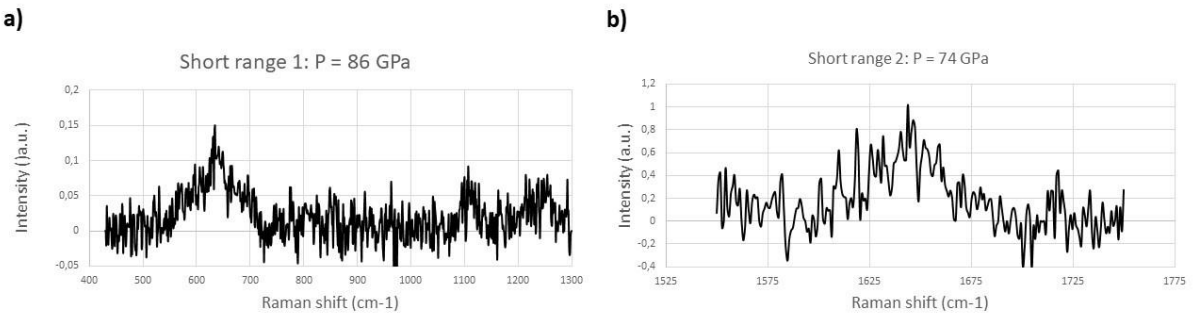

Figure 3.3.2.2: a) Raman spectra between 430 cm^{-1} and 1300 cm^{-1} at P = 86 GPa and b) Raman spectra between 1550 cm^{-1} and 17500 cm^{-1} at P = 74 GPa.

In Figure 3.3.2.1 I identified two regions highlighted in yellow and purple colors, showing changes in the oxalate spectral shape. These regions are identified in accordance with Mössbauer and preliminary XRD data analyses, thus it is conceivable to attribute the variations to pressure-induced changes in the atomic and electronic structure of the oxalate.

At ambient conditions the sample shows five Raman bands in the region from 200 cm^{-1} to 3500 cm^{-1} (Fig. 3.3.1.2). All bands shift to higher frequencies with increasing pressure and at higher pressure new bands start to appear. The shift of Raman bands to higher frequencies at the beginning and as a first approximation is due to the compression of the unit cell and, in a first approximation, the shift follows equation 3.3.2.1 (this formula is based on the theoretical model developed by Buckingham [53]):

$$v = \frac{1}{2\pi}\sqrt{\frac{F_r}{\mu}} \qquad (3.3.2.1)$$

where v is the frequency, F_r is the restoring force and μ is the weighted mass of the molecule or group of atoms. At higher pressure (above 34 GPa) it becomes more difficult to clearly identify the appearance of new bands, disappearance of existing ones and generally their frequency shift and intensity changes because the signal to noise ratio was not optimized during the acquisition of the spectra. The FWHM of the bands is also an important parameter to consider, since it might reflect an increased disorder in the sample structure as well as the presence of pressure gradients, i.e. not uniform pressure distribution on the sample due to deviatoric stress generated in compression.

At ambient pressure one can clearly distinguish five Raman modes, generated by stretching and bending of molecules and atomic pares, as well as entire lattice oscillations, and can distinguished in the spectra from their well defined frequencies (Fig. 3.3.2.3).

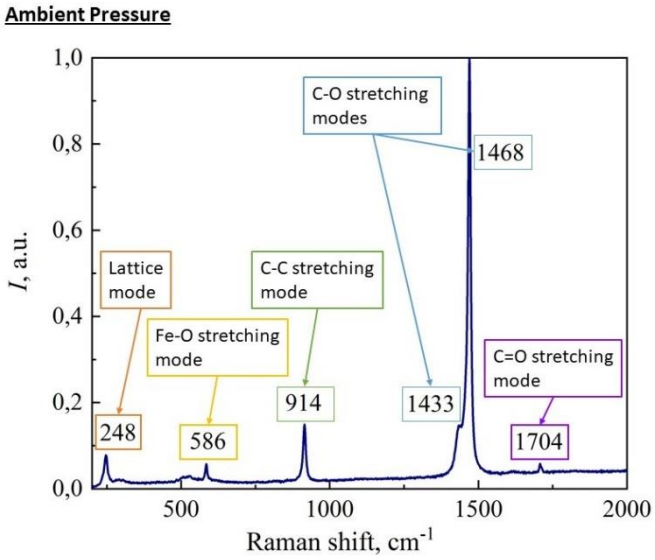

Figure 3.3.2.3: Raman band modes at ambient pressure.

The spectra become more complex at high pressures. At 3 GPa the bands characteristic of Fe-oxalate at ambient conditions are still present but the one at 1704 cm^{-1} disappears and one more band appears in the region of 500-600 cm^{-1}. A further increase in pressure to 9 GPa causes a lot of new vibrational modes to appear at lower wavenumbers (lattice mode), a less intense band appears at ~ 840 cm^{-1} and another one appears at ~1520 cm^{-1} (Fig. 3.3.2.1.a and Fig. 3.3.2.1.b). The spectral evolution seems to indicate the presence of a phase transition in this pressure interval, as normally the appearance of new Raman bands indicate structural changes or at least the formation of new molecular interactions. However, from Müller et al. [1] and our XRD preliminary analysis, it is known that the structure remains the same until ~ 20 GPa, thus we believe the appearance of new bands are caused by inter-molecular interactions due to strong structural compaction and distortion. The unit cell volume shrinks from ~ 517 $Å^3$ at ambient conditions to ~ 369 $Å^3$ at 16.7 GPa [1], showing a sharp collapse of the unit cell which does not come as a surprise considering that the 3D structure of $FeC_2O_4 \times 2\ H_2O$ consists of linear infinite chains of oxalate dianion-Fe-oxalate dianion (oxFeoxFeox) along [010], and neighboring chains in the b-c-plane linked by weak hydrogen bonds between the oxygen atoms of water molecules and oxalate dianions belonging to adjacent chains [1] (Fig. 1.2.2.2 and Fig. 1.2.2.3).

Moreover, most of the structure distortion happens in the first 5 GPa, where the angle β decreases rapidly from 127° to 122° [1], thus it is plausible to imagine that all new observed vibrational modes are caused by new inter-molecular interactions generated by pressure-induced structural compaction and distortion. Also, some of the newly observed bands at lower frequency, could have shifted towards higher wavenumbers

> 200 cm^{-1} due to compression, following Eq. 3.3.2.1, thus it is not to be excluded that some of these bands already existed but were not visible because below the lower detectable limit of the spectrometer. Concerning the higher frequency band (short range 2, Fig. 3.3.2.1.b), one can observe only one tiny peak at 1484 cm^{-1}, which apparently splits into two and gain in intensity after further increasing pressure to 9 GPa. The gain in intensity between 3 and 9 GPa is evident, however it cannot be excluded that the double feature was present already at 3 GPa, but not visible due to the low intensity to it associated.

At higher pressures, the evolution of the spectral shape is not trivial. Between 16 GPa and 22 GPa there is a clear lowering of the peaks' intensity (Fig. 3.3.2.1), which is an evidence of phase transition, in fact above 22 GPa the intensity is recovered. In the same pressure interval and in the region between 1450-1650 cm^{-1} the intensity of the second band at higher wavenumbers (1564 cm^{-1} at 16 GPa and 1594 cm^{-1} at 22 GPa), starts to decrease. At 25 GPa another mode appears (~ 1537 cm^{-1}) and from 34 GPa it seems that only one broad peak characterize the spectrum, even if one could fit it using more than one component, i.e. more than one gaussian curve (Fig. 3.3.2.4 and 3.3.2.5). I could also notice that the asymmetry of the single peak is similar at 34 GPa and 43 GPa but it changes at 38 GPa. At higher pressure the intensity of this band starts to decrease and above 70 GPa it disappears (Fig. 3.3.2.1.b and Fig 3.3.2.2.b).

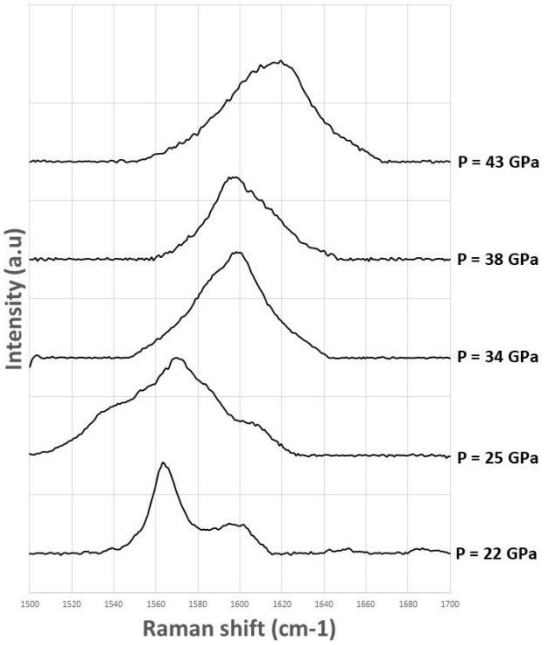

Figure 3.3.2.4: Evolution of Raman bands in short range 2 from 22 GPa to 43 GPa.

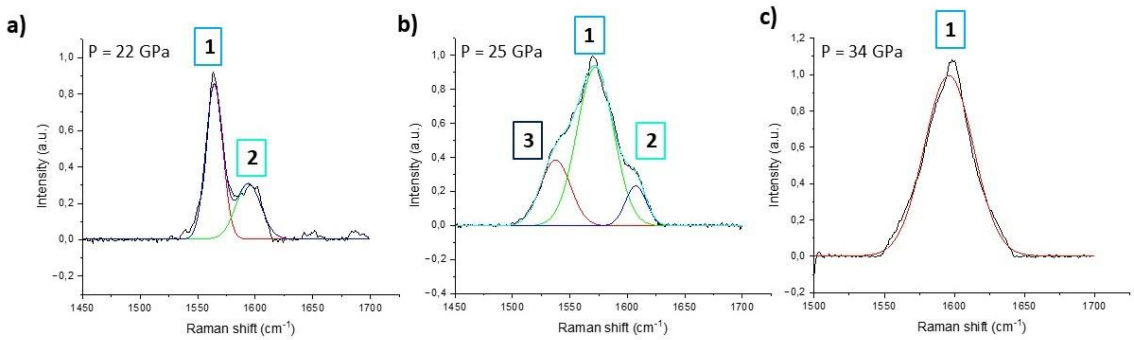

Figure 3.3.2.5: Evolution of Fe-oxalate Raman bands in short range 2 between 22 GPa and 43 GPa (the spectra are fitted with OriginLab): a) two bands (band 1 at 1568 cm^{-1} and band 2 at 1594 cm^{-1}) at 22 GPa, b) three bands (band 1 at 1572 cm^{-1}, band 2 at 1607 cm^{-1} and band 3 at 1537 cm^{-1}) at 25 GPa, c) one band (band 1 at 1596 cm^{-1}) at 34 GPa.

In the mid-frequency range, I noticed that at 22 GPa the intensity of the band identified with number 3 in Figure 3.3.2.6 drastically decreases and a new band identified with number 1 appears. Between 22 GPa and 25 GPa there is an evident change in the intensity of the two bands, 1 and 2, with peak 1 that grows at the expenses of peak two, and peak 3 disappear. However, it cannot be excluded that peak 3 (at 959 cm^{-1} at 22 GPa) is no longer distinguishable from the other two (band 1 at 932 cm^{-1} and band 2 at 979 cm^{-1} at 22 GPa) because it merged to peak 1. Then at 34 GPa another band (band 4) appears in the spectrum at 942 cm^{-1} and at 38 GPa band 2 disappears.

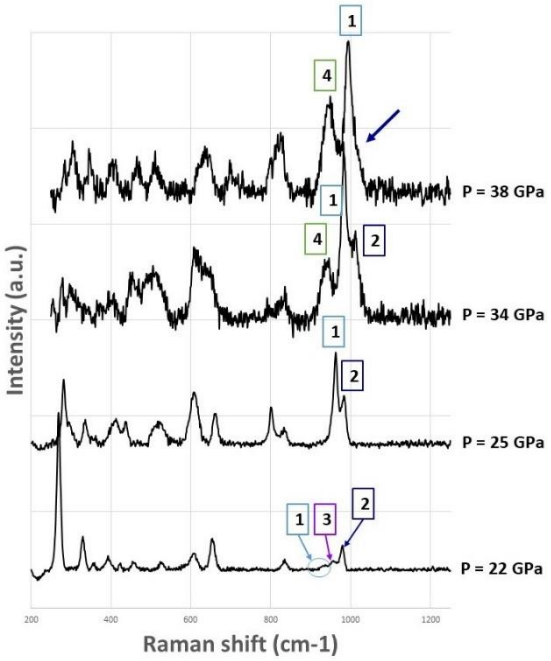

Figure 3.3.2.6: Evolution of Raman bands between 850-1000 cm^{-1} from 22 GPa to 38 GPa.

From 38 GPa to 48 GPa the shape of the spectra remains constant, only the peaks shift to higher wavelengths is observed (Fig. 3.3.2.1.a). At P ~ 53 GPa the reciprocal intensity of band 4 and 1 starts to invert, and complete inversion is reached at ~ 66 GPa, where only a tiny shoulder on the right of band 4 indicate the residual presence of band 1 (highlighted with a light blue arrow in Fig. 3.3.2.7). From 70 GPa to 79 GPa the shape of the spectra remains constant and above 79 GPa the spectra become too noisy and the signal to noise ratio too low to clearly distinguish the presence and evolution of Raman modes in the spectra (Fig. 3.3.2.1 and Fig. 3.3.2.2).

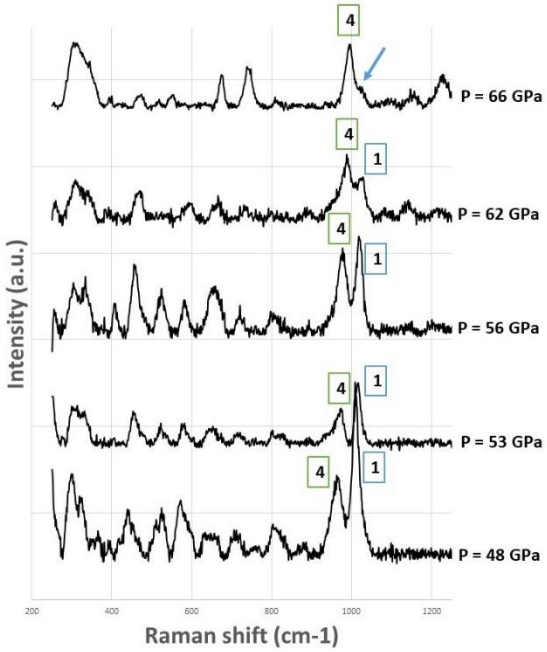

Figure 3.3.2.7: Evolution of Raman bands between 850-1000 cm^{-1} from 48 GPa to 66 GPa.

4. Discussion

Experiments under extreme conditions are an important tool for synthesis of new materials and investigation of physical and chemical properties. Such experiments are of interest not only to physics, chemistry and materials science, but also to geoscience because they provide the opportunity to probe the properties of geophysically relevant materials at conditions of the deep Earth's interior. This work is focused on the high-pressure high-temperature behaviour of synthetic iron oxalate dihydrate and in this chapter I will discuss the results of the experimental investigation presented in Chapter 3. I will combine the SMS, XRD and Raman data in order to have a complete analysis of the evolution of the sample under compression and after laser heating. In particularly, I will present some effects the iron oxalate suffers: i) the Goldanskii-Karyagin effect, ii) the spin transition and iii) the Jahn-Teller effect. Moreover, I will illustrate the structural and phase transition the sample undergoes under compression and the new product synthetized after laser heating.

4.1 Goldanskii-Karyagin effect applied to the study of Fe-oxalate at extreme conditions

In a Mössbauer spectrum, the positions of peaks and the hyperfine parameters of the lines are of primary interest. The angular dependence of the hyperfine interactions can also be significant. There are two main contributions influencing the relative line intensities of the peaks: i) the lattice vibrational anisotropy (the Goldanskii-Karyagin effect) and ii) the orientations of the spins and of the axes of the electric field gradient (EFG).

In this work, the fitting of the main Mössbauer spectra was performed by keeping the A12 parameter, which expressed the symmetry or asymmetry of the peaks in a doublet, to 0.5 for the X site (symmetric) and allowed to vary only the Y site after the emergence of the Y site at around 52 GPa. I followed this approach because I suppose that the X site goes from octahedral to dodecahedral coordination while I suppose that the Y site is in octahedral coordination. Moreover, I attribute the origin of the asymmetry of the doublet to the Goldanskii-Karyagin effect that it is known not to affect cubic/dodecahedral sites.

Let us now explain the origin of the asymmetry of the doublets and so the Goldanskii-Karyagin effect [54]. The angular dependence of the quadrupole interaction is reflected in the relative line intensities, I' = (±1/2 → ±3/2) and I''= (±1/2 → ±1/2), corresponding to the transitions $\Delta m = \pm 1$ and 0, respectively. In the thin-absorber approximation the intensity ratio is:

$$R_q = \frac{I'}{I''} = \frac{1+\cos^2\theta_q}{\frac{2}{3}+\sin^2\theta_q} \quad (4.1.1)$$

where θ_q is the angle between the direction of the γ-ray propagation and the principal axis of the EFG, $\hat{n}$. Here we assume that the asymmetry parameter η = 0. The value R_q= 1 is obtained for an ideal powder absorber in which the crystals are randomly orientated. However, if the recoil-free fraction *f* depends on the crystallographic and magnetic directions, the relative line intensities R_q of the hyperfine pattern will reflect this lattice vibrational anisotropy. Thus, the doublet will show asymmetric or abnormal peak intensities.

In our case the experiments were carried out using polarized synchrotron radiation on Fe-oxalate monoclinic single crystals, with ferrous iron (Fe^{2+}) "sitting" in octahedral coordination with oxygen in the X site and represented by a doublet component in the Mössbauer spectrum. This doublet, originally asymmetric due to lattice orientation owed by its single crystalline form, inverts the asymmetry of the peaks during compression. If at increasing pressures the intensity of the peaks reduces or reverts, i.e. the most intense peak becomes less intense and the less intense becomes more intense, it means that the sample structure is changing or that the single crystal is becoming progressively a powder. Indeed, at ID18 at ESRF the direction of the magnetic field is fixed. Therefore, if the intensity of the two peaks reverses, it means that the gradient of the magnetic field within the sample has changed. In order to better visualized how the asymmetry of the doublet of the X site change in the range of pressure between 5.5 GPa and 44 GPa (before the appearance of the second doublet of Y site), I did the fitting of the Mössbauer spectra using two singlet for every peak of the doublet (Fig. 4.1.1) and I plot the evolution of the relative intensity and of the FWHM of the two singlets with pressure (Fig. 4.1.2).

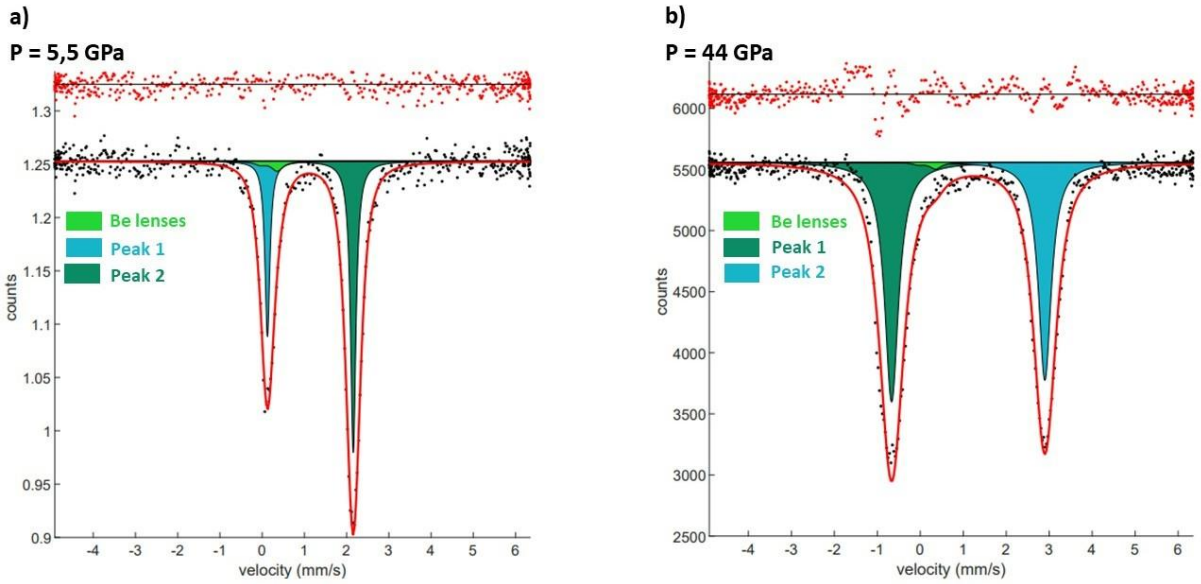

Figure 4.1.1: Mössbauer spectra fitted using MossA software package: a) DAC 2 at 5.5 GPa and b) DAC 2 at 44 GPa. The purpose of using two singlets instead of a doublet is to perform an in depth analysis and better understand the evolution of the peaks'

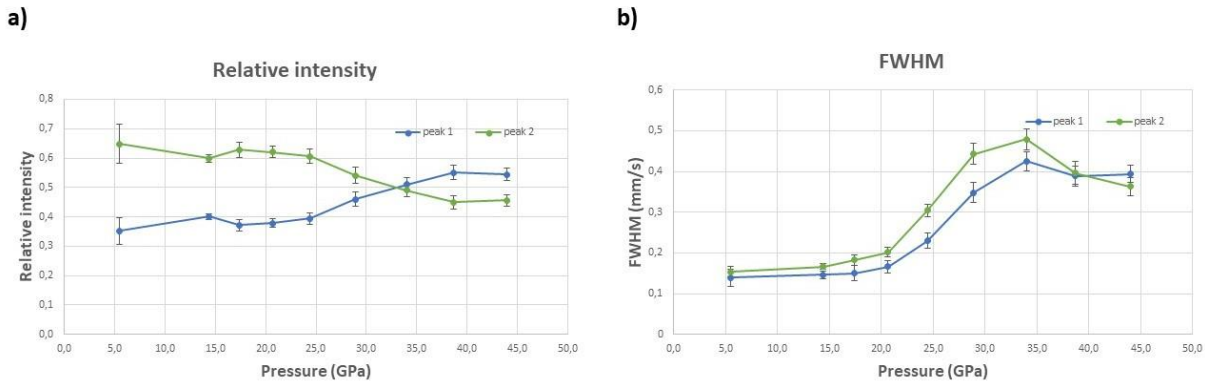

Figure 4.1.2: a) Evolution of relative intensity of the two peaks of the doublet of X site from 5.5 GPa to 44 GPa and b) evolution of FWHM of the two peaks of the doublet of X site from 5.5 GPa to 44 GPa.

From Figure 4.1.2.a it is clear the inversion of symmetry of the doublet and we can see that it happens at ~ 34 GPa. This result is in line with the hypothesis of a sluggish phase transition observed between ~ 22 and 38 GPa, where Fe^{2+} in the X site increases its coordination number from 6 → 8. Because the transition happens in a ~ 16 GPa interval, it is possible that the asymmetry progressively decreases while the X site becomes dodecahedral. Further distortion of the site due to compaction of the new structure might cause the little asymmetry inversion observed above 34 GPa. This result is corroborated by the constant increase in QS value, which stabilize around 38 GPa. An

in depth analysis of the XRD data is necessary to confirm our interpretation and is currently ongoing.

4.2 Spin transition

Iron is the most abundant transition metal within the Earth and features 3d electronic shells which can be partially filled, allowing for more complex structures than other major rock-forming elements. The ability of iron to exist in multiple valence states, Fe^{0}, Fe^{2+}, Fe^{3+}, Fe^{4+} and different electronic configurations, high-spin, low-spin and intermediate-spin, is the key to the formation of a wide variety of iron-containing materials that are of interest in many disciplines, among them Earth sciences, Material sciences, Chemistry and Physics. Related to the Earth, iron exhibits two main valence states in lower mantle materials: ferrous iron (Fe^{2+}), with six 3d electrons, and ferric iron (Fe^{3+}) with five 3d electrons. The length of iron ionic radii, which depend on the valence state and electronic configurations, i.e. high-spin and low-spin states, can differ up to ~ 22 % for Fe^{2+} and ~ 52 % for Fe^{3+}, depending on the coordination environment [55, 56]. For instance, all six 3d electrons of low-spin Fe^{2+} are paired in the outer shell orbitals, whereas high-spin Fe^{2+} has four unpaired electrons, thus the resulting high differences in ionic radii. For the above presented reasons, the spin transition of iron in lower mantle minerals affect significantly their physical (e.g., density and bulk modulus), transport (e.g., electrical conductivity and radiative heat transfer), and chemical (e.g., element partitioning) properties.

Let us now introduce the phenomenon of the spin transition in iron bearing compounds. Fe^{2+} has six electrons in the more external 3d orbitals. The d-orbitals have not the same energy. Indeed, the metal's five degenerate d-orbitals experience specific energy changes when surrounded by certain symmetries of ligands, which act as point charges. To better understand the process that removes this orbital degeneracy we have to combine the molecular orbital theory with the crystal field theory (CFT). This resulting theory is known as ligand field theory (LFT) and it allows for a complete understanding of the process of chemical bonding, electronic orbital structures, and other characteristics of coordination complexes. Consider now our case in which we have FeO_6 octahedra in which six ligands (oxygen), each positioned along a Cartesian axis, form an octahedral shape around a metal ion (iron). Based on CFT, the d-orbitals of the metal Fe^{2+} ion split into two sets with an energy difference Δc (the crystal-field octahedral splitting parameter). The d_{z^2} and $d_{x^2-y^2}$ orbitals lie along Cartesian axes and will experience an increase in energy due to repulsion caused by their proximity to the oxygen ligands. On the other hand, the d_{xy}, d_{xz}, and d_{yz} orbitals do not lie directly along any Cartesian axes but lie in planes between the ligands and therefore are lower in energy respect the d_{z^2} and $d_{x^2-y^2}$. For this reason, the d_{xy}, d_{xz}, and d_{yz} are energetically

stabilized. The three lower energy orbitals are collectively referred to as t_{2g} and the two higher-energy orbitals as e_g (Fig. 4.2.1).

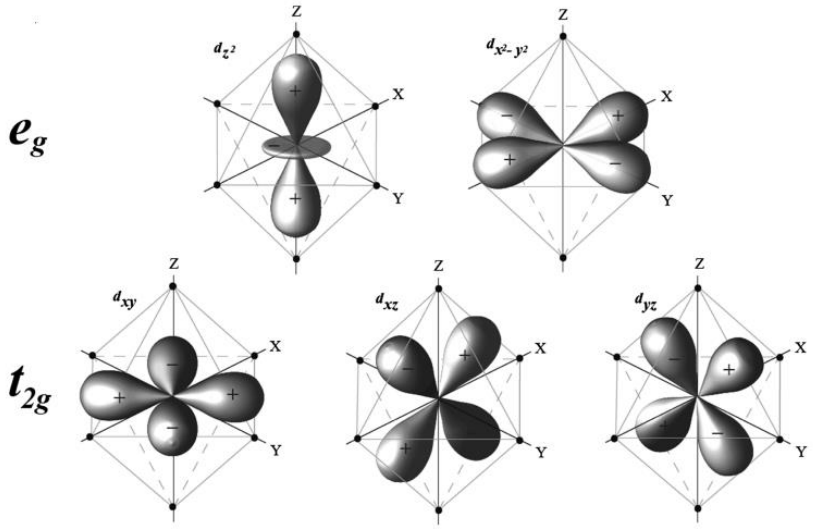

Figure 4.2.1: d-orbital configurations in an octahedral site.

It must be pointed out that the situation changes if Fe is in a dodecahedral site (or in any other coordination environment) instead of an octahedral one because the orbital splitting energies are directly related to the specific molecular coordination geometry of the complex. Thus, a dodecahedral ligand arrangement causes the t_{2g} orbitals to be higher in energy than the e_g orbitals. The occupation of the 3d orbitals depends on the surrounding environment of the iron ion and it is influenced by different factors such as bond length, crystallographic site, pressure, and temperature. Based on the crystal field theory, the spin transition of iron in Fe-bearing compounds exposed to high pressures is volume driven and results primarily from the competition between two quantities: the crystal-field splitting parameter (Δc) and the exchange splitting energy (Λ). For Fe^{2+} in an octahedral site, the 3d electrons of iron can occupy different degenerate sets of the 3d orbitals, namely the relatively lower energy triplet t_{2g} orbitals and the relatively high energy doublet e_g orbitals. Under ambient conditions, it is energetically favorable for the 3d electrons to occupy different orbitals with the same electronic spin, following Hund's rule. In this situation the t_{2g} and e_g orbitals are separated by the crystal-field splitting energy, which is lower than the electronic spin-pairing energy. Therefore, the Fe^{2+} is in the high-spin state with four electrons in the t_{2g} orbitals and two unpaired electrons in the e_g orbitals (the total spin quantum number (S) is equal to 2 because each electron has S = 1/2 (Fig. 4.2.2). However, changes in pressure and temperature influence the crystal-field splitting energy with respect to the spin-pairing energy. Under high pressures, the crystal-field splitting energy increases with respect to the spin-pairing energy leading to the pairing of the 3d

electrons of the opposite spin. In this situation, Fe^{2+} is in the low-spin state with all six 3d electrons paired in the t_{2g} orbitals (S = 0) (Fig. 4.2.2).

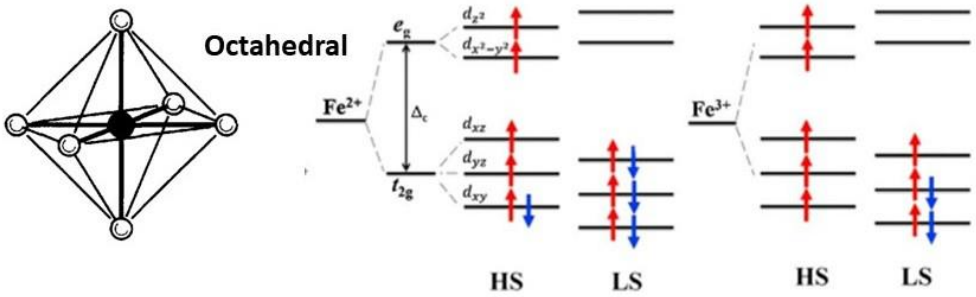

Figure 4.2.2: HS and LS configuration for Fe in octahedral coordination.

The electronic density distribution of the 3d shell of HS Fe^{2+} ions in octahedral coordination is non-spherical with S = 2 while Fe^{2+} ions in the low-spin state are more spherically symmetric with S = 0. This simplified crystal-field picture for the pressure induced spin transition becomes more complex through crystallographic site distortion and electronic band overlap where occupancy degeneracy is lifted, complicating our understanding of the spin transition in these systems.

In our case, it is not trivial to understand what happened to our sample only from Mössbauer spectroscopy. At P > 50 GPa a second doublet starts to emerge from the spectra and grows until P ~ 70 GPa (Fig. 3.1.2.1.1), where the co-existence of the two components appears to reach a steady-state (Table 3.1.2.1). This behavior can be visualized by the plot of the relative intensity of the two sites (Fig. 4.2.3) and could be explained by three different options:

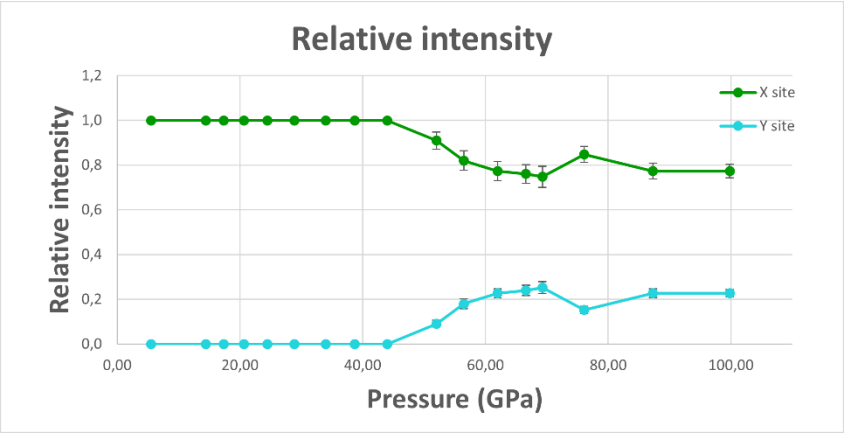

Figure 4.2.3: Evolution with pressure of relative intensity of X site and Y site.

(i) The first explanation is the transition to a new structure characterized by two distinct iron sites with different coordination numbers and hypothetically different

spin states. Indeed, at the beginning of the transition (at 52 GPa when there is the appearance of the second doublet) the intensity of Y site increases with pressure, meaning that more and more atoms go into that configuration. However, the doublet of the X site does not disappear completely, meaning that at the end both sites are present in the sample. This model is supported by the hyperfine parameters of the new doublet, CS of 0.44 mm/s and QS of 1.118 mm/s at 52 GPa, which could well represent LS-Fe^{2+} in a distorted octahedral environment. Thus the new structure would be characterized by two distinct iron sites, dodecahedral and octahedral, in HS and LS states respectively.

(ii) Another interpretation is the pressure induced oxidation of Fe^{2+} to Fe^{3+}, caused by the reduction of carbon in the oxalate molecule with consequent formation of one or more new phases. However, this option implies a redox reaction, which are normally caused by the application of high temperatures to the system. Heating to high T makes possible to overcome the activation energy necessary to break the bond between an electron and its atom or molecule allowing the former to move to a new ion or ionic complex. Since temperature is the average kinetic energy of the particles in the system, the higher the temperature, the higher the energy, and the easier the electron transfer. Even if pressure-induced redox reaction has been reported in the literature [57, 58], this is more unusual for Fe bearing compounds [59] and overall not common.

(iii) The last option is the attribution of the rise of the second doublet purely to the spin pairing of iron 3d electrons, preserving the original structure. However, in the case of spin pairing, one would expect a complete conversion, thus, the progressive disappearance of the first doublet, representing iron in a high-spin state, to the advantage of the low-spin doublet, which does not happen in our system (Fig. 4.2.3). As explained above, when there is a spin crossover, before the transition the original site is 100% in HS whereas the new site does not exist yet, thus 0% of the iron atoms are in LS state. Then, when the transition starts, the LS site starts to increase at the expenses of the HS site and at the end only the LS site is present in the spectra (the spin transition is completed). This is not our case. Indeed, we start with 100% of X site (Fe in HS) and 0% of Y site (Fe in LS), then the X site starts to become less intense but at ~ 70 GPa the intensities of the two sites stabilize showing the co-existence of both environments until the highest reached pressure (100 GPa) without any obvious variation in the components' intensities (Fig. 4.2.3). Despite some fluctuations in the relative intensities, it seems that from ~ 60 GPa 80% and 20% of iron atoms are in X and Y sites respectively. One explanation is the formation of metastable intermediate spin Fe^{2+} local environments (instead of LS) as already reported for bridgmanite at extreme pressures [60] where the presence of a new doublet with high QS values was observed, without the complete disappearance of the original component or any observed structural change. In this case, only one of the three electrons occupying the

t_{2g} orbitals goes into the lower energies e_g orbitals, thus creating an intermediate spin state. Note that the 3d degeneracy in dodecahedral and octahedral environment is reversed. The existence of a quadrupole splitting in the new doublet is indicative for a certain degree of EFG, which could be caused in this case by the partial electron pairing in the IS state as well as by the site distortion.

The spin crossover arises from a condition in which the thermal energy at high P-T is sufficient to overcome the energy difference between the high-spin and low-spin states. The fraction of the low-spin state (n_{LS}) at a given P-T condition is described by:

$$n_{LS} = \frac{1}{1+\exp\left(\Delta G(P,T)*/T\right)} \quad (4.2.1)$$

where $\Delta G(P,T)^*$ is the difference of the Gibbs free energy between the low-spin and high-spin states [61]. So, the spin crossover can be expected to occur in broader pressure range and depending on pressure can be completed or not. Nevertheless, I exclude the possibility of a partial conversion from HS to LS while maintaining the same structure, because even if it has been observed that the spin crossover can happen in broad pressure ranges, i.e. [55], the conversion is progressive and do not stop, which is instead what we see in our results.

Generally speaking, options (i) and (iii) are supported by the change hyperfine parameters. Indeed, Fe^{2+} in LS configuration has no unpaired electrons with nearly spherical charge distribution and this means that the EFG is essentially zero because all 3d energy levels are nearly equally occupied. Spin pairing changes abruptly the degree to which s electron density at the Fe nuclei is shielded by 3d electrons; hence the CS of the Y site drops considerably to 0.440(19) mm/s at 52 GPa. The decrease in CS at the transition is higher than the value observed for ferropericlase (~ 0.17 mm/s, [62]), but lower than for ironorganic complexes (~ 0.5 mm/s, [63]) at ambient or low (< 5 GPa) pressure. The value of the QS of the Y site is also in agreement with the result of a spin transition. Indeed, in our case the QS value of Y site (QS = 1.118(37) mm/s – 1.192(21) mm/s between 52 GPa and 100 GPa) has lower values than the QS of X site (QS = 3.531(11) mm/s – 3.260(11) mm/s between 52 GPa and 100 GPa). This confirms that site Y is Fe^{2+} in IS or LS states because lower values of QS indicate more symmetry around the Fe ion. Option (ii) however cannot be completely ruled out without further investigations since the hyperfine parameters of the new doublet might also match those of octahedrally coordinated HS-Fe^{3+}, the possible product of a redox reaction.

Raman spectroscopy also provides evidence of the spin transition. Figure 4.2.4 shows the evolution of Raman bands representing C-C symmetric stretching modes and O-C-O bending modes between 850-1000 cm^{-1} from 48 GPa to 66 GPa.

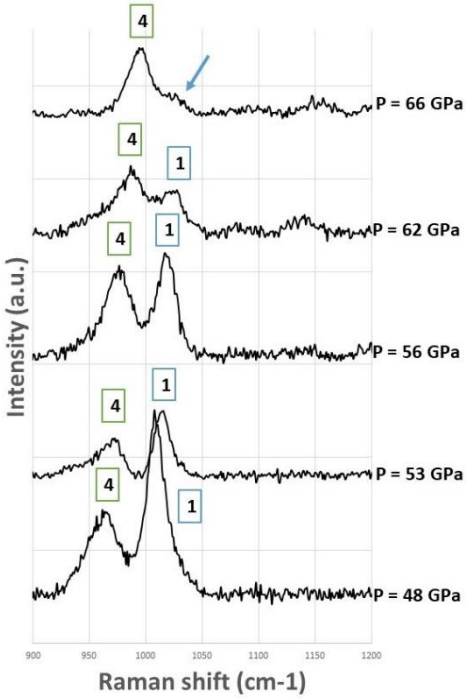

Figure 4.2.4: Evolution of Raman bands between 850-1000 cm^{-1} from 48 GPa to 66 GPa.

I assign band 4 (identified in Fig. 4.2.4) to Fe^{+2} in low spin configuration and band 1 (identified in Fig. 4.2.4) to Fe^{+2} in high spin configuration. When Fe^{+2} is in HS the electronic cloud is wider than that of Fe^{+2} in LS configuration. In LS the electronic cloud is more concentrated because the electrons are paired in same levels, the t_{2g} orbital, while in HS the electrons are unpaired in both e_g and t_{2g} orbitals. Therefore, Fe^{+2} in LS has a smaller radius respect Fe^{+2} in HS. Since the strength of the bond between Fe and O remains the same, we expect the volume of the FeOx polyhedron to shrink, i.e. the oxygens get closer to the iron atom resulting in longer C–O bonds. This causes a weakening of C-O bond and so the shift/growth of the peak to lower frequencies. Note that this model assumes the presence of oxy-carbon complexes such as a high pressure form of oxalate ions, intercalated between FeOx polyhedral (where x = 8 +) .The fact that at the beginning the band 4 (LS) is less intense and then becomes progressively more intense at the expense of band 1 (HS), which eventually disappears, may be indicative of the fact that due to the compression the sample is passing from HS to LS (or IS). It's a slow transition since the disappearance of the band 1 does not occur in a few GPa but in a larger range. Similar behavior on the evolution of Raman band mode is seen in carbonates [64].

In conclusion, our latest interpretation of the Mössbauer data is that the original doublet, which represents the X site, is due to Fe^{2+} in HS configuration and in octahedral coordination (CS = 1.14 mm/s and QS = 2.03 mm/s at 5.5 GPa). At pressures between 5.5 and 22 GPa, the site distortion increases due to the collapse of the oxalate

unit cell, while above 22 GPa until 38 GPa the X sites progressively turns from octahedral to dodecahedral in a sluggish structural transition (CS = 1.11 mm/s and QS = 3.57 mm/s at 44 GPa). At 52 GPa another doublet starts to appear which indicates either (i) a partial spin transition of Fe^{2+} in dodecahedral coordination to IS or LS states, or (ii) the formation of a new site, thus a new structure, where Fe^{2+} is in LS state and octahedrally coordination to 6 oxygen atoms.

4.3 Jahn Teller effect

The Jahn–Teller effect is the intrinsic instability of an electronically degenerate complex against distortions that remove the degeneracy. This happens because we cannot have an orbital degeneracy in the ground state of any quantum system. For this reason, there will be the lifting of orbital degeneracy with the consequential local symmetry breaking and deformation of crystal that will lower the symmetry and will give rise to a more favorable energy state. In our sample there is Fe^{+2} at the beginning in octahedral coordination and then in dodecahedral coordination and it can be energetically favorable for an octahedron to spontaneously distort because the energy cost of increased elastic energy is balanced by a resultant electronic energy saving due to the distortion. To describe the effect, at least at the phenomenological level, we will quantify the distortion of the system with the parameter Q, which denotes the distance of distortion along an appropriate normal mode coordinate. This gives rise to an energy cost which is quadratic in Q and can be written as:

$$E(Q) = \frac{1}{2} M w^2 Q^2 \tag{4.3.1}$$

where M and w are respectively the mass of the anion and the angular frequency corresponding to the particular normal mode. This relation is plotted in Figure 4.3.1.a and from this figure is clear that when Q = 0 we have the minimum distortion energy (no distortion). The distortion will raise the energy of certain orbitals and will lower the energy of others. In the cases of partially filled orbitals this effect can be important since the system can have a net reduction in total energy. The electronic energy dependence on Q is rather complicated, but one can write it as a Taylor series in Q and can keep only the term linear in Q assuming that the distortion is small. Hence, let us suppose that the energy of a given orbital has a term either AQ or -AQ corresponding to a raising or a lowering of the electronic energy, where A is a positive constant. Then the total energy E(Q) is given by the sum of the electronic energy and the elastic energy:

$$E(Q) = \pm AQ + \frac{1}{2} M w^2 Q^2 \tag{4.3.2}$$

where the two possible choices of the sign of the AQ term give rise to two separate curves which are plotted in Figure 4.3.1.b.

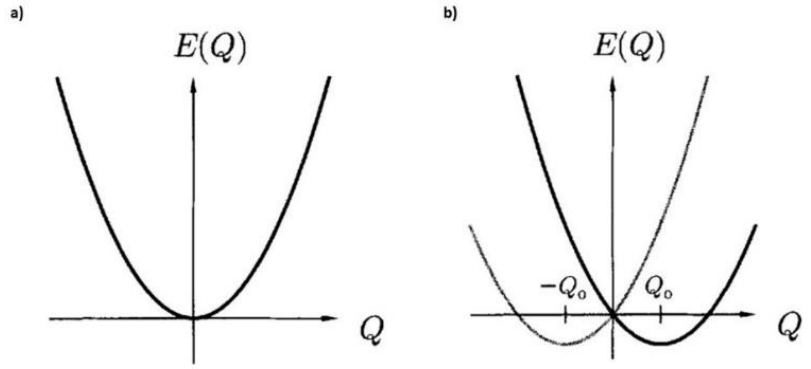

Figure 4.3.1: a) The energy of an octahedral complex as a function of the distortion Q according to eq. 4.5.1. and b) the energy of an octahedral complex as a function of the distortion Q according to eq 4.5.2.

The minimum energy for that orbital is obtained by equating to zero the first derivative respect the Q value of the energy:

$$E_{min} = -\frac{A^2}{Mw^2} \tag{4.3.3}$$

This term is negative and so the system can make a net energy saving by spontaneously distorting itself.

In the Raman spectra (Fig.4.3.2), I see that Fe^{2+}–O stretching bands (highlighted in red circles) are split and broadened in agreement with other studies [65].

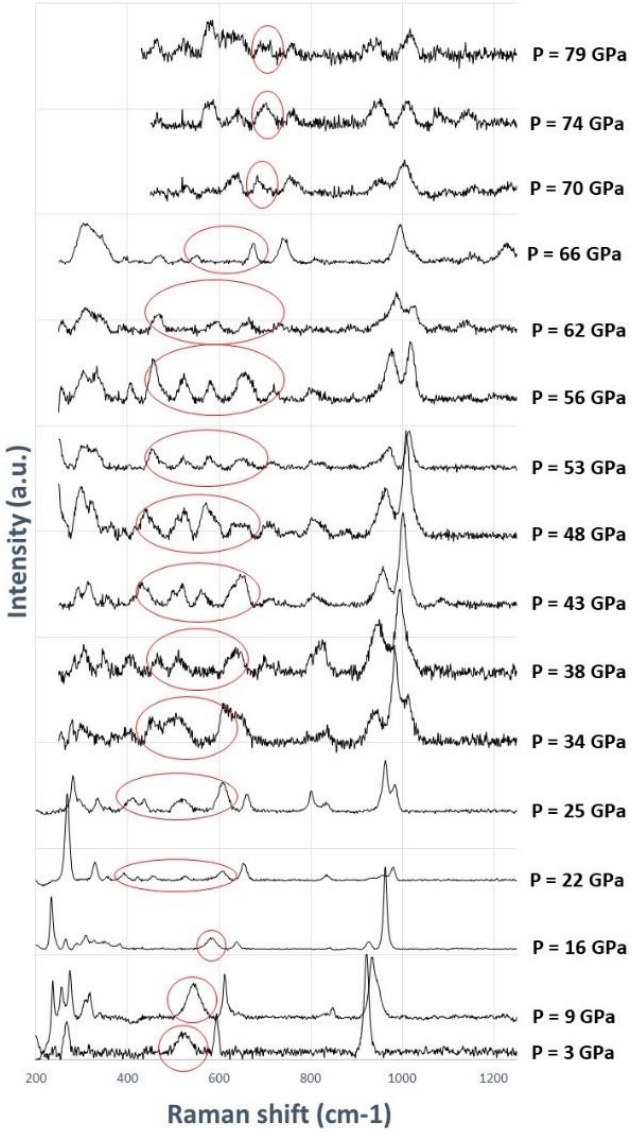

Figure 4.3.2: Raman spectra in the short range 1 from 3 GPa to 79 GPa. I highlighted with red circle the region in which there are Fe^{2+}–O stretching bands.

Both the broadening and lowering the intensity of the Fe^{2+}–O band may arise from the Jahn-Teller effect of Fe^{2+} ion. This effect is well known in octahedral complexes of transition metal and it very common in Fe^{+2} and in Mn^{+3} complexes. However, tetrahedral and dodecahedral sites can also display Jahn-Teller distortion, proven that degeneracy is present within the d orbitals. In previous studies [65] it was found that the Fe^{2+}–O stretching band in humboldtine (Fe complexes) is significantly broader and less intense than the Mn^{2+}–O stretching band in lindbergite (Mn-oxalate). The Jahn-Teller distortion therefore usually acts by causing an axial elongation of the metal-ligand bond along the z-axis and the compression of the four bonds lying on the plane.

It would also be possible the inverse alternative, that is the lengthening of the bonds on the plane and the compression of the axial ones, but considering that in this way four bonds weaken (against the two of the previous distortion) it is easily explained why the occurrence of the previous type of distortion prevails. In humboldtine the second type of distortion occurs. In humboldtine the d_{xy} orbitals point to the regions where there is no ligand. However, small repulsion due to the narrow bite-angles may occur between the orbitals and ligands (oxygen atoms belonging to oxalate anions). Thus, the repulsion induced by the narrow bite-angles causes the $Fe^{2+}O_6$ polyhedra to be horizontally elongated. The Mn^{2+}–O stretching band in lindbergite are less broad than the Fe^{2+}–O stretching band in humboldtine because the $Mn^{2+}O_6$ polyhedra are less distorted than $Fe^{2+}O_6$ polyhedra and the bite-angles in lindbergite are narrower than those in humboldtine. These differences can be explained both by the fact that high spin Mn^{2+} ion causes no Jahn Teller effect and by the interpretation that the octahedral distortion in humboldtine is caused by asymmetric t_{2g} configuration of electrons in which the energy level of d_{xy} become more stable. The consequence of the Jahn Taller effect is that the coordination environment of Fe^{2+} is a distorted octahedron where the two metal-water bonds (Fe–O3) are shorter than the other four metal-oxalate bonds (Fe–O1 and Fe–O2) (Fig. 4.3.3).

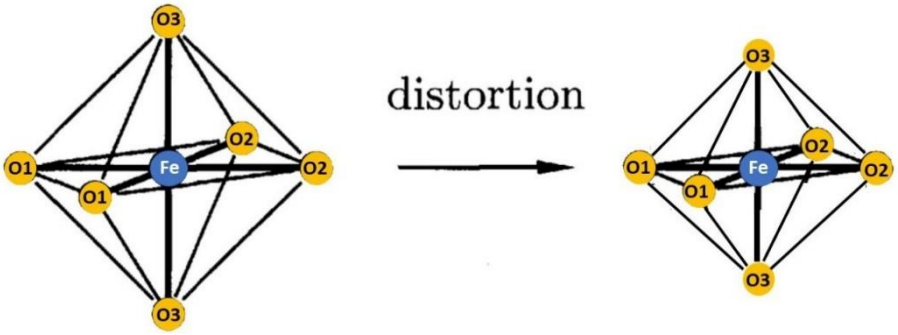

Figure 4.3.3: The Jahn-Teller effect for Fe^{+2}.

4.4 Synchrotron Mössbauer Spectroscopy dataset comparison

I analyzed and compared the data collected during the experiment HC-5141 with another dataset. The latter dataset was previously collected by Cerantola et al. at ID18 at ESRF. During this previous experiment a single crystal of iron oxalate dihydrate with different dimensions was analyzed. The spectra were collected in the range of pressure between 7.5 GPa and 58 GPa at pressure steps of about 6/8 GPa. The fitting of this dataset was performed in the same way of the current dataset. The results obtained in the former experiment (Cerantola et al.) display very similar trends and

are overall in agreement with those measured in this study. Figure 4.4.1 shows the comparison of the evolution of the CS and QS of the X and Y sites of both datasets.

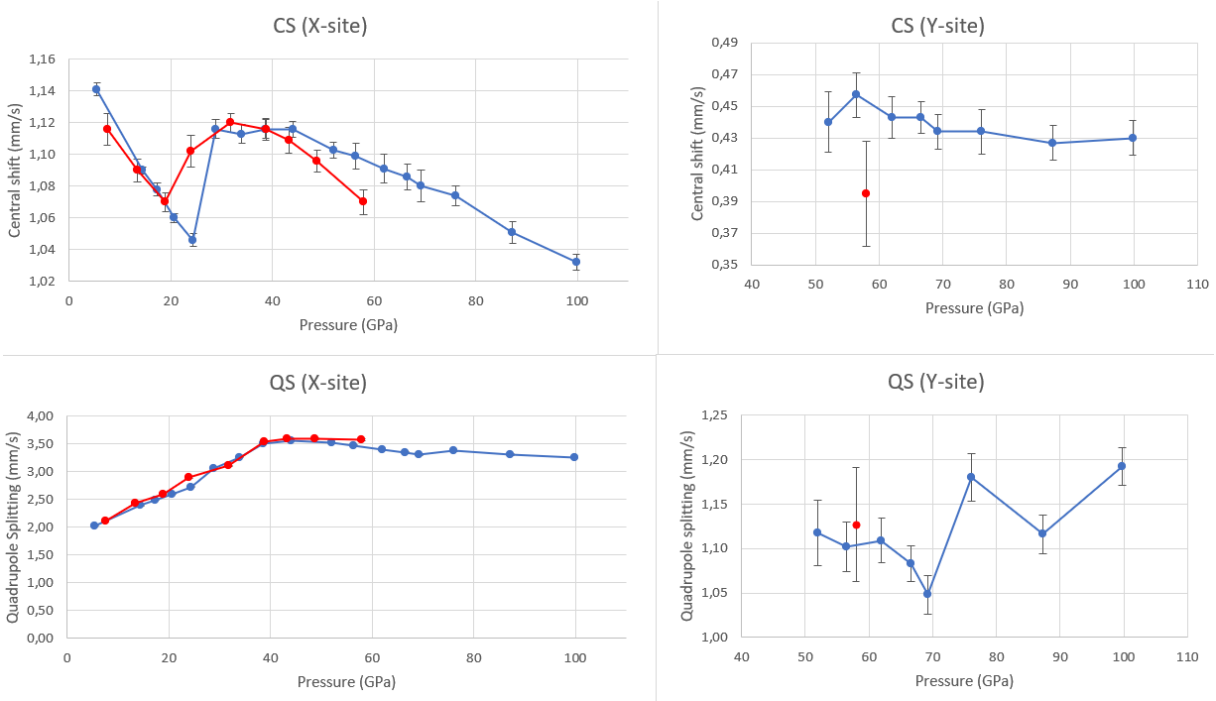

Figure 4.4.1: CS and QS of X site and Y site. The blue line represents the dataset collected during experiment HC-5141 whereas the red line is for previous dataset collected by Cerantola et al. (In QS of X site, the error bars are smaller than the identifying data points).

The results from Cerantola et al. show some differences in the CS position for both X and Y doublets with respect to the data collected in this study. For the X site the difference is not higher than 5%, and within error it is not larger than ~ 2%. One particular however should be noted, the first structural transition seems to start earlier, i.e. ~ 19 GPa vs ~ 24 GPa, probably because of the dimensions of the sample used. Indeed, it is known that the sample is very soft and deformable, the bulk modulus of monoclinic Fe-oxalate is 12.4(3) GPa, thus larger crystals experience higher deformability and strain during uniaxial compression which ultimately can affect the pressure at which the transition starts and overall its range of development. From Figure 4.4.1, one can notice that in the red dataset the CS of the X site decrease at slight slower rate between 7.5 GPa and 19 GPa. Then, between ~ 19 GPa and ~ 32 GPa the CS increases to much higher values as we also observed in this study, however the change is smoother and less sharp than in our dataset (blue line). This evidences that in the preliminary study from Cerantola et al. the phase transition, already discussed for the first dataset (blue line) in Chapter 3.1.2.1, occurs slowlier. After the jump, the CS of second dataset starts immediately to decrease (without no clear plateau) at a higher

rate with respect to the blue dataset. Instead, the trend of the QS of X site of both datasets follows a very similar behavior, which indicate a comparable evolution in terms of coordination number and deformation of the Fe-containing polyhedra as described in Chapter 3.1.2.1. As for the CS and QS of the Y site in the red dataset, only one data point is available for comparison with the results obtained in this study. It shows that the CS and QS are at slightly lower and higher values with respect to our datasets, but overall they are consistent within errors. From the comparison of the two datasets, I found consistency in the data. The tiny differences in hyperfine parameters are probably caused the different sample used, which even if had the same chemical composition and structure, both were selected from the same crystals batch, different crystals quality and dimensions could have caused the observed discrepancies.

4.5 Structural/phase transitions and evolution of sample under compression

In this work, we investigate the behaviour of iron oxalate dihydrate under compression. Our main goal is to understand the stability and behavior of this compound at extreme conditions, which are of interest in Earth sciences, to determine the composition of main and accessory mantle minerals, and in Material sciences and Condensed matter Physics, which look at the phenomena behind phase transitions as well as their physico-chemical properties. In order to analyze the evolution of the sample under compression, I plotted the evolution of hyperfine parameters at the increase of pressure. In particular, based on the fitting of the Mössbauer spectra presented in Chapter 3.1.2.1, the CS and QS are plotted at the increase of pressure for X site in Figure 4.5.1. I identified four different regions representing changes in the atomic and electronic structures, highlighted in Figure 4.5.1 using straight lines of different colors. These regions are identified in accordance with XRD data (Fig. 4.5.5). It is useful to see these trend because the CS and QS are sensitive parameters to the variation in pressure.

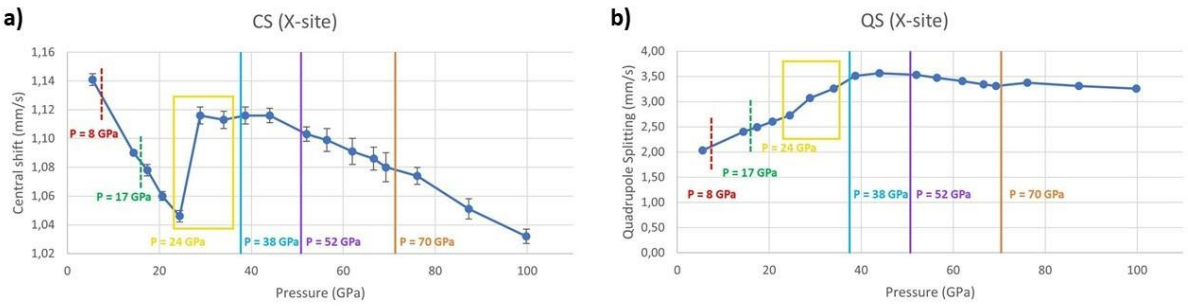

Figure 4.5.1: a) Evolution with pressure of CS of X site and b) evolution with pressure of QS of Y site. (In QS of X site, the error bars are smaller than points identifying data).

Generally speaking, there is a decrease in the CS with increasing pressure, which correspond to an increase of electron density at the iron nucleus, while the QS usually increase with pressure [66] due to a distortion of the local environment around the Fe nuclei. A quantitative interpretation depends on the knowledge of changes in local symmetry and spin-orbital coupling factors, as well as local compressibility. In particular, the central shift is sensitive to the s-electron density at the nucleus, while the quadrupole splitting measures the electric field gradient caused by a non-symmetrical charge distribution around the nucleus (see Chapter 2.2.1).

Ferrous iron electrons configuration is $1s^2 2s^2 2p^6 3s^2 3p^6 4s^2 3d^6$. Let us know consider the electron density term. The 1s and 2s orbitals contribute strongly to the electron density at the nucleus but they are completely insensitive to the chemical state and surroundings of the iron. The 3s electrons are relatively insensitive to the environment, but the maxima in the radial component of the 3s and 3d wavefunctions occur at about the same distance from the nucleus. Thus, changes in the 3d orbitals which are sensitive to environment, can change the amount that the 3s orbitals are shielded from nucleus, and then, change the electron density at the nucleus. Ferrous compounds exhibit lower electron density than ferric because they have six 3d electrons compared with a nominal five on the ferric ions. This means that Fe^{3+} ion has a smaller radius respect to Fe^{2+} ion and therefore the electrons are closer to the nucleus.

The effect of pressure on the CS of ionic compounds will depend on the effect of the 3d-3s shielding. The parameters which measure the repulsion between 3d electrons on a given ion (Racah parameters) decrease with increasing pressure. This can be interpreted as a spreading out of the 3d electron orbitals or at least as a change in the position of the maximum with pressure. Thus, one would predict an increase in electron density at the iron nucleus with pressure. For compounds with appreciable covalent binding, in addition to this effect, it exists the possibility of variations in hybridization or orbital occupation. These changes could act to increase or diminish the shielding effect. In iron oxalate the CS decreased with increasing pressure which corresponds to an increase in electron density at the iron nucleus with pressure. This is consistent with the reduction in the 3d shielding discussed above. The ferric compounds show less change in CS with pressure than do the ferrous. This is perhaps not unreasonable, as the ferrous ions involves six 3d electrons, while the ferric ions have “just” five.

As concerning the QS, it depends on the electric field gradient at the nucleus, which is established both by asymmetries in the 3d electron distribution and by the direct influence of noncubic point symmetry. For most compounds there is an increase in QS with pressure and the ferrous compounds exhibit a much larger QS than the ferric ones. High spin ferrous compounds are normally characterized by high QS values,

while HS ferric compounds exhibit little or no splitting since $3d^5$ is an S state (more symmetric and less degenerate).

These considerations are in agreement with the interpretation of the Mössbauer data given in the Chapter 3.1.2.1. By looking at the changes in CS and QS values (Table 3.1.2.1), I could divide the curves shown in Figures 4.5.1 into separate segments of different colors to better emphasize the atomic or electronic structural changes during compression (Fig. 4.5.2).

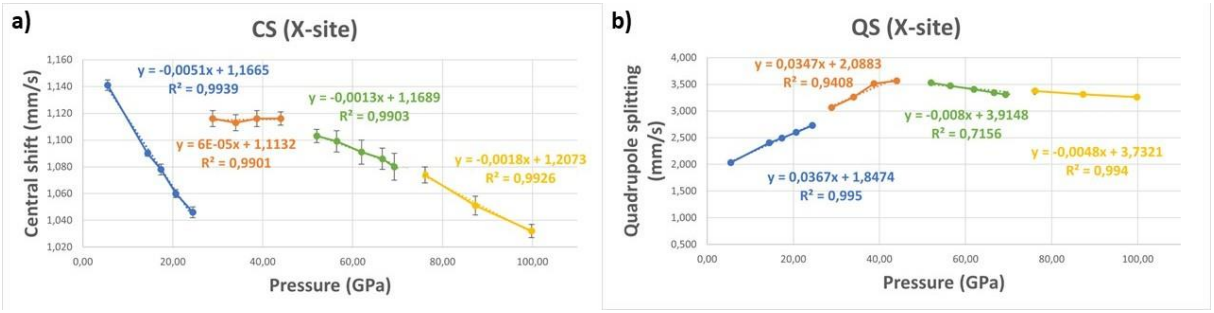

Figure 4.5.2: a) Trendlines for the evolution with pressure of CS of X site and b) trendlines for the evolution with pressure of QS of Y site.

The slop of the line is a qualitative indication of how fast the site is changing, while the variations of the CS and QS is representative for changes in coordination and configuration. From 5.5 GPa to 24 GPa (blue lines) the oxalate structure undergoes to simple compaction (increased electronic density at the iron nuclei) correlated to some distortion of the octahedral site, causing the increment of the EFG (expressed by the rising QS). Between 24 GPa and ~ 40 GPa (orange lines) a sluggish transition characterized by a progressive increase in the coordination environment around the iron atoms is evidenced by a sharp rise in the CS, which remains constant and does not lessen due to compaction until 44 GPa. In the same pressure interval, the QS continue rising at the same rate, however shifted to higher values above 24 GPa, confirmed by the higher offset of the orange line with respect to the blue, also an indication of progressive structural changes. The appearance of the second doublet, between 52 GPa and ~ 70 GPa (green lines), is attributed to the onset of a spin crossover, coupled (or not) to a structural transition. In this pressure range both CS and QS decrease following a linear trend. We expect a last structural transition above 70 GPa, or at least changes in the local environment around the iron nuclei, because both CS and QS shows deviations from the lower pressure trend, i.e. the CS keeps dropping however at a higher rate while the QS smoothly rise to then continue the trend to lower values, providing indication for a progressive regain in symmetry of the iron site.

In order to have a complete analysis of how the structure of the sample evolves under compression it is also useful to consider Raman data. Raman spectroscopy provides direct insight into the vibrational behavior of ionic pairs and molecules bonded together, thus their variation as a response to changes of external parameters such as pressure and temperature are also indicative for structural and electronic transitions.

Dihydrate oxalates belong to the point group D_{2d}, in which the vibrational activity is given by $\Gamma = 3A_1 + B_1 + 2B_1 + 3E$. Thus, all modes are Raman active and the $2B_1 + 3E$ modes are infrared active. All oxygens in the structure are equivalent and hence only one symmetric stretching mode should occur. Upon coordination of the oxalate as a mono-oxalate species, the symmetry is reduced to C_{2v}. The irreducible expression is then given by $\Gamma = 6A_1 + 2A_2 + 5B_1 + 2B_2$. Hence all modes are both Raman and infrared active. In this situation both the symmetric and antisymmetric stretching modes will be observed. If two oxalate molecules are bonded to the cation (Fe, Ni, Mn, Cu, …), then the molecular point group will be D_{2h} and the irreducible representation is given by $\Gamma = 7A_g + 3B_{1g} + 3B_{2g} + 5B_{3g} + 3A_u + 7B_{1u} + 7B_{2u} + 4B_{3u}$. The first four modes are Raman active and the last four modes are infrared active. Under this symmetry, there is a center of symmetry which means the infrared and Raman bands are exclusive.

$FeC_2O_4 \times 2\ H_2O$ is composed of bidentate oxalate dianions $C_2O_4^{2-}$, divalent ferrous Fe^{2+} ions, and water molecules. The alternating planar arrangement of oxalate dianions ($C_2O_4^{2-}$) and Fe^{2+} cations result in one-dimensional infinite linear chains along the b-axis. The octahedral coordination sphere of each Fe^{2+} ion comprises four oxygen atoms of two oxalate dianions on equatorial positions and is completed by the oxygen atoms of two water molecules on axial positions approximately parallel to a-axis. The mineral crystallizes in the monoclinic system, space group C2/c, and belongs to the point group D_{2h}. For symmetry reasons (as explained in the earlier paragraph) the sample give rise to modes that are Raman active. The Table 4.5.1 shows the Raman bands assigned in literature [67, 68, 69] to the mineral humboldtine (the natural correspondent of our sample).

Fe^{2+} (humboldtine)	Band assignment
3315 cm^{-1}	OH stretching
1708 cm^{-1}	$\upsilon_{a(C=O)}$
1555 cm^{-1}	$\upsilon_{a(C=O)}$
1468 cm^{-1}	$\upsilon_{s(C-O)} + \upsilon_{(C-C)}$
1450 cm^{-1}	$\upsilon_{s(C-O)} + \delta_{(O-C=0)}$
913 cm^{-1}	$\upsilon_{s(C-C)} + \delta_{(O-C=0)}$
856 cm^{-1}	$\upsilon_{s(C-C)}$ / $\delta_{(O-C-0)}$
582 cm^{-1}	Water libration
518 cm^{-1}	$\upsilon_{s(Fe-O)} + \upsilon_{(C-C)}$
293 cm^{-1}	out of plane bends
246 cm^{-1}	Lattice mode
203 cm^{-1}	Lattice mode

Table 4.5.1: Raman active mode of humboldtine.

It is known that the O–H stretching frequency regions of humboldtine is around 3316 cm^{-1} while prominent C–O stretching bands is observed at 1468 cm^{-1}. A low intensity band, attribute to C–O antisymmetric stretching vibration, is observed in the Raman spectra at 1708 cm^{-1}. The sharp bands centered at 585 and 915 cm^{-1} in the spectrum of humboldtine are assigned to water libration and O–C–O bending modes respectively. The observation of different C–O symmetric stretching vibrations provides credence to the existence of different phases in the sample, but at least in our case, single crystal XRD confirms the presence of only one phase at least up to ~ 24 GPa. The broad band centered at 523 cm^{-1} is assigned to Fe^{2+}–O stretching vibration and in addition, the band doublet at 204/245 cm^{-1} is attributed to lattice modes. The coordination environment of Fe^{2+} is a distorted octahedron where the two metal-water bonds (Fe–O3) are shorter than the other four metal-oxalate bonds (Fe–O1 and Fe–O2). For this reason, we can have multiple peaks in the region of the Fe^{2+}–O stretching band. Considering the arrangements of water molecules in the crystal structure, these water molecules are

obliquely tied to the chains consisting of metal cations and oxalate anions. In the low-frequency region of the Raman spectra of water, there exist intermolecular fluctuation bands which are due to the interaction between water molecules through the hydrogen bonds. The librational or restricted rotational Raman bands from liquid H_2O occur within the region 200-1100 cm^{-1}. The restricted translational motions of H_2O molecules involved in hydrogen bond interactions are equivalent to the bending and stretching motions of the O-H ° ° O units. If we increase pressure, we change the tilt and we can change the distance from the molecule and so the strength of the O-H and hydrogen bonds. As observed from Mössbauer, increasing the pressure introduces modifications at the structural and electronic level with the consequent adjustment in the polarity of the atom's bonds. All these changes will rise the number and complexity of the Raman active modes and of the observed Raman bands.

The following figure (Fig. 4.5.3) shows the evolution of the Raman shift of the principal identified band modes at the increasing of the pressure.

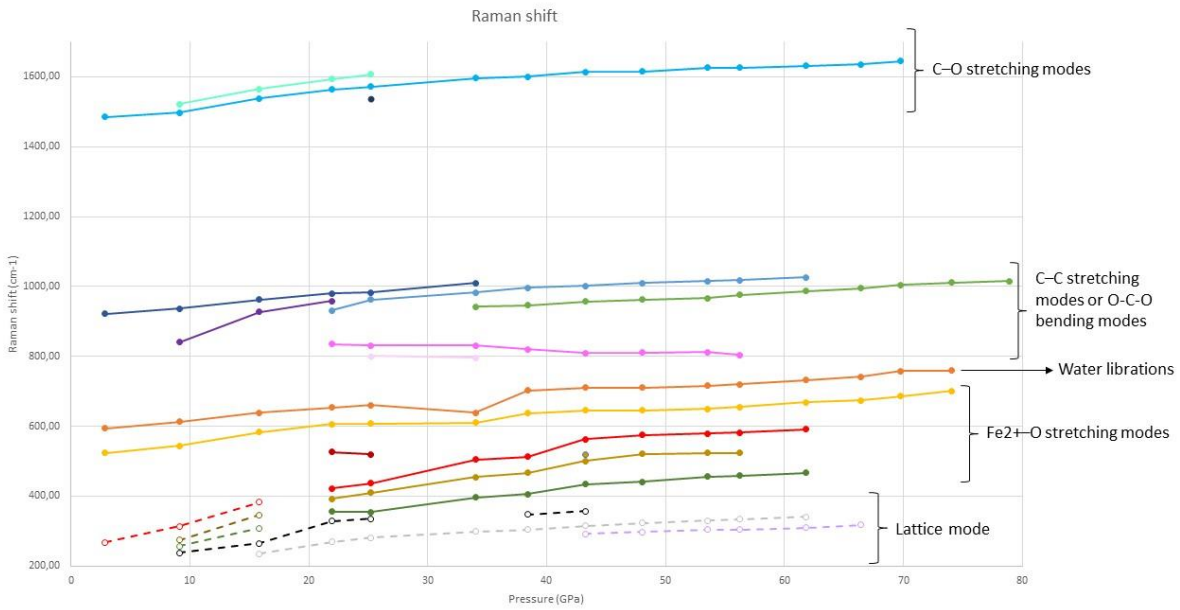

Figure 4.5.3: Evolution of the Raman shift of the principal band modes at the increasing of the pressure.

At ~ 22 GPa it is well known by now that the sample undergoes to a structural transition [1]. Indeed, I can notice that at this pressure a lot of new peaks of C-C, O-C-O and Fe-O modes start to appear. From literature [1], it is known that the sample has a high compressibility along the a- and c-axes and that the c-axis is stiffer than the a-axis (the stacking direction of the oxalate chains) because of the alignment of the

hydrogen bonds. Indeed, the value of the oblique angle H_2O-Fe-OH_2 decrease because the water molecule act as flexible joints of the molecular architecture. Pressure also affects the Fe-O bond distances and so it affects the strength of the O-H bond. The shortening of the Fe-O distances translates into a strengthening of these bonds, which may result in additional polarization, while the C-O bond length of the oxalate anions are only little affected by the compression, at least until the first phase transition. The b-axis shows a much lower and almost linear pressure dependence but it also shrinks with increasing pressures and it results in a decreasing in the length of the 1-D polymeric chains. As pressure increases, oxalate chains approach each other and the hydrogen H…O bond distances between neighboring chains get shorter. This is confirmed from the slope of the lines in Figure 4.5.3 that describes the evolution of the Raman shift of the different bands at increasing pressures. From Figure 4.5.3 one can notice that the Fe-O modes change faster respect to the C-C or O-C-O modes because the C-O bonds are less affected by the compression respect the H_2O-Fe-O_2H bonds. In particular, at due to compaction the bonds length gets shorter, which is reflected in higher vibration frequencies and so the shift of the bands in higher wavenumbers. These differences in the velocity of the shifting of the modes are highlighted in Figure 4.5.4 where I added the trendlines of the different modes.

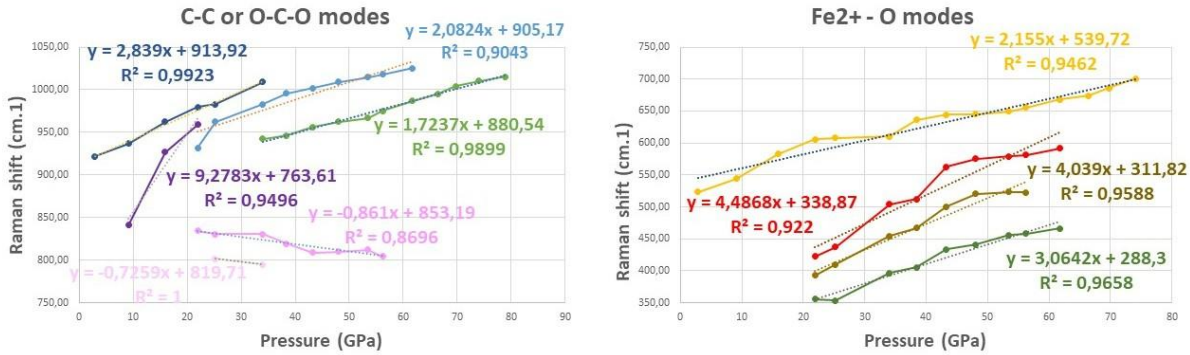

Figure 4.5.4: Evolution of the Raman shift of the principal band modes at the increasing of the pressure with the respective trendlines.

In order to confirm the structural evolution under compression of the sample the most useful technique is the XRD. XRD analysis identifies the long-range order (i.e., the structure) of crystalline materials and the short-range order of non-crystalline materials (X-ray total scattering). From X-ray diffraction patter, one can extract structural types, lattice constants, average grain size, degree of crystallinity, and crystal defects. However, as already said in the previous chapter, here we only describe a qualitative analysis made with Dioptas and preliminary observations made with CrysAlis^{PRO}. Dioptas qualitative analyses are useful to visualize the pressure

ranges of structural transition in the sample, which are reflected in changes in the peaks of the XRD patterns (Fig. 3.2.2.1.2).

The structural transition observed from the qualitative analyses of XRD patterns are in agreement with the already presented Mössbauer and Raman data. However, the presence of twinning in the selected single crystal led us to misinterpret the results, and we initially attributed the possible occurrence of structural modifications already at 7.9 GPa, which was not observed in the previous study from Müller et al. 2021 [1]. From the preliminary analysis made with CrysAlis^{PRO}, I can affirm that these changes are not due to a structural transition. Indeed, due to the twinning of the initial crystal, characterized by two distinct crystallographic domains, part of their intensities overlap, emerge or disappeared based on the crystal orientation (or the DAC orientation), and there is no proper way to overcome this only from a qualitative analyses of the integrated XRD patterns.

Regarding the structural transition at P > ~ 22 GPa, from the acquired data it is difficult to unambiguously resolve the new structure. It is possible to get the model of the high-pressure phase but the R1-value does not go below 12%. The poor data-parameter ratio due to small opening of the cell (±30°), the loss of quality of the crystal after the transition and the twinning of the initial crystal are the reasons of poor R-value. Despite the inability to resolve the structures formed during compression, the XRD data agrees with both Mössbauer and Raman results.

4.6 Synthesis of new products through laser heating

One of the goal of this study was to expose Fe oxalate dihydrate to the extreme conditions of planetary interiors, i.e. the Earth, thus not only high pressures but also temperatures. High pressure is reached through the diamond anvil cell while in order to reach high temperatures, i.e. thousands of degree Kelvin we laser heated the sample using two IR lasers (see Method section). Our scope is to understand whether we can synthesize new phases containing Fe, C, O and possibly water (as OH^- groups) starting from our original sample. Indeed, iron is the most abundant transition metal inside our planet, whereas C, O and H are known light elements that might be abundant in specific regions of the Earth's interior, first of all the Earth's core but could be widely spread also through the mantle. Characterizing the forms they could assume inside the Earth is a crucial step in order to better understand how the Earth's formed and differentiated, as well as the origin of life.

DAC1 and DAC2 were laser heated at 50 GPa/~2000 K and 100 GPa/~2400K/~2950K respectively (see Results chapter). From the acquired Mössbauer spectra of DAC1 and DAC2 in two different positions is clear that we were able to synthesis new products (Table 3.1.2.1 and Table 3.1.2.2). Indeed, the spectra before and after the laser heating

show notable differences (Fig. 4.6.1 and Fig. 4.6.2). In Figure 4.6.3 we overlap the spectra collected at different temperatures in different parts of the samples. It is clear from a qualitative observation that heating at (slightly) different temperatures does not change the products, but higher temperatures probably help to react more reagents, thus the spectral differences can be attribute mainly to different reagent/products ratios.

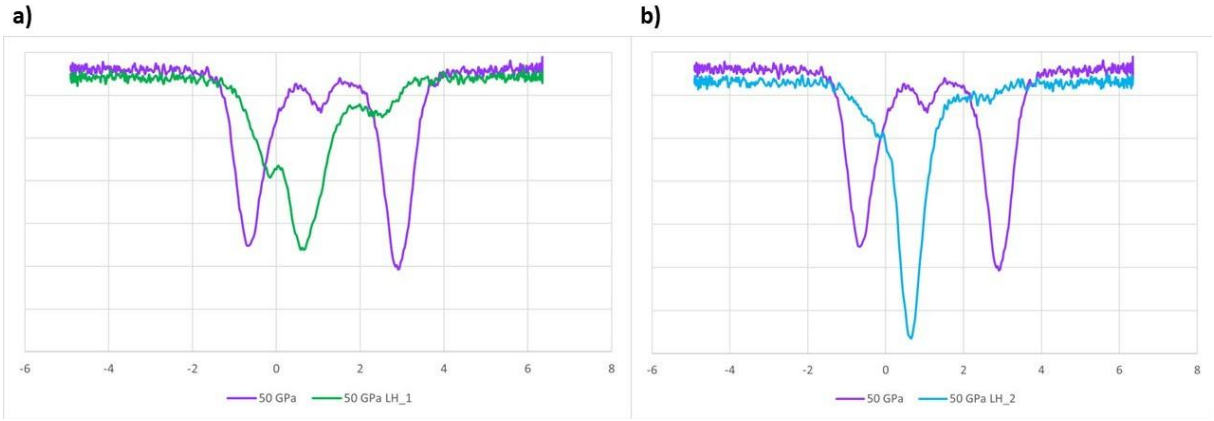

Figure 4.6.1: Mössbauer spectra of DAC1: a) comparison between spectrum acquired before laser heating (violet) and spectrum acquired after laser heating in position 1 (green) and b) comparison between spectrum acquired before laser heating (violet) and spectrum acquired after laser heating in position 2 (light blue).

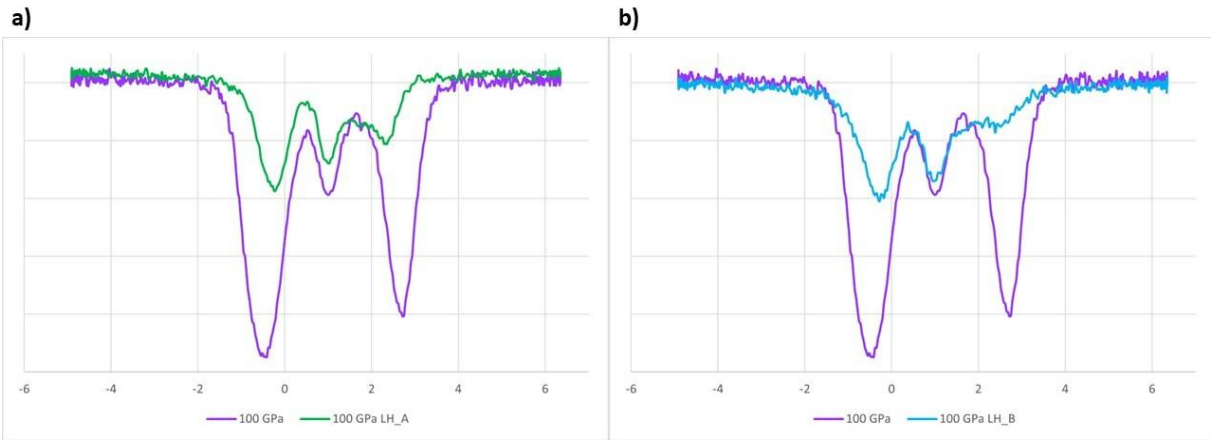

Figure 4.6.2: Mössbauer spectra of DAC2: a) comparison between spectrum acquired before laser heating (violet) and spectrum acquired after laser heating in area A (green) and b) comparison between spectrum acquired before laser heating (violet) and spectrum acquired after laser heating in area B (light blue).

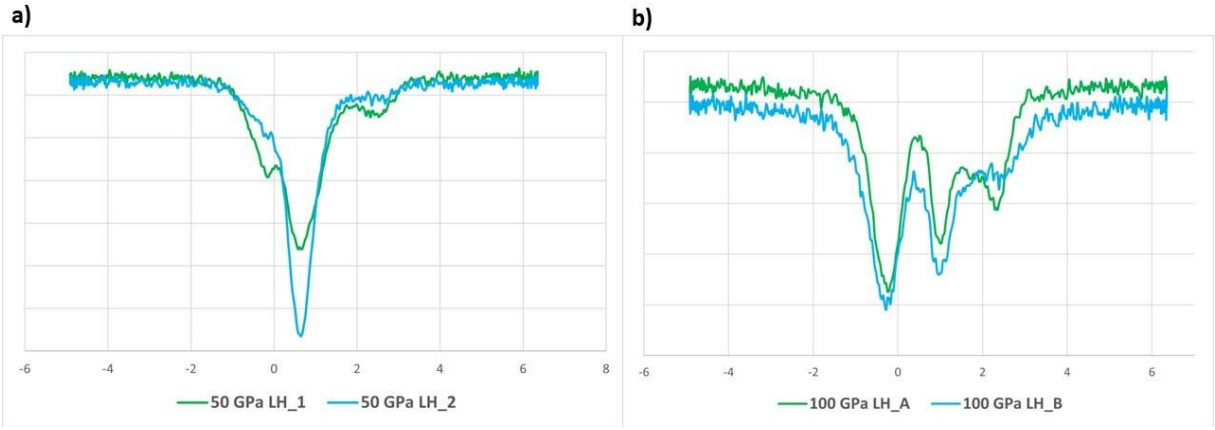

Figure 4.6.3: Mössbauer spectra: a) comparison between spectrum acquired in position 1 (green) and spectrum acquired in position 2 (light blue) and b) comparison between spectrum acquired in area A (green) and spectrum acquired in area B (light blue).

A precise characterization of the products using only Mössbauer spectroscopy is not possible due to the presence of several iron-bearing compounds in the same spectrum, which are very difficult to deconvolve without the use of complementary information from XRD. It is known however that iron oxalate is not stable at high pressures and temperatures and if melted during heating, it can recrystallize as a wide variety of products, such as Fe-oxides, carbonates/tetracarbonates, and other reduced or oxidized species. Thus, in order to better understand and interpret what happened to the sample we must combine Mössbauer and XRD data. From preliminary analyses made with CrysAlis^{Pro} on DAC1, we associate the new reflections on the XRD pattern (Fig. 3.2.2.2.1) to the synthesis of at least two new products, a new tetracarbonate $Fe_5C_3O_{13}$, where Fe^{2+} and Fe^{3+} coexist in the same structure, indicating only partial oxidation, and one or more phases that remains unidentified. Unfortunately, the quality of the refinement for the new tetracarbonate $Fe_5C_3O_{13}$ is not great (R ~ 10%) and a precise structural model cannot be retrieved so far. The main reasons of poor R-value are the small opening of the cell (±30°) which does not allow to collect enough reflections for a proper structural determination. So far single crystal XRD data analysis is still ongoing, but more experiments at similar conditions are necessary (with larger cell opening) to finalize the study. One should note that the new tetracarbonate might host water, in form of OH^- groups, in its structure, since the two molecules of water present in Fe-oxalate dihydrate must have reacted during the transformation/decomposition reaction. A deep analysis on the atomic bonds length might elucidate whether OH groups are contained in the tetracarbonate or if the form different phases, such ice VII or other types of molecules.

Due to the impossibility of resolving the structure of these new phases and therefore knowing the coordination and spin configuration of iron in the products, it is very

difficult to extract from the Mössbauer spectra the correct hyperfine parameters for the components of the obtained phases.

Regarding DAC2, from the preliminary analysis we found a known phase, a tetracarbonate already discovered few years ago [13]. This is an orthocarbonate $Fe_4C_3O_{12}$ in which all iron is ferric (Fe^{+3}) and in which there are two structurally distinct iron position. The Fe atom in position 1 is surrounded by nine O atoms forming a regular trigonal prism while the Fe atom in position 2 is located in a bicapped trigonal prism coordinated by oxygens. The presence of other phases in not excluded, several reflections were not indexed, but one has to carefully look at the data. In previous studies [13], the transformation of $FeCO_3$ was related to $Fe_4C_3O_{12}$ + $Fe_{13}O_{19}$, however other oxides, such as hp-Fe_3O_4, Fe_4O_5, Fe_7O_9, FeO_2, etc. [70, 71, 72] might be present. In DAC2, the formation of the new high-pressure phase ($Fe_4C_3O_{12}$) was associated with complete oxidation of Fe^{2+} to Fe^{3+} and production of reduced carbon compounds such as diamonds or CO and other iron oxides [73]. The initial amount of Fe^{2+} is also of significant importance since the nature of the high-pressure phase depends on the Fe^{2+} content. It was demonstrated experimentally that in $Fe_4C_3O_{12}$ only ferric iron is present [13] and that the electronic configuration of iron is in the high-spin state, as the distance between iron and oxygen atoms is indicative of ferric iron complexes in a high-spin state [74]. Although the difficulty to have a complete analysis of the new product only through Mössbauer spectroscopy, our results are in agreement with this other studies. Indeed, following what was already known from literature, I performed the fitting with MossA software using the lowest amount of component i.e two doublets for the two sites of the ferric atom (Fig. 4.6.4). Thus, I did not consider all the extra component due to iron oxalate formed during laser heating.

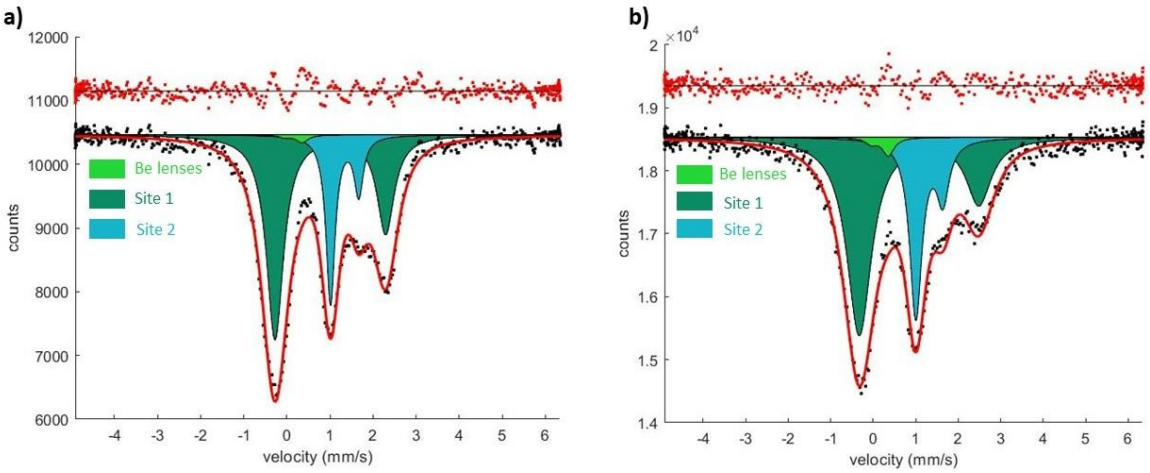

Figure 4.6.4: Mössbauer spectra fitted using MossA software package: a) DAC 2 at 100 GPa after LH in area A and b) DAC 2 at 100 GPa after LH in area B.

The value of CS of both sites are ~ 1.05 mm/s (site 1) and ~ 1.33 mm/s (site 2) (Table 3.1.2.2). These values are too high to be iron in low spin configuration and thus, are in agreement with the assumption of being iron in high spin.

The ability to synthesize the orthocarbonate at different P/T conditions and from many different reagents is reported in the literature. $Fe_4C_3O_{12}$ was synthesized from $FeCO_3$ heated at ~ 70 GPa and 1750 K [13]. Its formation was also described by combining $(Mg_{0.4}, Fe_{0.6})O$ and CO_2 at P > 80 GPa and 2000 K [75] or using FeO, Fe_2O_3, or FeO(OH) oxides embedded in CO_2 at P > 40 GPa and T ~ 1500 K [73]. In this study it formed starting from $FeC_2O_4 \times 2\ H_2O$ at 100 GPa and T > 2900 K, however it cannot be excluded that $FeCO_3$ was the first product of the reaction, which might have formed as a transient phase before the complete conversion to orthocarbonate, following the reaction:

$$4FeC_2O_4 \times 8H_2O \rightarrow 4FeCO_3 + 4CO + 8H_2O \rightarrow Fe_4C_3O_{12} + C + 4CO + 8H_2O$$

Anyway, despite the kinetics of reaction, the broad P/T stability range of $Fe_4C_3O_{12}$ corroborates the theory that it might exist at great depth inside our planet.

In this study, we performed an experimental investigation of the high-pressure high-temperature behaviour of iron oxalate dihydrate and the experimental conditions reached are that of deep Earth. From our results we revealed an already discovered compound containing tetrahedral CO_4 groups ($Fe_4C_3O_{12}$), a new tetracarbonate $Fe_5C_3O_{13}$, which may contain OH group in its structure and the complex role of ferrous and ferric iron in stabilizing carbonates at extreme conditions. These results are important for both the carbon recycle in deep Earth and the deep water cycle in subducting slabs. Indeed, the presence of this new orthocarbonate, at P-T conditions typical for the deep Earth, suggests a strong stability of this phase against dissociation into simple oxide. Also, the preference of the new high-pressure phase for Fe^{3+} implies reduction of part of the carbon and the coexistence of oxidized and reduced species of carbon at lower mantle conditions [75]. This behavior might be due to a strong thermodynamic stability of the new carbon-bearing phase. However, for this new phase to be actually present in the deep lower mantle, carbonates must be preserved during deep subduction. It could happen if they are transported in a relatively cold subducted slab where oxygen fugacity is locally higher because due to particular local mineral assemblage [76]. This fraction of surviving carbonates may be transported beyond in lower mantel and transform into the newly observed Fe^{3+}-bearing phase.

5. Conclusions and outlook

This thesis focused on the study of the structural evolution of $FeC_2O_4 \times 2\ H_2O$ at high pressures and its stability, i.e. phase transformation or decomposition, at extreme pressures and temperatures. Investigations on the structural changes and physico-chemical properties of iron oxalate are relevant in different research fields such as technology (as anode material for lithium-ion batteries), deep carbon cycle (as precursor of $FeCO_3$) and planetary science (as Fe-C-O phase). In order to investigate the behavior of iron oxalate dihydrate we combined different experimental techniques. Synchrotron Mössbauer spectroscopy looks into the local environment around iron nuclei and provides very precise information about the material's chemical, structural, magnetic and time-dependent properties. It was used to study the nuclear and electronic evolution of the sample under compression. X-ray diffraction is the most powerful tool used for identifying a crystalline material and determining its atomic structure. XRD was used to investigate changes in the long-range ordered structure. Raman spectroscopy is a non-destructive technique used for observation of vibrational, rotational and other low-frequency modes in solid, liquid and gases complexes. It was used to investigate the vibrational behavior of ions or groups of ions bonded together and their variation as a response to changes of external parameters such as pressure and temperature. These techniques are complementary and essential to reach a complete analysis of how the sample reacted to the variations in extremal parameters. The results obtained in this thesis can be summarized as follows:

i. We determined how many structural/phase transitions happen in $FeC_2O_4 \times 2\ H_2O$ up to 100 GPa and their pressure ranges;
ii. We studied the amorphization process;
iii. We synthesized new materials at ~ 50 and ~ 100 GPa and T > 2000 K;
iv. We investigate the spin crossover in iron atoms at P > 50 GPa.

(i) Through SMS, XRD and Raman spectroscopy we confirmed the formation of a new phase starting at ~ 22 GPa [1]. The structural transition happens in a broad P-range and is finally completed at P ~ 38 GPa. Unfortunately, we were not able to resolve the new structure because of the little 2θ range available due to a lower-than-expected opening angle of the DAC (±30°). Moreover, other reasons for the poor obtained R-values are the loss of quality of the crystal after the first transition and the twinning of the initial crystal with the consequent overlap of the intensities of the two twin domains. The only way to determine the structure of the new phase is to redo the experiment using 4 mm diamonds with cell aperture of 80°.

(ii) The initial assumption from Müller et al [1] that the sample would amorphized at P > 20-25 GPa was not confirmed by our study. We instead show that even if the quality of the single crystals used in the experiment decreases after the first structural transition, the material remains crystalline at least until the highest pressure investigate, 100 GPa.

(iii) Through SMS and XRD we confirmed the synthesis of new products at the extreme conditions, with clear implications for the composition of the Earth and the recycling of carbon and water into the deep mantle. At 100 GPa and ~ 2750 K we formed an already discovered orthocarbonate $Fe_4C_3O_{12}$ while at 50 GPa and ~ 2000 K we formed a new tetracarbonate $Fe_5C_3O_{13}$ which may contain OH^- group in its structure. Other phases also formed as products of the redox reactions, but remain still unidentified. Also in this case, we are not able to resolve the new structure because of the poor refinement R-value. In order to properly characterize these new phases, more experiments are required combined to the use of DAC with larger opening, i.e. higher 2θ range.

(iv) Through SMS and Raman spectroscopy we confirmed the spin transition. At P > 50 GPa a second doublet starts to emerge from the Mössbauer spectra and grows until P ~ 70 GPa, where the co-existence of the two components appears to reach a steady-state. In the same pressure range, in the frequency region of the Raman spectra where C-C symmetric stretching modes and O-C-O bending modes are present, the intensity of the peak at lower frequency increases at the expenses of the second peak at higher frequencies. We attribute the rise of the second doublet (in SMS) and the growth of the peak at lower frequencies (in Raman spectroscopy) to the spin transition of iron 3d electrons. However, our interpretation is not yet conclusive, since in the case of spin pairing, one would expect a complete conversion, thus i.e. the progressive disappearance of the first doublet (in SMS) and of the second peak (in Raman spectroscopy), representing iron in a high-spin state, to the advantage of the low-spin (LS) doublet, which does not happen. Other explanations of what we have observed could be i) the p-induced oxidation of Fe^{2+} to Fe^{3+}, caused by the reduction of the oxalate molecule with consequent formation of a new phase, or ii) the transition to a new structure characterized by two distinct iron sites with different coordination numbers and hypothetically different spin states. X-ray emission spectroscopy (XES) is the ideal analytical technique to address this question. Indeed, Mossbauer spectroscopy is not influenced directly by the spin state but it can serve as a genuine probe through its sensitivity to the (re)distribution of the 3d electrons. On the other hand, X-ray emission spectroscopy is the best technique to look into spin transition, since spin pairing in 3d orbital can be directly probed from changes in Fe Kβ and Fe Kβ' emission lines, which express electronic transitions between 3d to 2p electrons

shells [77]. We applied for beamtime at ID20 at the ESRF to perform XES experiment on Fe oxalate and clarify this issue once and for all.

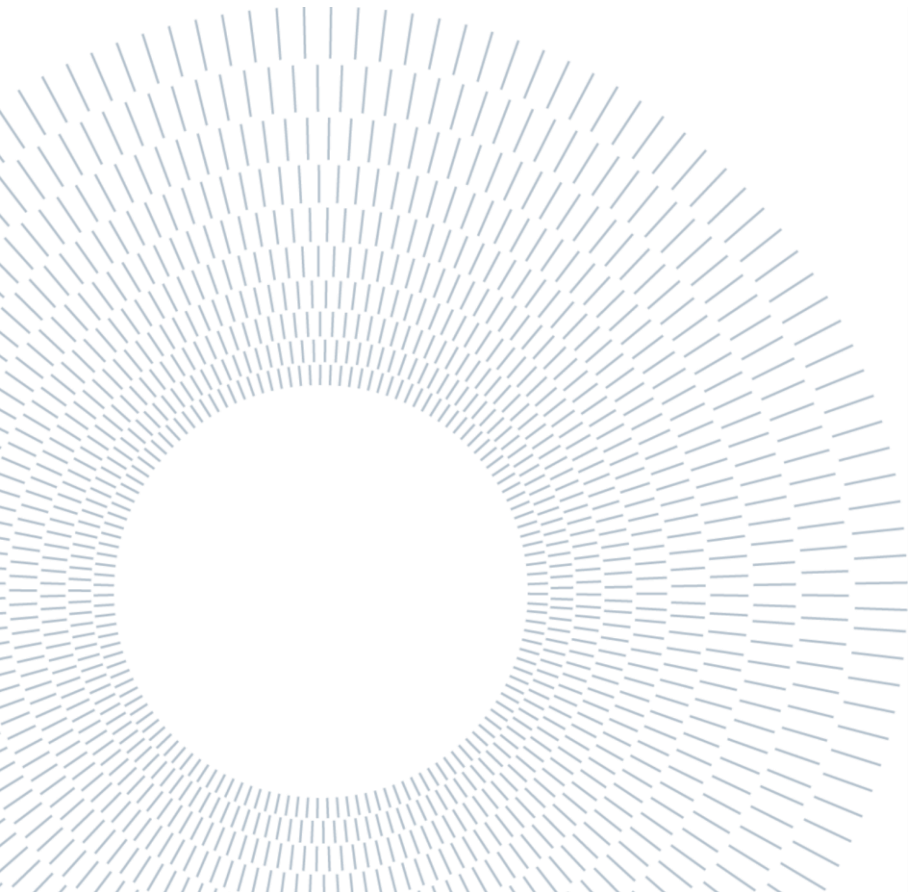

Bibliography

[1] Müller, H., Bourcet, L., Hanfland, M. (2021). Iron(II)oxalate Dihydrate-Humboldtine: Synthesis, Spectroscopic and Structural Properties of a Versatile Precursor for High Pressure Research. Minerals 11, 113.

[2] Liu, Z.-J., Liu, W., Wang, Y. and Guo, M.-L. (2016) Preparation of β-ferrous oxalate dehydrate layered nano sheets by mechanochemical method and its visible light-driven photocatalytic performance. Mat. Lett., 178, 83–86.

[3] Yamada, T., Sadakiyo, M. and Kitagawa, H. (2009). High proton conductivity of one-dimensional ferrous oxalate dihydrate. J. Am. Chem. Soc., 131, 9.

[4] Poizot, P., Laruelle, S., Grugeon, S. et al. (2000) Nano-sized transition-metal oxides as negative-electrode materials for lithium-ion batteries. Nature 407, 496–499.

[5] Li, N., Li, Q., Guo, X, Yuan, M. and Pang, H. (2019). Controllable synthesis of oxalate and oxalate-derived nanomaterials for applications in electrochemistry. Chemical Engineering Journal, 372.

[6] Zhang, K., Li, Y., Wang, Y., Zhao, J., Chen, X., Dai, Y. and Yao, Y. (2020). Enhanced electrochemical properties of iron oxalate with more stable Li^+ ions diffusion channels by controlling polymorphic structure. Chemical Engineering Journal, 384.

[7] Oh, HJ., Jo, CH., Yoon, C. et al. (2016). Nickel oxalate dihydrate nanorods attached to reduced graphene oxide sheets as a high-capacity anode for rechargeable lithium batteries. NPG Asia Mater, 8, e270.

[8] Wu, X., Guo, J., McDonald, M. J., Li, S., Xu, B. and Yang, Y. (2015). Synthesis and characterization of urchin-like $Mn_{0.33}Co_{0.67}C_2O_4$ for Li-ion batteries: Role of SEI layers for enhanced electrochemical properties. Electrochimica Acta, Volume 163.

[9] Aragon, M. J., Leon, B., Vincente, C. P. and Tirado, J. L. (2008). Synthesis and Electrochemical Reaction with Lithium of Mesoporous Iron Oxalate Nanoribbons. Inog. Chem., 47.

[10] Zhang, K., Li, Y., Hu, X., Liang, F., Wang, F., Xu, R., Dai, Y. and Yao, Y. (2021). Inhibitive role of crystal water on lithium storage for multilayer $FeC_2O_4 \cdot xH_2O$ anode materials. Chemical Engineering Journal, 404.

[11] Orcutt, B. N., Daniel, I. and Dasgupta, R. (2019). Deep Carbon: Past to Present. Cambridge University Press.

[12] Boulard, E., Menguy, N., Auzende, A. L., Benzerara., K., Bureau, H., Antonageli, D., Corgne, A., Morard, G., Siebert, J., Perillat, J. P. et al. (2012). Experimental investigation of the stability of Fe-rich carbonates in the lower mantle. J. Geophys. Res., 117.

[13] Cerantola, V., Bykova, E., Kupenko, I., Merlini, M., Ismailova, L., McCammon, C., Bykov, M., Chumakov, A., Petitgirard, S., Kantor, I. et al. (2017). Stability of iron-bearing carbonates in the deep earth's interior. Nat. Comm., 8.

[14] Peacock, S. M. (1990). Fluid processes in subduction zones. Science, 248.

[15] Pearson, D., Brenker, F., Nestola, F. et al. (2016). Hydrous mantle transition zone indicated by ringwoodite included within diamond. Nature 507, 221–224.

[16] Pépin, C. M., Dewale, A., Geneste, G., Loubeyre, P. and Mezouar, M. (2014). New Iron Hydrides under High Pressure. Phys. Rev. Lett., 133.

[17] Fortney, J.J., Nettelmann, N. (2010). The Interior Structure, Composition, and Evolution of Giant Planets. Space Sci. Rev., 152.

[18] Kraus, D., Vorberger, J., Pak, A. et al. (2017). Formation of diamonds in laser-compressed hydrocarbons at planetary interior conditions. Nat. Astron., 1.

[19] Baren, E. J. (2016). Natural iron oxalates and their analogous synthetic counterparts: A review. Chemie der Erde, 76.

[20] Chen, J., Blume, H.P. and Beyer, L. (2000). Weathering of rocks induced by lichen colonization. A review. Catena, 39.

[21] Adamo, P. and Violante, P. (2000). Weathering of rocks and neogenesis of minerals associated with lichen activity. Appl. Clay Sci. 16.

[22] Zelenskaya, M. S., Izatulina, A. R., Frank-Kamenetskaya, O. V. and Vlasov, D. Y. (2021). Iron Oxalate Humboldtine Crystallization by Fungus Aspergillus niger. Crystals, 11.

[23] Weir, C., Lippincott, E., Van Valkenburg, A., Bunting, E., (1959). Infrared studies in the 1- to 15-micron region to 30,000 atmospheres. J. Res. NBS, Sect. A Phys. Chem. 63A.

[24] Kantor, I., Prakapenka, V., Kantor, A., Dera, P., Kurnosov, A., Sinogeikin, S., Dubrovinskaia, N., Dubrovinsky, L., (2012). BX90: A new diamond anvil cell design for X-ray diffraction and optical measurements. Review of Scientific Instruments, 83, 125102.

[25] Letoullec, R., Pinceaux, J. P. and Loubeyre, P. (2006). The membrane diamond anvil cell: A new device for generating continuous pressure and temperature variations. High Pressure Research, 1.

[26] Kurnosov, A., Kantor, I., Boffa-Ballaran, T., Lindhardt, S., Dubrovinsky, L., Kuznetsov, A., and Zehnder, B.H. (2008) A novel gas-loading system for mechanically closing of various types of diamond anvil cells. Review of Scientific Instruments, 79, 045110.

[27] URL: https://www.esrf.fr/home/UsersAndScience/Experiments/MEx/ID18/beamline_layout.html

[28] Dewael, A., Torrent, M., Loubeyre, P., Mezouar, M. (2008). Compression curves of transition metals in the Mbar range: Experiments and projector augmented-wave calculations. Phys Rev B, 78, 104102.

[29] Shen, G., Wang, Y., Dewaele, A. et al. (2020). Toward an international practical pressure scale: A proposal for an IPPS ruby gauge (IPPS-Ruby2020). High Pres. Res. 40(1).

[30] Akahama, Y., Kawamura, H. (2006). Pressure calibration of diamond anvil Raman gauge to 310 GPa. Journal of Applied Physics, 100, 043516.

[31] Mezouar, M., Giampaoli, R., Garbarino, G., Kantor, I., Dewaele, A., Weck, G., Boccato, S., Svitlyk, V., Rosa, A. D., Torchio, R., Mathon, O., Hignette, O. and Bauchau, S. (2017). Methodology for in situ synchrotron X-ray studies in the laser-heated diamond anvil cell. High Pressure Research, 37, 2.

[32] Konôpková, Z., Morgenroth, W., Husband, R., Giordano, N., Pakhomova, A., Gutowski, O., Wendt, M., Glazyrin, K., Ehnes, A., Delitz, J. T., Goncharov, A. F., Prakapenka, V. B. and Liermann, H.-P. (2021). Laser heating system at the Extreme Conditions Beamline, P02.2, PETRA III. J. Synchrotron Rad., 28.

[33] Kupenko, I., Dubrovinsky, L., Dubrovinskaia, N., McCammon, C., Glazyrin, K., Bykova, E., Boffa Ballaran, T., Sinmyo, R., Chumakov, A. I., Potapkin, V., Kantor, A., Rüffer, R., Hanfland, M., Crichton, W. and Merlini, M. (2012). Portable double-sided laser-heating system for Mössbauer spectroscopy and X-ray diffraction experiments at synchrotron facilities with diamond anvil cells. Review of Scientific Instruments, 83.

[34] Aprilis, G., Strohm, C., Kupenko, I., Linhardt, S., Laskin, A., Vasiukov, D. M., Cerantola, V., Koemets, E. G., McCammon, C., Kurnosov, A., Chumakov, A. I., Rüffer, R., Dubrovinskaia, N., Dubrovinsky, L. (2017). Portable double-sided pulsed laser heating system for time-resolved geoscience and materials science applications. Review of Scientific Instruments, 88.

[35] Mössbauer, R. L. (1958). Nuclear resonance absorption of gamma radiation in Ir191. Naturwissenschaften (West Germany). 45.

[36] Yoshida, Y., Suzuki, K., Hayakawa, K., Yukihira, K., Soejima, H. (2009). Mössbauer spectroscopic microscope. Hyperfine Interact, 188.

[37] Potapkin, V., McCammon, C., Glazyrin, K. et al. (2013). Effect of iron oxidation state on the electrical conductivity of the Earth's lower mantle. Nat. Commun., 4.

[38] Troyan, I., Gavrilik, A., Rüffer, R., Chumakov, A., Mironovich, A., Lyubutin, I., Pereklain, D., Drozdov, A. P. and Eremets, M. (2016). Observation of superconductivity in hydrogen sulfide from nuclear resonant scattering. Science, 351, 6279.

[39] Potapkin, V., McCammon, C., Glazyrin, K., Kantor, A., Kupenko, I., Prescher, C., Sinmyo, R., Smirnov, G. V., Popov, S., Chumakov, A. I., Rüffer, R., Dubrovinsky, L. (2012). The 57Fe Synchrotron Mössbauer Source at the ESRF. J. Synchrotron Rad, 19.

[40] Smirnov, G. V., Sklyarevskii, V. V., Voscanian, R. A., Artem'ev, A. N. (1969). Nuclear diffraction of resonant γ radiation by an antiferromagnetic crystal. Soviet Journal of Experimental and Theoretical Physics Letters, 9.

[41] Smirnov, G. V., Zelepukhin, M. V., van Bürck, U. (1986). Purely nuclear diffraction of Mössbauer radiation in the critical region near the Néel point. JEPT Lett., 43.

[42] Smirnov, G.V. (2000). Synchrotron Mössbauer source of 57Fe radiation. Hyperfine Interactions, 125.

[43] Smirnov, G. V., Chumakov, A. I., Potapkin, V., Rüffer, R., Popov, S. L. (2011). Multispace quantum interference in a 57Fd synchrotron Mössbauer source. Phys. Rev. A, 84.

[44] Mitsui, T., Hirao, N., Ohishi, Y., Masuda, R., Nakamura, Y., Enoki, H., Sakaki, K., Seto, M. (2009). Development of an energy-domain 57Fe-Mössbauer spectrometer using synchrotron radiation and its application to ultrahigh-pressure studies with a diamond anvil cell. J. Synchrotron Rad., 16.

[45] Merlini, M., Hanfland, M. (2013). Single-crystal diffraction at megabar conditions by synchrotron radiation. High Pressure Research, 33(3).

[46] URL: https://kantor.50webs.com/ruby.htm

[47] Prescher, C., McCammon, C., Dubrovinsky, L. (2012). MossA: a program for analyzing energy-domain Mössbauer spectra from conventional and synchrotron sources. Journal of Applied Crystallography, 45.

[48] Cerantola, V. et al. (2015.) High-pressure spectroscopic study of siderite ($FeCO_3$) with focus on spin crossover. Am. Mineral, 100.

[49] Kupenko, I., McCammon, C., Sinmyo, R., Cerantola, V., Potapkin, V, Chumakov, A. I., Kantor, A., Rüffer, R. and Dubrovinsky, L. (2015). Oxidation state of the lower mantle: In situ observations of the iron electronic configuration in bridgmanite at extreme conditions. Earth and Planetary Science Letters, 423.

[50] Prescher, C. (2017). Dioptas Documentation, Release 0.4.0.

[51] Prescher, C., Prakapenka, V.B. (2015). DIOPTAS: a program for reduction of two-dimensional X-ray diffraction data and data exploration. High Press. Res. 35:3, 223–230.

[52] Moberly, J.G., Bernards, M.T., Waynant, K.V. (2018). Key features and updates for Origin 2018. Journal of Cheminformatics, 10, 5.

[53] Buckingham, A.D. (1960). A theory of frequency, intensity and bandwidth changes due to solvents in infra-red spectroscopy., Proc. R. Soc. Lond., 255(A).

[54] Pfannes, H. D. and Gonser, U. (1973). Goldanskii-Karyagin Effect Versus Preferred Orientations (Texture). Appl. Phys., 1.

[55] Lin, J.-F., Speziale, S., Mao, Z. and Marquardt, H. (2013). Effects of the electronic spin transitions of iron in lower mantle minerals: implications for deep mantle geophysics and geochemistry. Rev. Geophys., 51.

[56] Shannon, R. D. (1976). Revised Effective Ionic Radii and Systematic Studies of Interatomie Distances in Halides and Chaleogenides. Acta Cryst., A32, 751.

[57] Schupp, B., Heines, P., Savin, A. and Keller, H. L. (2000). Crystal Structures and Pressure-Induced Redox Reaction of $Cs_2PdI_4 \cdot I_2$ to Cs_2PdI_6. Inorg. Chem., 39, 4.

[58] Heines, P., Keller, H. L., Armbruster, M., Schwarz, U. and Tse, J. (2006). Pressure-Induced Interanl Redox Reaction of $Cs_2[PdI_4]\cdot I_2$, $Cs_2[PdBr_4]\cdot I_2$ and $Cs_2[CI_4]\cdot I_2$. Inorg. Chem., 45, 24.

[59] Slichter, C. P. and Drickamer, H. G. (1972). Pressure-Induced Electronic Changes in Compounds of Iron. J. Chem. Phys. 56, 2142.

[60] Kupenko, I., McCammon, C., Sinmyo, R., Cerantola, V., Potapkin, V., Chumakov, A.I., Kantor, A., Rüffer, R. and Dubrovinsky, L. (2015). Oxidation state of the lower

mantle: In situ observations of the iron electronic configuration in bridgmanite at extreme conditions. Earth and Planetary Science Letters, 423.

[61] Speziale, S., A. Milner, V. E. Lee, S. M. Clark, M. P. Pasternak, and R. Jeanloz. (2005). Iron spin transition in Earth's mantle. Proc. Natl. Acad. Sci. U.S.A., 102.

[62] Kantor, I. Yu. and Dubrovinsky, L. S. and McCammon, C. A. (2006). Spin crossover in (Mg, Fe)O: A Mössbauer effect study with an alternative interpretation of X-ray emission spectroscopy data. Phys. Rev. B, 73, 10.

[63] Gütlich, P., Link, R. and Trautwein, A. (2011). Mössbauer Spectroscopy and Transition Metal Chemistry. Springer, 10.

[64] Spivak, A., Solopova, N., Cerantola, V. et al. (2014). Raman study of $MgCO_3$–$FeCO_3$ carbonate solid solution at high pressures up to 55 GPa. Phys Chem Minerals, 41.

[65] Echigo, T. and Kimata, M. (2008). Single-crystal X-ray diffraction and spectroscopic studies on humboldtine and lindbergite: weak Jahn -Teller effect on Fe^{+2} ion. Phys Chem Minerals, 35.

[66] Champion, A. R., Vaughan, R. W. and Drickamer, H. G. (2004). Effect of pressure on the Mössbauer resonance in ionic compounds of iron. J. Chem. Phys, 47.

[67] Frost, R.L., Jing, Y. and Ding, Z. (2003). Raman and FTIR spectroscopy of natural oxalates: Implications for the evidence of life on Mars. Chinese Science Bulletin, 48, 17.

[68] Frost, R.L and Weier, M.L. (2004). THERMAL DECOMPOSITION OF HUMBOLDTINE A high resolution thermogravimetric and hot stage Raman spectroscopic study. Journal of Thermal Analysis and Calorimetry, 75.

[69] Košek, F., Culka, A., Rousaki, A., Vandenabeele, P. and Jehlička, J. (2020). Evaluation of handheld and portable Raman spectrometers with different laser excitation wavelengths for the detection and characterization of organic minerals. Spectrochimica Acta Part A: Molecular and Biomolecular Spectroscopy, 243.

[70] Bykova, E., Dubrovinsky, L., Dubrovinskaia, N. et al. (2016). Structural complexity of simple Fe_2O_3 at high pressures and temperatures. Nat. Commun., **7**.

[71] Sinmyo, R., Bykova, E., Ovsyannikov, S. et al. (2016). Discovery of Fe_7O_9: a new iron oxide with a complex monoclinic structure. Sci. Rep., 6.

[72] Koemets, E., Leonov, I., Bykov, M., Bykova, E., Chariton, S. et al. (2021). Revealing the Complex Nature of Bonding in the Binary High-Pressure Compound FeO_2. Phys. Rev. Lett., 126.

[73] Boulard, E., Menguy, N., Auzende, A. L., Benzerara, K., Bureau, H., Antonangeli, D., Corgne, A., Morard, G., Siebert, J., Perrillat, J. P., Guyot, F. and Fiquet, G. (2012). Experimental investigation of the stability of Fe-rich carbonates in the lower mantle. Journal of geophysical research, 117.

[74] Lavina, B., Dera, P., Downs, R. T., Yang, W., Sinogeikin, S., Meng, Y., Shen, G. and Schiferl, D. (2010). Structure of siderite FeCO3 to 56 GPa and hysteresis of its spin-pairing transition., Phys. Rev., B, 82.

[75] Boulard, E., A. Gloter, A. Corgne, D. Antonangeli, A. L. Auzende, J. P. Perrillat, F. Guyot, and G. Fiquet. (2011). New host for carbon in the deep Earth. Proc. Natl. Acad. Sci. U. S. A., 108, 13.

[76] Ballhaus, C., Berry, R. F. and Green, D. H. (1990). Oxygen fugacity controls in the Earth's upper mantle. Nature, 348.

[77] Vankó, G., Neisius, T., Molnár, G., Renz, F., Kárpáti, S., Shukla, A. and de Groot, F. M. F. (2006). Probing the 3d Spin Momentum with X-ray Emission Spectroscopy: The case of Molecular-Spin Transitions. The Journal of Physical Chemistry B, 110, 24.

List of Figures

List of Tables

6. Acknowledgements

First of all, thanks to Prof. Dr. Marco Moretti without whom this incredible experience would have been simply a far mirage.

A very special thank to Dr. Valerio Cerantola, this project belongs more to him than to me, I humbly tried to bring a small contribute for the success of this research. Thanks to followed me through all my work giving me precious advice and supervising the realisation of this thesis.

Further, I also want to thank Dr. Aleksandr I. Chumakov and Dr. Dimitrios Bessas, my scientific advisors at ESRF, for their support, experience and assistance during my permanence at the synchrotron.

Thanks to all ID18 staff: thanks to Georgios Aprilis for his support during my beamtime, thanks to Ilya Kupenko and Serguy Yaroslavtsev who helped me with gentleness in the beam line and gave me advice for my thesis, thanks to Jean-Philippe Celse and thanks to Susanne Muller and Xiang Yang for their kindness and company during the coffee breaks.

Thanks to BGI to allow me to do Raman Spectroscopy there.

A great thank to my roommate and colleague Simona, to share my life with you for six months was an instructive and funny experience. Thanks to complete with me the mission of finding the best pain au chocolat in Grenoble and to support me in these six months far from home.

Thanks to the city of Grenoble and to all the special people I have met there.

Thanks to my parents who always supported me through all my life in all my decisions never letting me alone; thanks to my sister and to my brother who supported me discreetly but steadily.

Thanks to all my best friends: Elena, Claudia, Benedetta, Sara, Maria Chiara, Michela, Asia, Giorgia, Dania and Giuseppe for the wonderful experiences we spend together and their useful advices; and special thanks to Ilaria for being a sister rather than a roommate in these five years spent together in Milan.

Last but not least, thanks to Carlo, the person who made this journey truly worthy enriching my life with love.

My deep gratitude to you all.